INVESTIGATION OF CYANIDE-BASED CATALYSTS AND HYBRID ASSEMBLIES FOR ARTIFICIAL PHOTOSYNTHESIS

A DISSERTATION SUBMITTED TO

THE GRADUATE SCHOOL OF ENGINEERING AND SCIENCE

OF BILKENT UNIVERSITY

IN PARTIAL FULFILLMENT OF THE REQUIREMENTS FOR

THE DEGREE OF

DOCTOR OF PHILOSOPHY

IN

CHEMISTRY

By

Sina Sadigh Akbari

September 2022

INVESTIGATION OF CYANIDE−BASED CATALYSTS AND HYBRID ASSEMBLIES FOR ARTIFICIAL PHOTOSYNTHESIS

By Sina Sadigh Akbari

September 2022

We certify that we have read this dissertation and that in our opinion, it is fully adequate, in scope and in quality, as a dissertation for the degree of Doctor of Philosophy.

Ferdi Karadaş (Advisor)

Ömer Dağ

Emren Nalbant

Burak Ülgüt

Uğur Ünal

Approved for the Graduate School of Engineering and Science:

Orhan Arıkan

Director of the Graduate School

ABSTRACT

INVESTIGATION OF CYANIDE-BASED CATALYSTS AND HYBRID ASSEMBLIES FOR ARTIFICIAL PHOTOSYNTHESIS

Sina Sadigh Akbari

Ph.D. in Chemistry

Advisor: Ferdi Karadaş

September 2022

The storage and conversion of solar energy appear to be a highly promising solution to the global energy dilemma due to the sustainability and abundance of sunlight. Among various strategies, artificial photosynthesis, in which solar energy is directly converted to chemical bonds, has gained a great deal of attraction over the past decades. Such a design requires a catalyst coupled with a semiconductor and/or a photosensitizer as light-harvesting components with proper band levels for efficient charge separation. Therefore, the development of an earth-abundant, robust, and visible-light absorbing photocatalytic assembly has been one of the bottlenecks for the advancement of scalable cells. This work aims to overcome this critical challenge by developing new cyanide-based hybrid assemblies for light-driven water splitting and CO_2 reduction.

CoFe Prussian blue analogues (CoFe-PBAs) have recently emerged as active water oxidation catalysts with excellent long-term stabilities. In the first study, a ZnCr layered double hydroxide (ZnCr-LDH) with a two-dimensional (2D) morphology and a CoFe-PBA

are combined to afford a precious metal-free photocatalytic assembly involving a visible light-absorbing semiconductor (SC) and a water oxidation catalyst (WOC). The SC−WOC hybrid materials exhibit a threefold enhancement in activity compared to bare ZnCr-LDH, which is maintained for 6 h under photocatalytic conditions. The band energy diagram was extracted from optical and electrochemical studies to clarify the origin of the improved photocatalytic performance. The assembly is observed to have an appropriate band energy alignment that facilitates charge transfer from the valence band of ZnCr-LDH to the HOMO level of CoFe-PBA for the water oxidation process.

In a follow-up study, we move one step forward by coupling exfoliated Dion−Jacobson type niobate nanosheets as a 2D semiconductor with the CoFe-PBA to construct an SC−WOC hybrid structure, which produces a p−n junction. The assembly exhibits a promoted activity (89.5 μmol g^{-1} h^{-1}) with a proper band energy alignment for the photocatalytic water oxidation process, and it is stable throughout a 12 h photocatalytic study. These studies mark a straightforward pathway to developing low-cost and precious metal-free assemblies for light-driven water oxidation.

Metal dicyanamides are another well-known cyanide-based materials, which can be employed as a catalyst for hydrogen evolution reaction (HER) and CO_2 reduction due to the partial electron delocalization and the proper coordination environment of metal ions. Herein, we promote a cobalt dicyanamide coordination polymer, Co-dca, for the first time, as a selective catalyst to reduce CO_2 to CO in the presence of a ruthenium photosensitizer (Ru PS) under visible light irradiation. A series of photocatalytic experiments under various reaction conditions were performed to reveal the role of the PS, the scavenger, and the solvent in the selectivity and the activity of the photocatalytic process. We find that Co-dca exhibits an activity of 254 μmol h^{-1} g^{-1} and a CO selectivity as high as 93%. Furthermore,

cobalt dicyanamide also displayed enhanced H_2 evolution activity (25000 μmol h^{-1} g^{-1}), which is maintained for at least 12 h in a mixed aqueous solution containing a Ru-based photosensitizer and a sacrificial electron donor. The effect of various reaction parameters on the photocatalytic activity of the system was investigated.

Overall, this thesis presents various low-cost and stable SC-WOC hybrid assemblies based on CoFe-PBA for the light-driven water oxidation process. Moreover, we suggest the use of Co-dca, for the first time, as catalysts for HER and CO_2 reduction reactions.

Keywords: Photocatalytic water splitting, artificial photosynthesis, CO_2 reduction reaction, cobalt−iron Prussian blue, cobalt dicyanamide, hybrid assembly, 2D semiconductors.

ÖZET

YAPAY FOTOSENTEZ İÇİN SİYANÜR BAZLI KATALİZÖRLER VE HİBRİT DÜZENLEMELERİN İNCELENMESİ

Sina Sadigh Akbari

Kimya, Doktora Tezi

Danışman: Ferdi Karadaş

Eylul 2022

Güneş enerjisinin depolanması ve dönüştürülmesi, güneş ışığının sürdürülebilirliği ve bolluğu nedeniyle küresel enerji için oldukça umut verici bir çözüm olarak kabul edilmektedir. Çeşitli stratejiler arasında, güneş enerjisinin doğrudan kimyasal bağlara dönüştürüldüğü yapay fotosentez, geçtiğimiz yıllarda büyük bir ilgi gördü. Böyle bir tasarım, verimli yük ayrımı için uygun bant seviyelerine sahip bir yarı iletken ve/veya ışığa duyarlı bir malzeme ile birleştirilmiş bir katalizör gerektirmektedir. Bu nedenle, yeryüzünde bol, sağlam ve görünür ışık soğuran bir fotokatalitik düzeneğin geliştirilmesi, ölçeklenebilir hücrelerin ilerlemesi için en zor adım olmuştur. Bu çalışma, fotokatalitik yöntemle hidrojen oluşturma ve CO_2 indirgemesi için yeni siyanür temelli hibrit düzenekler geliştirerek bu kritik zorluğun üstesinden gelmeyi amaçlamaktadır.

Yapılan çalışmalar, CoFe Prusya mavisi analoglarının (CoFe-PBA) mükemmel uzun vadeli kararlılıklara sahip aktif su oksidasyon katalizörleri olduğunu göstermektedir. Bu tezdeki ilk çalışma, iki boyutlu (2D) morfolojiye sahip tabakalı bir çift hidroksit (ZnCr-LDH) bileşikle bir CoFe-PBA yapısının birleştirilerek değerli metal içermeyen

fotokatalitik bir düzenek geliştirilmesi üzerinedir. SC−WOC hibrit malzemeleri, fotokatalitik koşullar altında 6 saat boyunca kararlı kalmakla birlikte, ZnCr-LDH'ye kıyasla aktivitede üç kat bir artış sergiler. Fotokatalitik performansın kaynağını anlamak için optik ve elektrokimyasal çalışmalar yardımıyla bant enerji diyagramı ortaya çıkarılmıştır. Düzeneğin, su oksidasyon işlemi için ZnCr-LDH valans bandından CoFe-PBAnin HOMO seviyesine yük transferini kolaylaştıran uygun bir bant enerji diyagramına sahip olduğu gözlemlenmiştir.

Bunu takip eden çalışmada, bir p-n junction üreten bir SC-WOC hibrit yapısı oluşturmak için 2D yarı iletken exfole edilmiş Dion-Jacobson tipi niyobat nano tabakalarını CoFe-PBA ile birleştirerek bir adım ileri gidiyoruz. Hibrit malzeme fotokatalitik yöntemle suyun yükseltgenmesi işlemi için uygun bir bant enerji seviyesi yardımıyla yüksek bir aktivite (89,5 μmol g^{-1} h^{-1}) sergilemektedir ve 12 saatlik bir fotokatalitik çalışma boyunca kararlıdır. Bu çalışmalar, ışıkla su oksidasyonu için düşük maliyetli ve değerli metal içermeyen düzenekler geliştirmeye yönelik basit bir yolu işaret ediyor.

Metal disyanamitler, kısmi elektron delokalizasyonu ve metal iyonlarının uygun koordinasyon ortamı nedeniyle hidrojen oluşumu reaksiyonu (HER) ve CO_2 indirgemesi için bir katalizör olarak kullanılabilecek diğer iyi bilinen siyanür temelli malzemelerdir. Burada, görünür ışığa duyarlı bir rutenyum bileşiği (Ru PS) varlığında CO_2'yi CO'ya indirgemek için seçici bir katalizör olarak ilk kez bir kobalt disyanamit koordinasyon polimeri olan Co-dca'yı kullandık. Co-dca'nın 254 μmol h^{-1} g^{-1} aktivite ve %93 kadar yüksek bir CO seçiciliği sergilediğini bulduk. Ayrıca, kobalt disyanamit, sulu bir çözeltide en az 12 saat sürdürülen H_2 oluşturma aktivitesi (25000 μmol h^{-1} g^{-1}) sergilemektedir. Fotokatalitik prosesin seçiciliği ve etkinliğinde PS'nin, elektron donörü ve çözücünün rolünü ortaya çıkarmak için çeşitli reaksiyon koşulları altında bir dizi fotokatalitik deney

yapıldı. Sistemin fotokatalitik aktivitesi üzerine çeşitli reaksiyon parametrelerinin etkisi araştırıldı.

Genel olarak, bu tez, fotokatalitik yöntemle suyun yükseltgenmesi işlemi için CoFe-PBA içeren çeşitli düşük maliyetli ve kararlı SC-WOC hibrit düzeneklerinin geliştirilmesine odaklanmıştır. Ayrıca, HER ve CO_2 indirgeme reaksiyonları için katalizörler olarak ilk kez Co-dca'nın kullanılması önerilmiştir.

Anahtar Kelimeler: Fotokatalitik su ayırma, yapay fotosentez, CO_2 indirgeme reaksiyonu, kobalt-demir Prusya mavisi, kobalt disyanamit, hibrit düzenek, 2D yarı iletkenler.

ACKNOWLEDGMENT

I am extremely grateful to my supervisor, Assoc. Prof. Ferdi Karadaş for giving me the opportunity to conduct a thesis in his research group and providing precious guidance throughout my Ph.D. research. I am really thankful for the discussions and extra support that he gave me over these years. I will always be grateful to him for everything he taught me.

I would also like to offer my special thanks to our collaborator, Uğur Ünal, for his support and the valuable collaboration we had.

I would like to sincerely thank my jury members Ömer Dağ, Emren Nalbant, Burak Ülgüt, and Uğur Ünal for giving their valuable time, professional opinions, and feedback in my research to finalize my thesis.

I am very thankful to all Chemistry department faculty members for providing a friendly environment, as well as the UNAM research center for offering various sources and equipment, which I made use of them to full fill my Ph.D. research.

I would like to extend my gratitude to all past and present lab mates (who are too many to name but all friendly) in the Karadaş research group and the technical staff in the department.

My sincere gratitude goes to the scholarship provided by Bilkent University \ Department of Chemistry and funding from TÜBİTAK.

Words can never be enough to express my thank to my family. I owe special thanks to my parents, Maryam and Ghassem, for believing in me for everything, giving all their love and help in every little step of this process and before that. I want to express my special

gratitude to my mother-in-law for always supporting us and our decisions. I am so lucky to have them.

Lastly but most importantly, I would like to express my deepest thank to my wife, Elnaz, for all her understanding and motivation. Without her support, I would have been lost during the difficult times. She is truly a source of inspiration. Thank you for everything.

CONTENTS

LIST OF FIGURES

LIST OF TABLES

LIST OF ABBREVIATIONS

PV−EC: Photovoltaic electrolysis

PEC: Photoelectrochemical

OER: Oxygen evolution reaction

HER: Hydrogen evolution reaction

VB: Valence band

CB: Conduction band

DSP: Dye-sensitized photocatalysis

PS: Photosensitizer

2D: Two-dimensional

SC: Semiconductor

WOC: Water oxidation catalyst

CO_2RR: CO_2 reduction reaction

D: Sacrificial electron donor

PBA: Prussian blue analogue

HOMO: Highest occupied molecular orbital

PCET: Proton-coupled electron transfer

LDH: Layered double hydroxide

MLCT: Metal-to-ligand charge transfer

dca: Dicyanamide

XRD: X-ray diffraction

ATR−FTIR: Attenuated total reflectance−Fourier transformed infrared

XPS: X-ray photoelectron spectroscopy

SEM: Scanning electron microscopy

EDS: Energy−dispersive X-ray spectroscopy

TEM: Transmission electron microscopy

HAADF: High angle annular dark field

UV−Vis: Ultraviolet−visible

PL: Photoluminescence

NHE: Normal hydrogen electrode

FTO: Fluorine-doped tin oxide

CV: Cyclic voltammetry

CA: Chronoamperometry

TOF: Turnover frequency

DRS: Diffuse reflectance spectroscopy

MeCN: Acetonitrile

TEOA: Triethanolamine

TEA: Triethylamine

Chapter 1

Introduction

Among various sustainable energy resources, sunlight is the most abundant and promising one for global energy demands. The earth's surface gets an enormous amount of solar energy (1.3×10^5 TW per day), which exceeds the whole human energy consumption in a year. Sunlight can be harvested by directly converting solar energy to chemicals, such as H_2 or carbon-based fuels, by water splitting or CO_2 reduction reactions. Such energy stored in long-term storable chemical bonds is considered to be an attractive strategy for solving clean energy issues [1]–[4]. As shown in Figure 1, water splitting or CO_2 reduction reactions can be classified into three major categories: i) photovoltaic electrolysis (PV−EC), ii) photoelectrochemical (PEC) process, and iii) particulate photocatalysis (PC). The highest energy conversion efficiency value could be provided by a PV system (20−30%). However, large-scale device fabrication still remains the biggest challenge for designing both PV and PEC devices [5], [6]. In a typical photoelectrochemical system, a semiconductor acts as a photoanode/photocathode, and photoexcited holes/electrons are transferred on the surface of the electrode to be employed in the oxidation/reduction process. The photocatalytic strategy can be utilized as either a homogeneous or a heterogeneous system. Generally, oxidation or reduction reactions occur on the surface of the semiconductor particles or at the active center of the catalyst in the aqueous solution.

This architecture allows the design of a low-cost and scalable device for solar fuel production. However, one of the main drawbacks of photocatalytic processes is the separation of photogenerated H_2 and O_2 [6], [7].

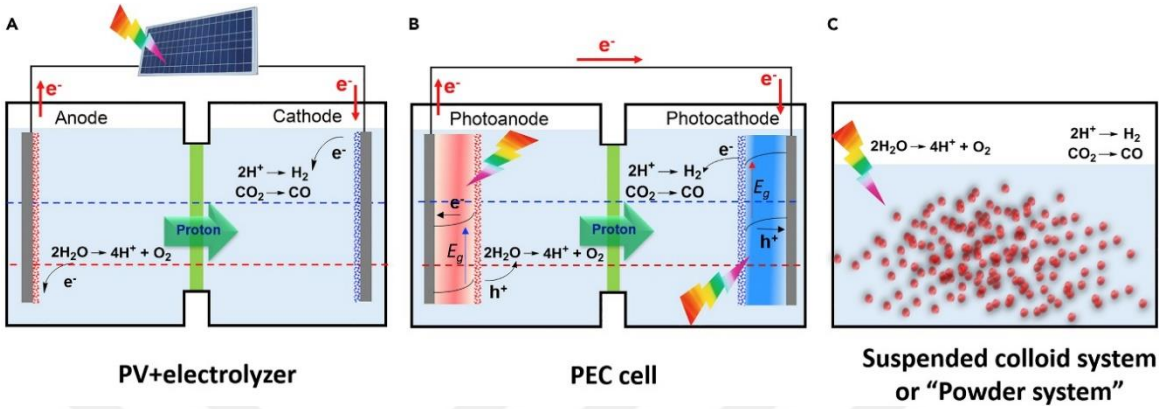

Figure 1. Schematic diagrams of various water splitting strategies. (A) PV+electrolyzer system, (B) PEC system, and (C) particulate photocatalysis (Reprinted with permission from Elsevier, Ref. [8] Copyright © 2018, Elsevier Inc.).

1.1 Aim of this Thesis

The storage of solar light as chemical bonds is one of the most plausible strategies for satisfying the world's energy demand. For this aim, we focus on studying the novel design and optimization of photocatalytic systems for water splitting and CO_2 reduction. In this work, we follow two approaches:

First, we study the performance of Co-Fe Prussian blue as a water oxidation catalyst when it is coupled to two-dimensional semiconductor materials, including Zn-Cr layered double hydroxide and niobate nanosheets.

Then, we explore the photocatalytic activity of cobalt dicyanamide coordination polymer for hydrogen evolution and CO_2 reduction reactions in the presence of a ruthenium-based photosensitizer.

Herein, four projects are presented to investigate the possible application of cyanide-based assemblies for water splitting and CO_2 reduction. Before going through the details of the characterization techniques and the obtained results, this chapter provides a brief introduction to the types of systems used in this work.

1.2 Water Splitting

In nature, plants convert solar energy into chemical energy by reducing CO_2 and oxidizing water to generate carbohydrates and oxygen, which is named natural photosynthesis. The absorption of light by photosystem II (PSII) produces electron−hole pairs (a charge separation process), and the oxidative holes are used to oxidize water molecules to oxygen gas [9]. Then, electrons are transported via photosystem I (PSI) and ultimately serve to generate bio-reducing agents such as NADPH and ATP that are energetically enriched. These agents finally reduce atmospheric CO_2 to carbohydrates in the Calvin cycle (Figure 2) [10]–[12]. The storage of solar energy into chemical bonds can mimic natural photosynthesis to construct an artificial photosynthetic system.

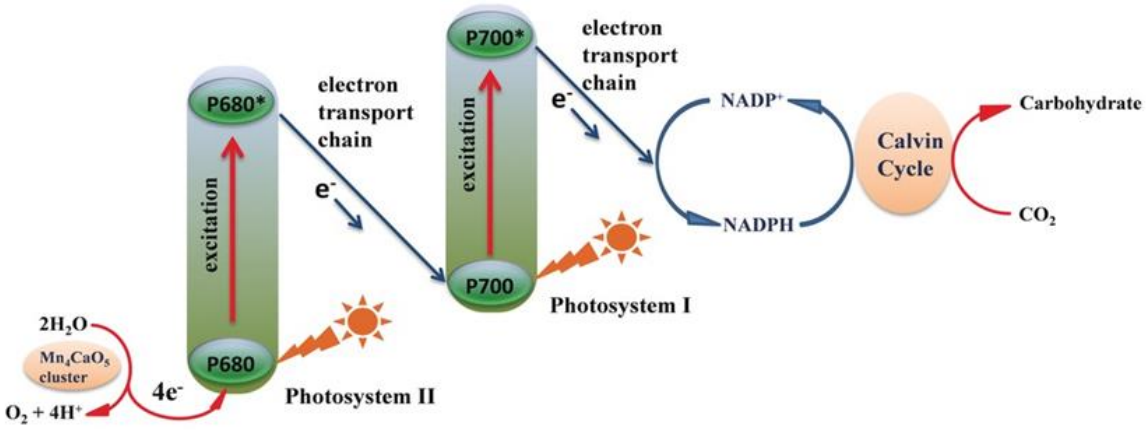

Figure 2. Schematic representation of natural photosynthesis (Reprinted with permission from John Wiley and Sons, Ref. [12] Copyright © 2016, WILEY-VCH Verlag GmbH & Co. KGaA, Weinheim).

1.2.1 Particulate Photocatalysis

The overall water splitting consists of two half-reactions: i) oxygen evolution reaction (OER) and ii) hydrogen evolution reaction (HER). These reactions are summarized below:

$$2H_2O \longrightarrow O_2 + 4e^- + 4H^+ \quad (1)$$

$$2H^+ + 2e^- \longrightarrow H_2 \quad (2)$$

The water splitting reaction is an uphill reaction that involves an increase in Gibbs free energy by 237 kJ mol^{-1}. Thus, this reaction cannot occur spontaneously, and the addition of external energy is required. A schematic of a typical semiconductor particle loaded with co-catalysts for the evolution of hydrogen and oxygen is shown in Figure 3a. For overall water splitting, a semiconductor absorbs photons with energy values greater than its band gap to excite electrons from the valence band (VB) to the conduction band (CB). This creates electron-hole pairs as the initial step of the photocatalytic process (step 1). Photo-generated electrons and holes migrate to the surface of the semiconductor (step 2). Then the holes provide oxidation of water to O_2 while the electrons reduce protons to H_2 (step 3) [13], [14].

For the successful operation of this process, the CB minimum of the semiconductor has to be located at a more negative potential than the H^+ to H_2 reduction potential (0 V vs. NHE at pH 0). In comparison, the VB maximum must be more positive than the water oxidation potential (+1.23 V vs. NHE at pH 0). This is the principle of the one-step excitation photocatalytic system (Figure 3b). The minimum thermodynamic energy needed for water oxidation is 1.23 eV, which corresponds to a wavelength of 1000 nm [13], [15]–[17].

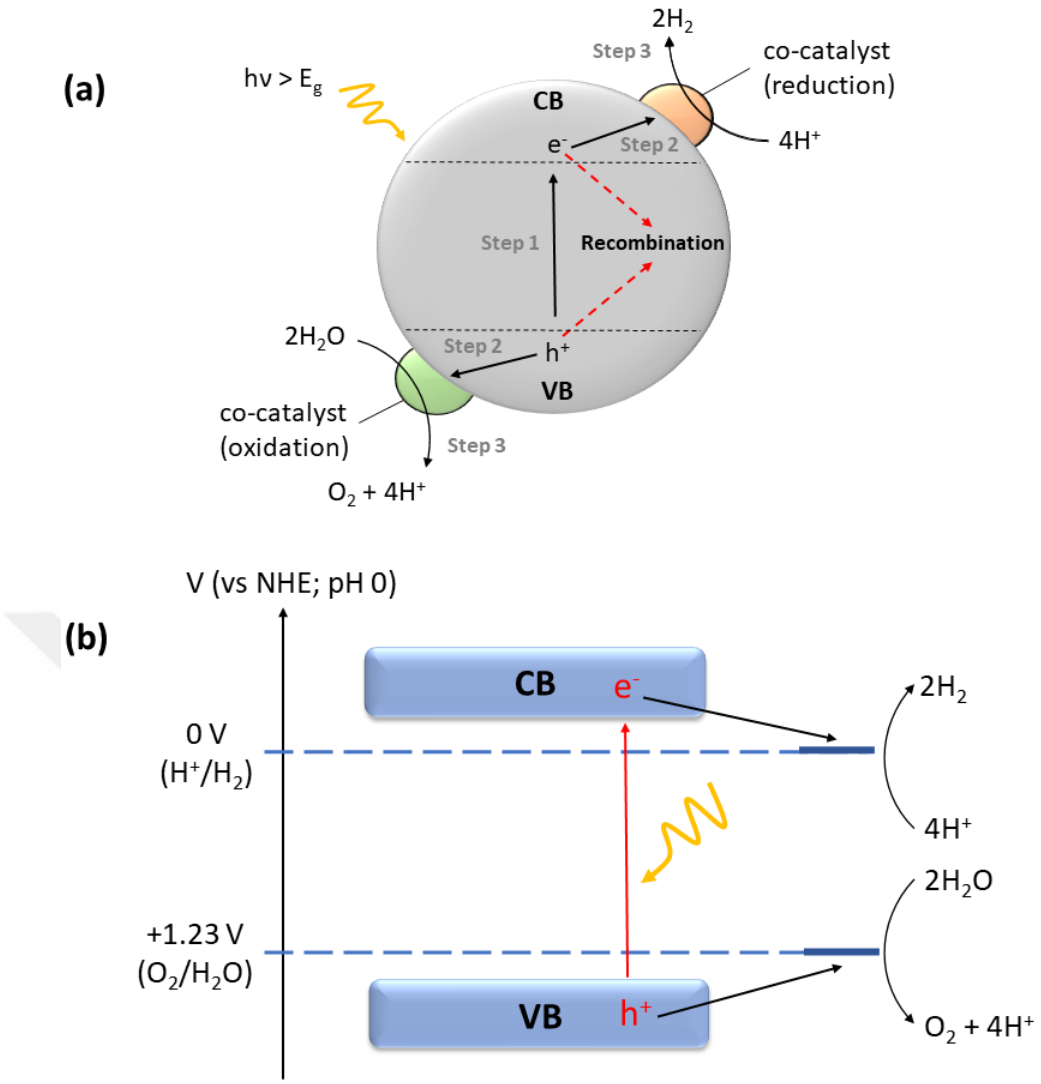

Figure 3. (a) illustration of reactions during overall water splitting (E_g: bandgap of semiconductor). (b) Energy diagram for photocatalytic water splitting.

The momentum (wave vector) of an electron in the VB maximum is identical to that of an electron in the CB minimum in the case of a direct bandgap. As a result, by absorbing photons with energies higher than the band gap energy, electrons are easily promoted from the VB to the CB, with minimal change in their momenta (Figure 4a). For a semiconductor with an indirect band gap, the states at the maximum of the VB and minimum of the CB band do not have equal momenta. Thus, a significant change in the momentum of an electron is required for excitation and to form an electron-hole pair in this case (Figure 4b).

The probability and rate of electron excitation are much lower in an indirect band gap semiconductor compared to a direct one [18], [19].

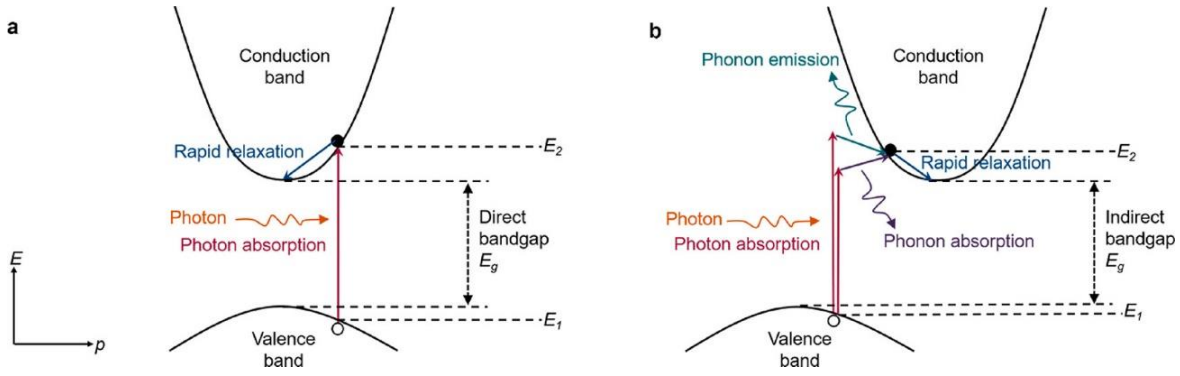

Figure 4. Photon absorption in (a) a direct bandgap semiconductor for an incident photon with energy $h\nu = E_2 - E_1 > E_g$, and (b) an indirect bandgap semiconductor for a photon with energy $h\nu < E_2 - E_1$ and a photon with energy $h\nu > E_2 - E_1$ (Reprinted with permission from American Chemical Society, Ref. [19] Copyright © 2020, American Chemical Society).

Colloidal semiconductor materials could be employed as: (i) a light-harvesting agent (Figure 5a) or (ii) a semiconductor in dye-sensitized photocatalysis (Figure 5b). In case (i), the colloid was used to both absorb light and transfer electrons/holes into a surface-anchored molecular catalyst. In case (ii), however, the semiconductor participates in the photoinduced process indirectly by facilitating the diffusion of charge from an additional photosensitizer to the catalyst. In both cases, efficient sunlight absorption and the generation of long-lived charges are necessary for a successful photocatalytic process [15], [20].

In photocatalytic water splitting, co-catalysts have three different roles in improving the activity and stability of the semiconductor: i) Co-catalyst provides redox reaction sites that reduce the activation energy or overpotential of HER or OER reactions on the surface of the semiconductor. The OER reaction is a complicated four−electron process, in which the utilization of co-catalysts might enhance the efficiency of photocatalytic O_2 production.

ii) A co-catalyst can facilitate electron−hole separation by consuming photoinduced charge carriers. The formation of a suitable hetero−junction between the co-catalyst and the semiconductor is essential for promoting charge migration and separation. iii) A co-catalyst could protect the semiconductor surface from being oxidized by holes and improve its durability. The co-catalyst loading amount has a remarkable impact on the performance of the photocatalytic water splitting system. While the introduction of the catalyst onto the semiconductor enhances the activity until reaching an optimum point, further loading will drastically decrease the photocatalytic performance. Excessive co-catalyst loading not only covers the active surface sites of the semiconductor and prevents their interaction with sacrificial reagents or water molecules but also shields the incident light, thus lowering the light absorption and generation of photogenerated electrons and holes [14], [21], [22].

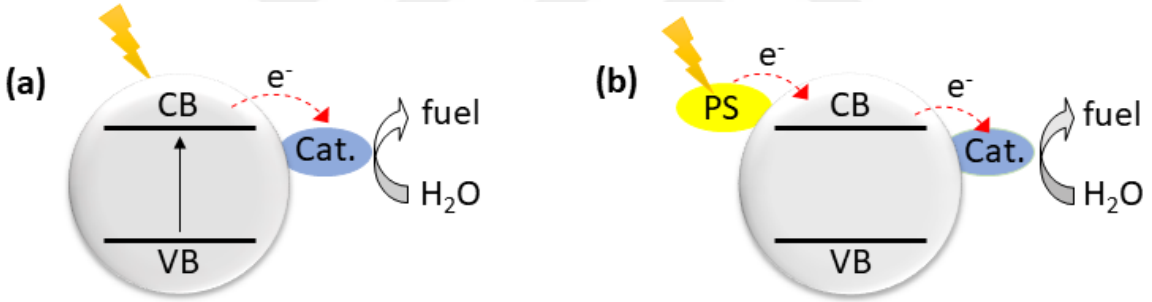

Figure 5. Schematic representation of the colloidal material used either as (a) a light absorber or (b) a semiconductor.

1.2.2 Dye-sensitized Photocatalysis

In dye-sensitized photocatalysis (DSP), a molecular dye and a catalyst adsorb onto a semiconducting particle, which is used as both a scaffold and as a solid-state electron mediator (Figure 6). In a typical DSP, solar light irradiation generates an electron-hole pair in the photosensitizer (PS), and then electrons are collected at the semiconductor. DSP systems are easy to construct by mixing in an aqueous solution, whereby each component and overall activity can be improved. The key parameter of this type of system is visible

light absorption by the PS and the efficient electron transfer into the CB of the semiconductor. Thermodynamics of water splitting is challenging in DSP: for proton reduction, for example, the semiconductor's CB must be more reducing than the proton reduction potential. In-situ assembly is possible for DSP systems if both the molecular dye and catalyst are water-soluble and bind to the semiconductor. Water-insoluble components can be dispersed in an organic solvent (ex-situ) followed by mixing with the semiconductor [23]–[25].

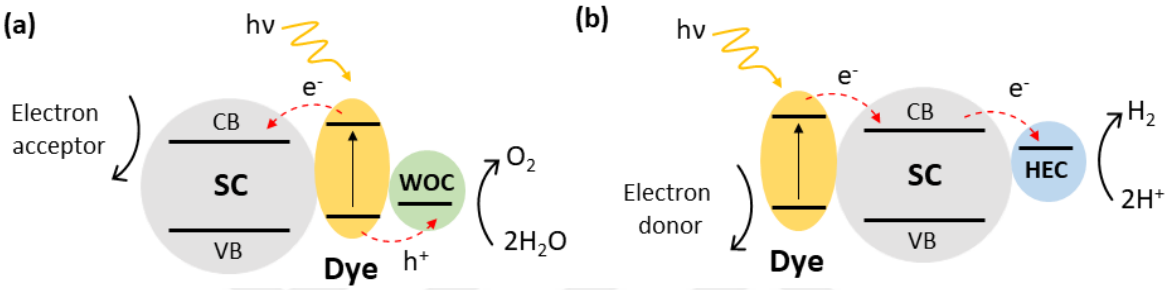

Figure 6. DSP systems for (a) water oxidation, and (b) hydrogen evolution reactions (SC: semiconductor; WOC: water oxidation catalyst; HEC: hydrogen evolution catalyst).

1.2.3 Photosensitizer-Catalyst Dyad Assemblies

When a PS dye is covalently attached to a catalyst, the resultant complex is known as a dyad that can be adsorbed on the semiconductor surface in a manner similar to the DSP. Both catalyst stabilization and efficient charge separation are aimed with this approach. The proper connection between the PS and the catalyst is critical to achieving a high-performance design [20], [26].

The initial step of photocatalysis is the generation of an excited state by absorption of solar irradiation, which occurs within the light-harvesting chromophore. Up to now, none of the studied chromophores satisfies all the conditions for an ideal light-harvesting component, including broad absorption spectrum, long excited-state lifetime, appropriate redox potentials, high photochemical stability, and flexible synthesis method. Thus, the

selection of chromophores is crucial in developing dyad assemblies to enable effective energy transfer and panchromatic absorption. The charge recombination in the PS is another problem that needs to be minimized. Thus, long-lived charge-separated states are desired to ensure that each photon is converted into chemical energy by the photocatalytic system. [27].

Several light-driven water splitting systems have successfully employed the ruthenium trisbipyridil complex, $[Ru(bpy)_3]^{2+}$, and its derivatives as the light-absorbing unit (Figure 7). This family of photoactive complexes exhibits unique redox and photochemical properties [28]–[30].

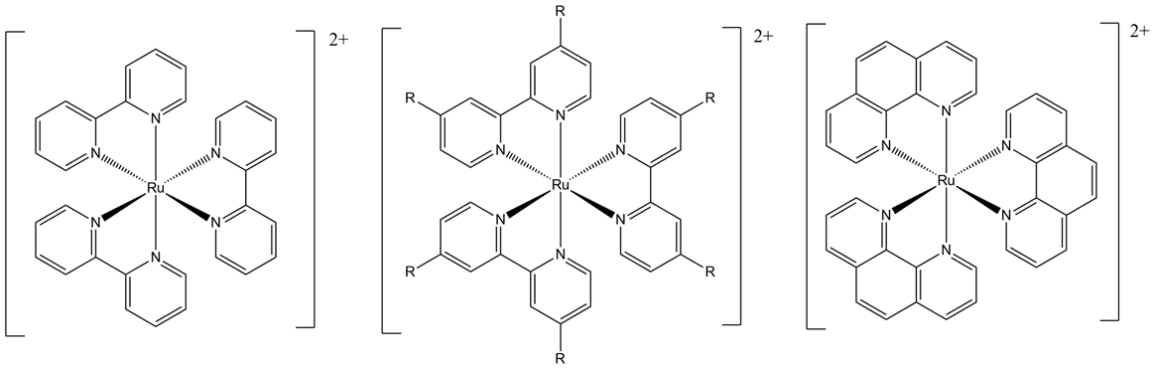

Figure 7. Structure of the ruthenium-based PSs.

The photosensitized process can proceed via two mechanisms: oxidative or reductive quenching. The use of stable oxide materials to design heterogeneous assemblies might be a possible way to improve stability; however, the lack of complete control over metal ion coordination in oxide chemistry restricts the construction of oxide-based dyads [20], [31].

1.2.4 p−n Heterojunction Photocatalytic System

Recently, combining a p−type and n−type semiconductor to fabricate a heterojunction structure has attracted vigorous attention (Figure 8). Such a design creates an internal electric field due to the flow of charge carriers. In this structure, electrons can move to the

CB of the n−type semiconductor, and holes can diffuse to the VB of the p−type semiconductor. Hence, it can improve charge separation efficiency and promotes charge carriers' lifetime, which results in an enhanced photocatalytic activity [32], [33].

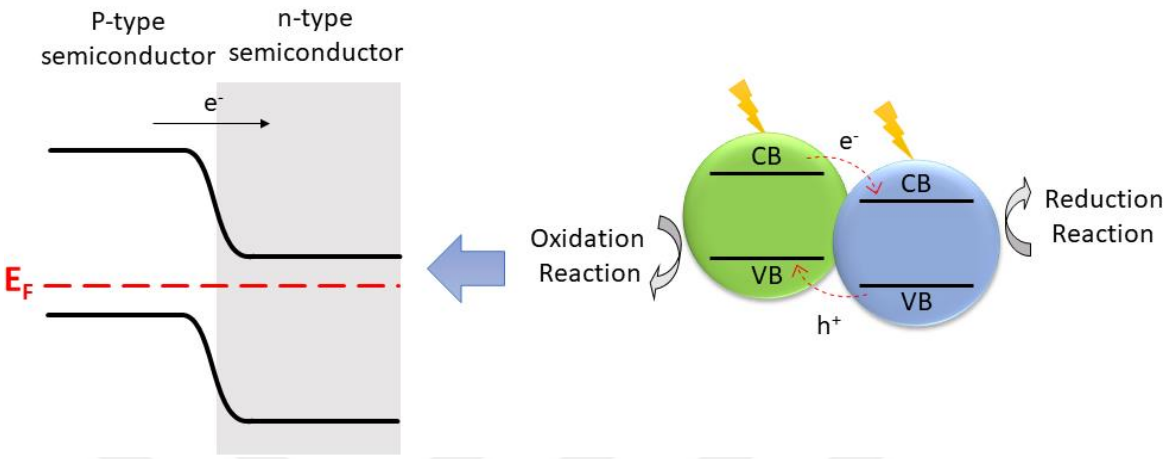

Figure 8. Band-bending and band alignment in p−n heterojunction semiconductors.

1.3 Two-dimensional (2D) Materials for Photocatalytic Water Splitting

Despite the rapid development of semiconductor photocatalysts for the water splitting process, they suffer several challenges. Most of the active sites in bulk semiconductors are not accessible and, thus, they cannot be efficiently used for the catalytic reaction. Furthermore, the recombination reaction between electron and hole is one of the crucial factors that reduce photocatalytic activity. The electron−hole pairs are generated when a semiconductor is irradiated by light with an energy greater than the band gap. These charge carriers must reach the surface of the semiconductor to carry out OER and HER reactions. During this transfer process, they might be recombined or get trapped by the defect sites. Although a semiconducting nanocrystal might be an ideal material for suppressing recombination and providing a short travel distance, obtaining sufficient photon flux density may be challenging to accomplish photocatalytic water splitting [34]–[36].

Two-dimensional (2D) materials can be used to minimize the recombination reaction and shorten the travel distance for charge carriers. Moreover, the 2D architecture facilitates

light absorption even at low photon flux density. A 2D crystal material, the so-called 2D nanosheet, prepared by exfoliation of a layered compound reveals a significantly low recombination rate due to an ultrathin thickness and a lateral dimension of several hundreds of nanometers (Figure 9). These materials demonstrate the remarkable capacity of electron confinement in their ultrathin layers, resulting in outstanding optical and electrical properties. By adjusting the number of layers, the band gap and light absorption of a 2D semiconductor can be modified. The layered structure also has a high specific surface area, allowing surface reactions such as water splitting to occur efficiently [35], [37], [38].

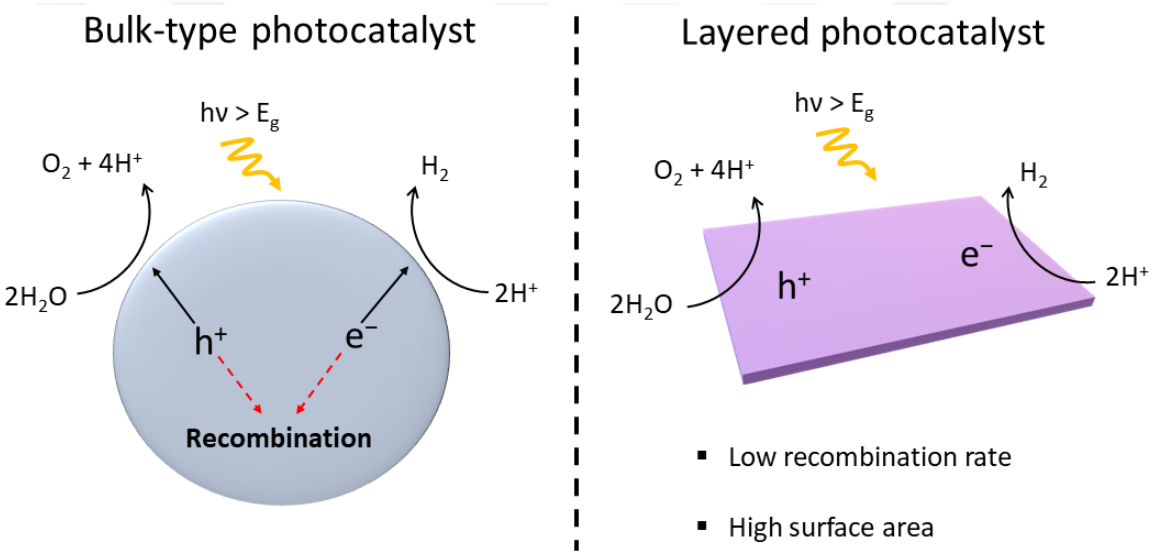

Figure 9. Comparison of bulk-type particles and 2D materials as photocatalysts.

Exfoliation of layered metal oxides forms unilamellar single-crystalline colloidal nanosheets with a thickness of 1−2 nm. In recent years, metal oxide nanosheets such as niobate have gained significant attention as a photocatalyst for the water splitting process [39], [40]. Layered double hydroxides with 2D lamellar structure consist of positively charged brucite-like layers and interlayer anions. Layered double hydroxides have a moderate surface area and activity for water splitting due to the layered structure. Several

studies on photocatalytic water splitting with layered double hydroxide-based materials have recently been published, which is a rapidly growing field in water splitting [38].

1.4 Oxygen Evolution Reaction (OER)

One of the challenging steps for the construction of an overall water splitting system operating with sunlight is the water oxidation process. The lowest energy path for water oxidation reaction is a four-electron transfer process that is coupled to form O_2 from the water molecule (Equation 1), reflecting its mechanistic complexity [41], [42]. Photocatalytic water oxidation using powder suspensions has been an appealing technique since it offers a simple, relatively low-cost, and readily scalable method to harvest solar light. These photocatalytic assemblies generally involve coupling a proper semiconductor (SC) with a water oxidation catalyst (WOC). Despite the fact that hundreds of different assemblies have been reported up to date, most of them are active primarily in the UV region (< 400 nm), and/or WOCs are mainly based on precious metal oxides [6], [11], [20], [43]. Therefore, developing an earth-abundant and visible-light harvesting SC-WOC hybrid structure is one of the critical challenges for advancing scalable and efficient photocatalytic water splitting systems.

1.5 CO_2 Reduction Reaction (CO_2RR)

The as-emitted carbon dioxide (CO_2) has been continually accumulating in the atmosphere in the last few decades due to the massive use of fossil fuels. At the same time, considerable efforts have been made to develop alternative energy technologies. The production of fuels from CO_2 is a promising yet challenging approach for clean energy conversion and storage [44], [45].

CO_2 is the ultimate chemical product of carbon oxidation and is a thermodynamically stable compound. Each of the C=O bonds in CO_2 has a bond dissociation energy (750 kJ mol^{-1}) significantly larger than that of the C−C (336 kJ mol^{-1}) and C−H (441 kJ mol^{-1}) bond. Furthermore, the CO_2RR is a thermodynamically uphill reaction and requires remarkable energy input. Several different reaction pathways may occur during CO_2 reduction generating various chemicals such as carbon monoxide (CO), formic acid (HCOOH), methane (CH_4), and ethylene (C_2H_4), which can make CO_2 reduction even more complicated. The critical challenges in CO_2RR, thus, involve sluggish kinetics and low selectivity [46], [47].

1.5.1 Photocatalytic CO_2 Reduction

The direct conversion of CO_2 into energy-rich carbon-containing compounds through a photochemical process has gained great interest since intermediate energy carriers are not necessary. The one-electron reduction of CO_2 is a thermodynamically unfavorable reaction because the formation of unstable $CO_2^{\bullet-}$ radical (Equation 3) does not start at the potential as negative as −1.9 V vs. NHE. However, the multi-electron reduction of CO_2 via chemical reaction could be promising from the perspective of both low-energy light application and stable reduction product. For instance, there is a 1.3 V difference in the potential for converting CO_2 to CO and formic acid compared to the one-electron reduction of CO_2 (Equations 4 and 5) [48]–[50].

$$CO_2 + e^- \rightarrow CO_2^{\bullet-} \qquad -1.9 \text{ V vs. NHE} \qquad (3)$$

$$CO_2 + 2e^- + 2H^+ \rightarrow CO + H_2O \qquad -0.52 \text{ V vs. NHE} \qquad (4)$$

$$CO_2 + 2e^- + 2H^+ \rightarrow HCOOH \qquad -0.61 \text{ V vs. NHE} \qquad (5)$$

Note that both CO and HCOOH are beneficial chemicals and can be converted to fuels via other processes. For instance, the Fischer–Tropsch reaction can be employed to convert CO into a liquid hydrocarbon using H_2 gas. Most of the reported photocatalytic CO_2 reduction systems based on transition metal complexes contain a redox PS, a reductant (D) so-called a sacrificial electron donor, and a catalyst. During the photocatalytic process, the PS photochemically induces a one-electron transfer from the reductant to the catalyst. Subsequently, the catalyst accumulates two electrons and reduces the CO_2 molecule, producing CO and/or HCOOH (Figure 10) [49].

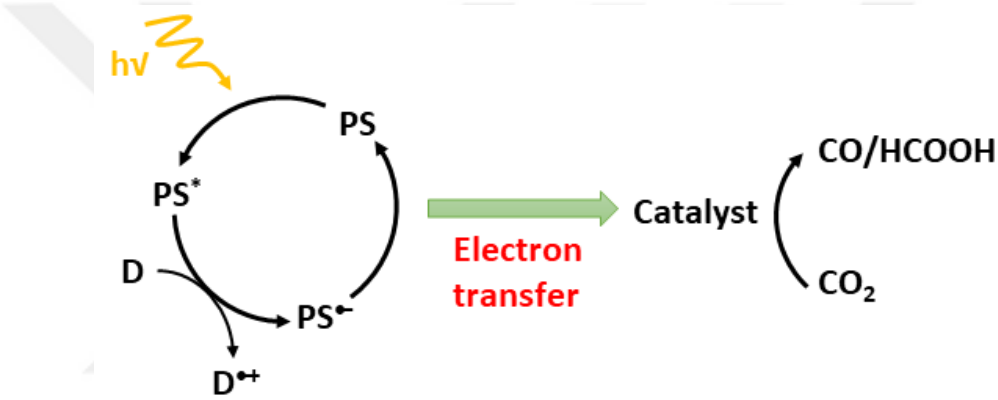

Figure 10. Schematic representation for photocatalytic CO_2RR.

Electron transfer from D to the catalyst through photoexcitation in the photocatalytic CO_2 reduction processes should be mediated by a redox PS. There are two types of reaction mechanisms in the initial stage: i) Oxidative quenching and ii) reductive quenching. In the oxidative quenching, the excited PS (PS^*) transfers an electron to the catalyst, in which a one-electron oxidized species of the photosensitizer unit ($PS^{\bullet+}$) and a one-electron reduced species of the catalyst unit ($Cat^{\bullet-}$) are formed. Subsequently, a sacrificial donor (D) donates one electron to $PS^{\bullet+}$. In reductive quenching, however, PS^* is first reduced by a sacrificial electron donor, resulting in a one-electron reduced species of the PS ($PS^{\bullet-}$). Then the unpaired electron is transferred from $PS^{\bullet-}$ to the catalyst. The latter procedure was utilized in the majority of the photocatalytic CO_2 reduction systems (Figure 11) [49], [51], [52].

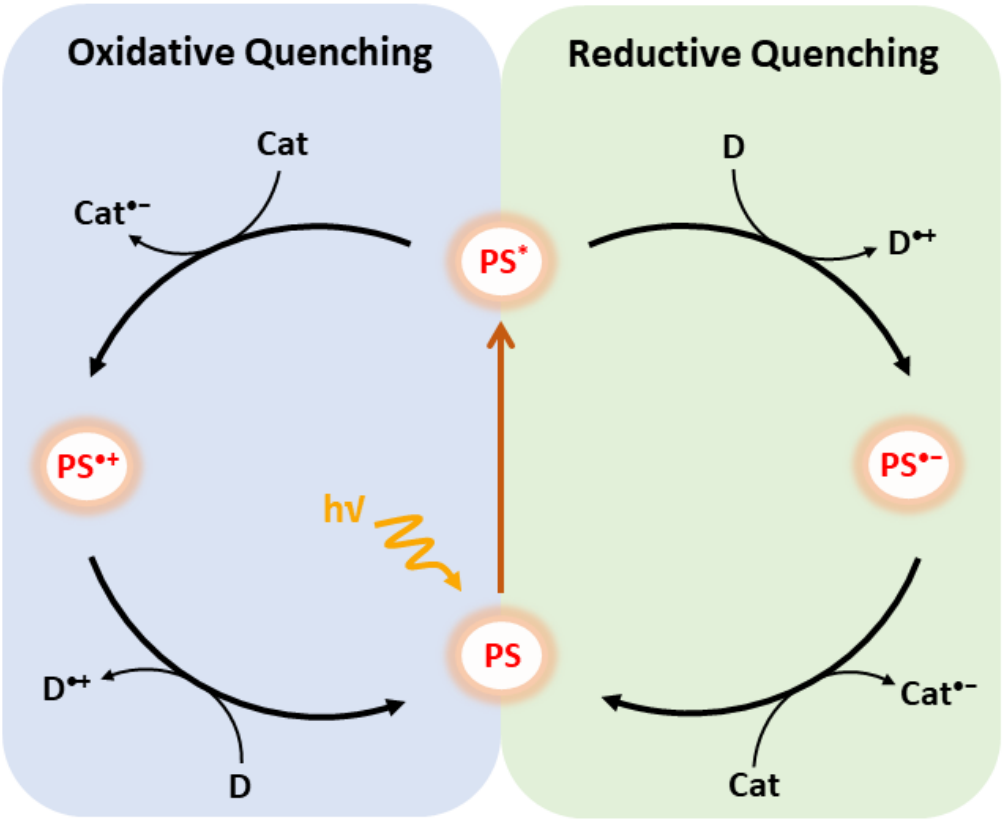

Figure 11. Oxidative and reductive quenching in a photocatalytic system (PS: photosensitizer; Cat: catalyst; D: electron donor reagent).

Phthalocyanines [53], [54], MOFs [55]–[58], oxides [59], [60], LDHs [61], [62], and most recently Prussian blue analogues have been utilized as heterogeneous catalysts for photocatalytic conversion of CO_2 to CO [63]. Notably, the studies on metal phthalocyanines reveal that capping ligands, which allow partial delocalization, play a critical role in the catalytic activity and selectivity of the CO_2 to CO conversion process [64], [65].

1.6 Hydrogen Evolution Reaction (HER)

Large-scale generation of hydrogen from renewable solar energy using a catalytic reaction is an ideal approach for sustainable energy production [31], [66]. Photocatalytic water splitting is one of the methods for H_2 production since it utilizes sunlight energy and is a low-cost and environmentally friendly method [19], [67], [68]. The water splitting

processes (HER and OER) at standard conditions have a high positive Gibbs free energy and are thus thermodynamically unfavorable. Therefore, a suitable photocatalyst is required for efficient photocatalytic H_2 evolution. First, solar light absorption is necessary for a photocatalyst, and the ideal one should include the majority or the whole visible light spectrum (ca. 400–800 nm, 43% in solar energy). Second, the CB edge of the semiconductor photocatalyst has to be located at a more negative potential than the H_2 evolution (0 V vs. NHE, pH = 0). Besides, effective charge separation, high chemical stability, and noble metal-free are some other features that must be considered [69]–[71].

After Fujishima and Honda's 1972 discovery of light-driven PEC water splitting using TiO_2 as a photocatalyst [72], several studies have been performed to develop an efficient catalyst for H_2 evolution. HER photocatalytic systems generally involve a catalyst, a PS, and a sacrificial electron donor. The PS serves as both a light absorber and an electron carrier for the catalyst. Various PSs have been developed, including organic and organometallic chromophores [73]–[77]. The catalyst in photocatalytic HER receives electrons from the excited state of the PS (oxidative quenching) or from the PS radical anion formed by a sacrificial electron donor (reductive quenching). Although metallic colloidal Pt or Pt-containing complexes exhibit excellent activity for H_2 generation, they are rare and expensive [78], [79]. Therefore, noble-metal-free complexes based on cobalt, nickel, iron, and copper have gained significant attraction over the past decade [11], [29], [80], [81]. Tertiary amines, alcohols, and ascorbic acid are examples of commonly used sacrificial electron donors that provide required electrons for HER. Decomposition of electron donor reagents typically occurs after one-electron oxidation, which produces protons. Thus, the sacrificial agent is not only the source of electrons but also protons [70].

1.7 Prussian Blue Analogues (PBAs) for Water Oxidation

Prussian blue analogues (PBAs) are the most well-known cyanide-based compounds, known as microporous coordination polymers with a 3D open framework structure. The general formula of a PBA is $A_{x/n}M_{(3-x)}[M'(CN)_6]_2 \cdot nH_2O$ (where A is an alkali metal cation, and M and M′ are transition metals), which can be easily obtained by mixing a hexacyanometalate complex with a 3d transition metal ion. Metal cations in PB structures are linked together by cyanide bridging ligands, generating a cubic coordination network. The incorporation of various 3d transition metal ions into PBAs allows for a systematic study of the water splitting process [82]–[84]. Figure 12 shows the typical crystalline structure of a cobalt-based PBA, cobalt-iron PBA (CoFe-PBA).

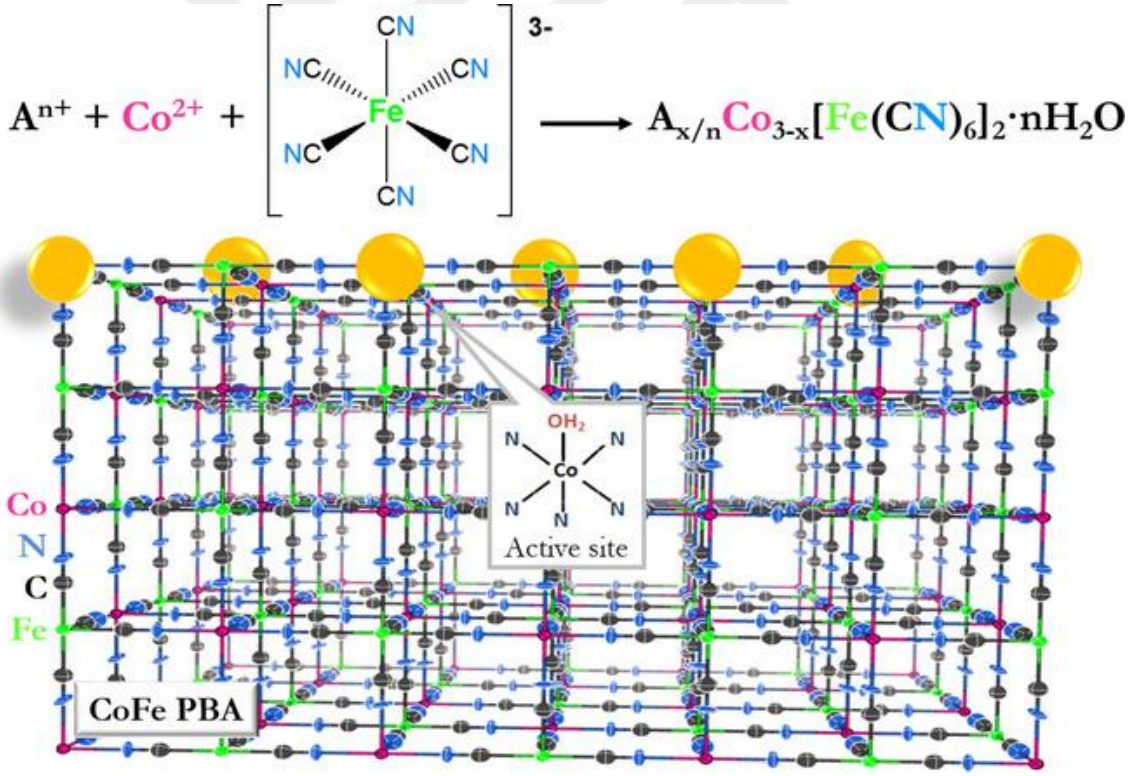

Figure 12. Synthesis method and structure of CoFe-PBA (Reprinted with permission from John Wiley and Sons, Ref. [84] Copyright © 2021, WILEY-VCH Verlag GmbH & Co. KGaA, Weinheim).

1.7.1 Cobalt−Iron PBA

A cobalt-based PBA was used as one of the first non-oxide heterogeneous WOCs in 2013 [85]. The metal ions that are connected through a cyanide group yield a rigid and robust structure, which is stable even under harsh electrocatalytic and photocatalytic conditions over a wide pH range, pH 1−13 [86]. The iron sites in a CoFe-PBA network, which are coordinated with cyanide groups, are catalytically inactive. A cobalt cation is surrounded by a combination of nitrogen atoms of cyanide groups and water molecules (Figure 13). Since the cobalt ion in the PB structure is easily oxidized to higher oxidation states, it is a suitable catalytic site for the oxidation of water [84].

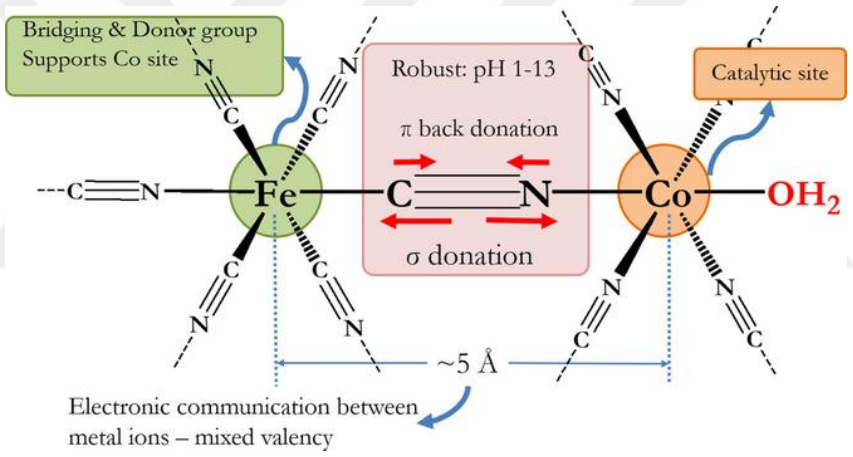

Figure 13. Characteristic features of each constituent in a CoFe-PBA (Reprinted with permission from John Wiley and Sons, Ref. [84] Copyright © 2021 WILEY-VCH Verlag GmbH & Co. KGaA, Weinheim).

Because of many critical features, cobalt-based PBAs are ideal catalytic compounds for water oxidation. PBA synthesis can be modified to provide a specific morphology for the desired application using earth-abundant, non-toxic, and low-cost precursors. Unlike the majority of typical oxide-based WOCs, PBAs are stable in acidic media. Since the cyanide bridging group forms micro-channels with a diameter of around 5 Å, PBAs are considered as one of the earliest coordination polymers, which allow small molecules, including water

and oxygen, to move through the structure. Moreover, fast electronic communication between metal ions is provided by the short cyanide linker [84].

1.7.2 Photocatalytic Water Oxidation

It is important to note that PBA materials have a poor light-absorbing property. As a consequence, the general strategy is to couple PBA with a suitable PS and/or semiconductor to utilize them for the light-driven water oxidation process. In such a design, the VB of the semiconductor (or HOMO level of the PS) is expected to be lower than the HOMO level of the PBA structure for effective charge transfer. As a result, the hole generated in the VB of the semiconductor upon excitation can be injected into the HOMO level of PBA to activate the catalytic site. An electron acceptor in the electrolyte extracts the electron from the CB for charge balance (Figure 14).

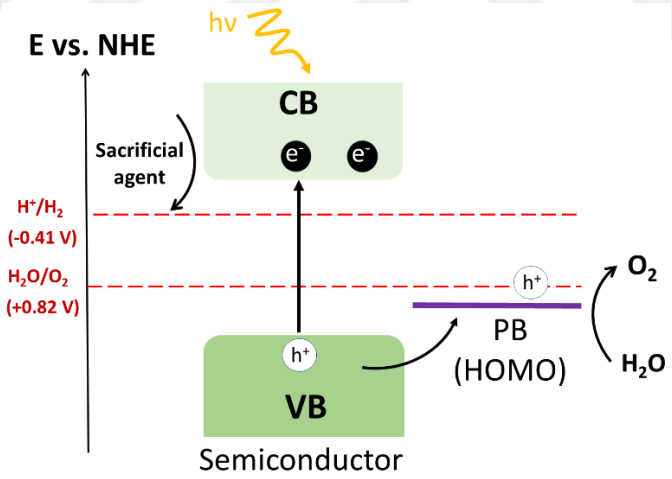

Figure 14. An estimated band structure of an SC−PB hybrid assembly for water oxidation process (pH = 7) involving the electron transfer mechanism.

The CoFe-PB structure offers an excellent catalyst for water splitting cells because its HOMO level is placed at a lower energy state than the water oxidation potential. The photocatalytic activity of CoFe-PB has been investigated in the presence of various chromophores such as $[Ru(bpy)_3]^{2+}$, Ru−poly(4−vinylpyridine), and porphyrin derivative

[85], [87], [88]. Besides, several semiconductors have been combined with CoFe-PB to construct water oxidation photoanodes [89], [90].

1.7.3 Catalytic Mechanism

Similar to the oxide-based materials, the $4e^-$ mechanism includes oxidation and activation of the catalytic site through four proton-coupled electron transfer (PCET) steps to achieve a high-valent metal-oxo species. A nucleophilic water molecule attacks this active species to produce a peroxo species, which is ultimately liberated as an oxygen molecule. The $4e^-$ water oxidation process proceeds in a single cobalt site due to a relatively long distance between two cobalt ions. Both oxidation of Co^{3+} to a higher oxidation state and the nucleophilic attack of the water molecule to a cobalt-oxo species are key steps, and one of them could be assigned as the rate-determining step in the water oxidation process (Figure 15) [84].

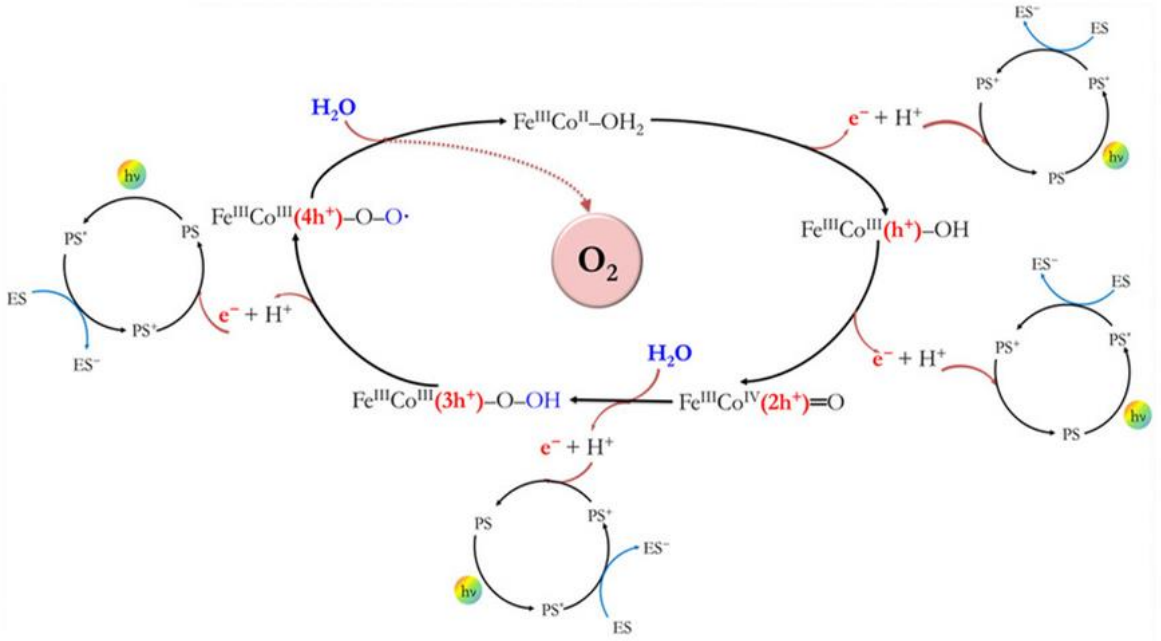

Figure 15. The responsible PCET mechanism for photocatalytic water oxidation with CoFe-PBAs (PS: photosensitizer, ES: electron scavenger; Reprinted with permission from John Wiley and Sons, Ref. [84] Copyright © 2021, WILEY-VCH Verlag GmbH & Co. KGaA, Weinheim).

1.8 2D Semiconductors for Water Oxidation

1.8.1 Layered Double Hydroxides (LDHs)

Layered double hydroxides (LDHs) or hydrotalcite-like compounds are a class of 2D materials composed of positively charged layers. The general formula of LDHs can be represented by $[M_{1-x}^{2+}M_x^{3+}(OH)_2]^{x+}[A_{x/n}]^{n-}.mH_2O$, where M^{2+} and M^{3+} are divalent and trivalent metal cations coordinated octahedrally by hydroxyl groups in the layers. Water molecules and charge-compensating anions (A^{n-}) are located in between the layers (Figure 16). In previous studies, numerous synthetic protocols such as hydrothermal/solvothermal method, co-precipitation, electrodeposition, and ion-exchange approach have been employed in the preparation of LDHs, achieving successful progress. There is a growing interest in these materials because of the compositional flexibility afforded by their considerable tunability in terms of the variety of metal cations, the M^{2+}/M^{3+} molar ratios, and the type of interlayer anions. LDHs have several applications in the field of heterogeneous catalysis due to their vast range of physical and chemical properties [91]–[94].

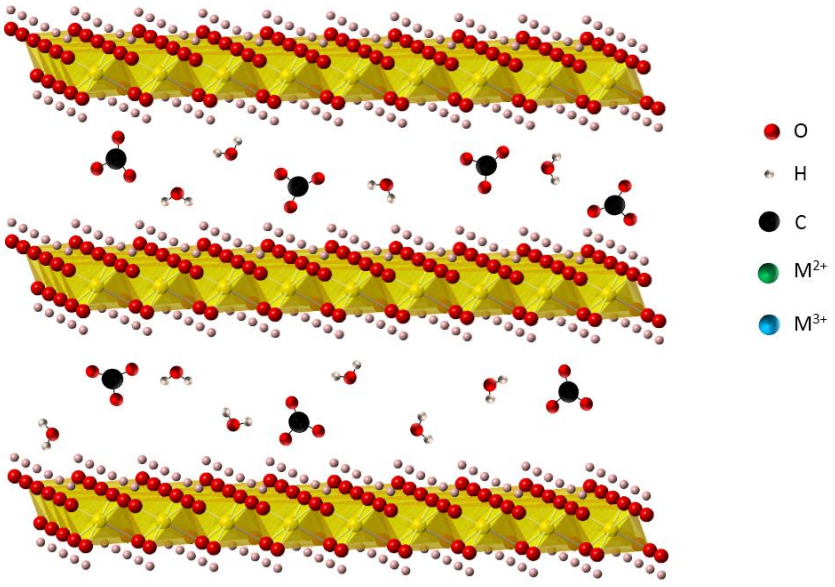

Figure 16. The idealized structure of carbonate-intercalated LDHs.

Delamination of LDHs is an interesting approach that yields positively charged thin platelets with a thickness of a few atomic layers. Compared to other layered materials, the exfoliation of LDHs is more challenging. The high charge density of the LDHs layers and the high anion amount create strong interlayer electrostatic interactions between the sheets and a prominent hydrophilic nature [95]. Nevertheless, LDHs have been widely used in photocatalytic water splitting without exfoliation due to their abundant active metal centers, efficient visible light harvesting property, and their proper band alignment with respect to HER [96], [97], [106]–[108], [98]–[105].

Among the various transition metal LDHs, Zn-Cr LDH (ZnCr-LDH) is an n-type semiconducting material with enhanced photocatalytic activity. Although LDHs have been extensively employed for photocatalytic water splitting, only a few studies have used ZnCr-LDH as a narrow bandgap semiconductor for the photocatalytic water oxidation process [109]. ZnCr-LDH has attracted the interest of several studies in the past few years, which has been employed either as an individual photocatalyst [110]–[112] or as part of a heterostructure consisting of a combination of semiconductors for overall water splitting [113]–[115]. Although ZnCr-LDH possesses a proper band energy alignment for visible-light-driven water oxidation, poor charge mobility in LDHs leads to unavoidable recombination of photo-induced charge carriers, thus, inhibits their efficiencies [109]. For this reason, various strategies to suppress photogenerated charge recombination and improve the interfacial kinetics of LDH materials are necessary to promote LDH-based water splitting technologies [116]–[119]. Although ZnCr-LDH has been coupled with other semiconductors for photocatalytic applications, it has not yet been combined with a water oxidation catalyst.

Such a design requires the coupling of two components with matching band energies for efficient charge separation. CoFe-PBA has recently been acknowledged as an efficient

and robust WOC, and could be an ideal co-catalyst to be coupled with a ZnCr-LDH since i) it is a precious-metal-free compound, ii) it can be prepared via straightforward solution chemistry, and iii) our previous studies suggest that CoFe-PBA is projected to have a proper band energy alignment that can facilitate charge transfer from the valence band of ZnCr-LDH to water oxidation reaction [87], [88], [120]–[122].

1.8.2 Niobate Nanosheets

The photocatalytic activity of a semiconductor can be enhanced by increasing the crystallinity and surface area. High crystallinity decreases the number of structural defects and vacancies that may serve as electron−hole recombination sites. Moreover, a large surface area provides more active sites, which supplies more redox reactions on the surface. However, it is difficult for typical bulk materials to achieve both high crystallinity and high surface area. Metal oxide nanosheets offer many advantages that make them ideal for photocatalytic applications compared to similar 3D materials. Nanosheets are generally single-crystalline and have an extremely high surface-area-to-volume ratio, allowing them to achieve both high crystallinity and a large surface area. In addition, the nanoscale thickness promotes the migration of photogenerated electron−hole to the surface, which enhances charge separation and suppresses recombination reaction. They can also be used as building blocks for the development of new materials with long-range controlled structure periodicity [40], [123].

2D layered perovskites have attracted attention since their electronic properties and surface areas could be easily modified by ion exchange, intercalation, and reconstruction of the layered structure after exfoliation [39], [123], [124]. One of the typical examples of layered oxides, $KCa_2Nb_3O_{10}$ (Figure 17), exhibits a Dion-Jacobson type layered perovskite structure with negatively charged metal oxide sheets ($Ca_2Nb_3O_{10}^-$) separated by potassium

ions [123]. These perovskite sheets can readily be obtained after proton exchange and exfoliation reactions. The dimensionality of the structure is reduced from a bulk one to 2D nanosheets with the exfoliation process, which provides high surface area, improved electrical properties, and enhanced photocatalytic activities [125]–[127]. Furthermore, 2D nanosheets of exfoliated layered perovskites can be used as building blocks in the design and development of novel materials for various applications. Dye molecules, oxides, quantum dots, and even metallic nanostructures have previously been incorporated into the layered niobates using the method mentioned above [128]–[135]. This approach holds the potential not only to inhibit the recombination of electron−hole pairs by stimulating charge separation but also to develop semiconductor−catalyst hybrid assemblies.

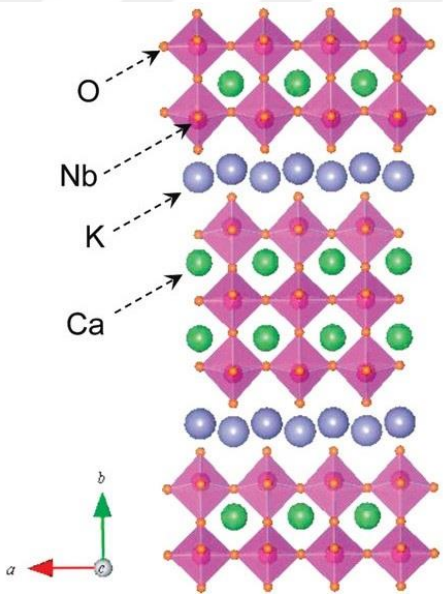

Figure 17. Structure of $KCa_2Nb_3O_{10}$ (Reprinted with permission from American Chemical Society, Ref. [136] Copyright © 2009, American Chemical Society).

Previous reports on layered niobates and CoFe-PBA reveal that they could collaborate for a photocatalytic water oxidation process due to their proper energy level alignments [84], [137]. Although bare layered niobates are suitable candidates for HER, they must be either sensitized or coupled with a catalyst for the water oxidation reaction. It has been

claimed in several studies that the exfoliation/restacking route is essential for oxygen evolution from niobate sheets [40], [137]–[139]. Restocking increases the surface area and improves the accessibility of reactant molecules, such as water, to catalytic sites on nanosheets. Platinum nanoparticles, 3d metal oxides, and ruthenium trisbipyridyl complexes have previously been intercalated into niobate oxide sheets [134], [135], [140]. On the other hand, CoFe-PBAs have previously been combined with PSs and/or semiconductors for the light-driven water oxidation process. For the development of PB-based photocatalytic hybrid assemblies, various components have been utilized, ranging from ruthenium PSs to porphyrin derivatives, oxide-based semiconductors, LDHs [87], [88], [120], [141]–[143]. Herein, we combine a layered niobate and a CoFe-PB structure to develop a semiconductor−catalyst hybrid assembly for the photocatalytic water oxidation process.

1.9 Ruthenium-based Photosensitizers

In the photocatalytic CO_2RR and HER studies, $[Ru(bpy)_3]^{2+}$ (bpy = 2,2′-bipyridine) complex and its derivatives have been the most commonly used redox PSs. These photoactive complexes exhibit unique redox and photochemical properties. $[Ru(bpy)_3]^{2+}$complexe absorbs visible light very effectively due to the characteristic metal-to-ligand charge transfer (^{1}MLCT) from the d orbitals of the Ru(II) center to the π^* orbital of ligands. The singlet excited state (S = 0; $^{**}[Ru(bpy)_3]^{2+}$) created upon excitation rapidly converts into a triplet state (S = 1; $^{*}[Ru(bpy)_3]^{2+}$), ^{3}MLCT, through intersystem crossing due to the strong spin−orbit coupling effect of ruthenium. With a τ = 0.6 μs, this excited state is long-lived enough to interact with other solute molecules before being deactivated. The energy difference between the ground state and $^{*}[Ru(bpy)_3]^{2+}$ is 2.12 eV. As an electron is present in the π^* antibonding orbital of one ligand, this excited state serves as a strong

reducing agent with a standard potential of −0.86 V vs. NHE. Additionally, $^{*}[Ru(bpy)_3]^{2+}$ can also act as a powerful oxidizing agent with E° = 0.84 V vs. NHE due to the existence of an unoccupied d orbital at the metal center (Figure 18). The reactivity of the excited state as a reducing or oxidizing species is determined by the types and amounts of redox components [29], [144]–[146].

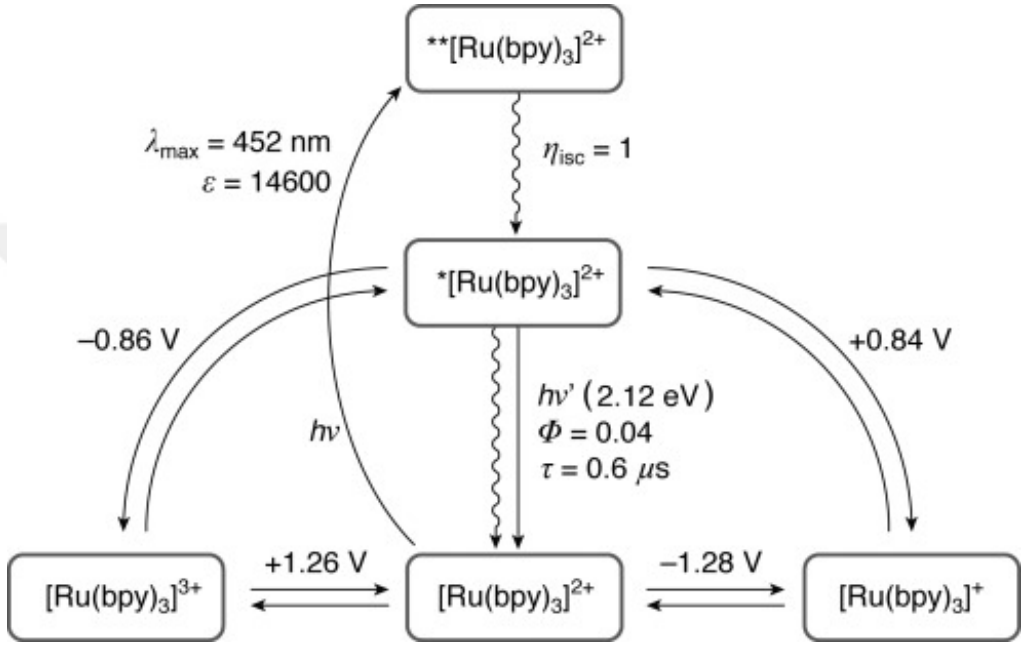

Figure 18. Molecular quantities of $[Ru(bpy)_3]^{2+}$ relevant for electron transfer processes. Reduction potentials are referred to as NHE (Reprinted with permission from John Wiley and Sons, Ref. [146] 2015, WILEY-VCH Verlag GmbH & Co. KGaA, Weinheim).

Photoexcitation of ruthenium-based PSs may lead to the decomposition and formation of $[[Ru(bpy)_2L_2]^{m+}$−type complexes (L = solvent, CO, or Cl). Since the decomposed complex might act as a catalyst, photocatalytic CO_2RR and HER occur even without the catalyst. The combination of $[Ru(bpy)_3]^{2+}$ and transition metal complexes (as the catalysts) improves electron transfer between two components for efficient catalytic reaction in the presence of the sacrificial electron donor reagent. Since the HER competes with CO_2RR, the catalyst should have a low ability to evolve H_2. Therefore, the HER must be suppressed during the photocatalytic CO_2 reduction process [49], [51].

1.10 Sacrificial Electron Donor

The selection of sacrificial electron donor (D) can significantly impact the photocatalytic system's activity. Since the back electron transfer from $PS^{\bullet-}$ to $D^{\bullet+}$ decreases the efficiency of the photocatalytic system, the stability of $D^{\bullet+}$ has a critical effect on the activity, and it should be sacrificially decomposed to prevent the oxidation of $PS^{\bullet-}$. Another critical point for consideration is that the final oxidation product of the sacrificial electron donor may react with the catalyst and PS intermediate species to decrease the photocatalytic activity. Triethylamine (E_{ox} = 0.96 V vs. SCE in benzene) and triethanolamine (E_{ox} = 0.80 V vs. SCE in acetonitrile) are the well-known sacrificial electron donors for photocatalytic CO_2RR and HER [49].

1.11 Metal Dicyanamides for CO_2RR and HER

Dicyanamide (dca), $[N(CN)_2]^-$, is an N−donor bridging group, which forms polymeric compounds with transition metals by using its nitrogen atoms for coordination. It is considered a pseudo-halide as it displays chemical and coordination properties similar to group 17 anions [147]. The dca anion is a relatively weak field ligand compared to the cyanide anion, which stabilizes high spin states. Unlike the well-studied cyanide ligand, which can only accept one coordination mode, this ligand can adopt a variety of coordination modes in its chemistry: i) monodentate via one of the nitrile nitrogen atoms (Figure 19a), ii) bidentate through both nitrile N atoms (Figure19b), or one nitrile and the central amide N atom (Figure 19c), iii) tridentate through both nitriles and the amide N atom (Figure 19d), and v) tetradentate, in which the central amide and one of the nitrile nitrogen atoms are μ−coordinated, and the remaining nitrile atom is bis-bidentate to two separate metal ions (Figure19e) [148], [149].

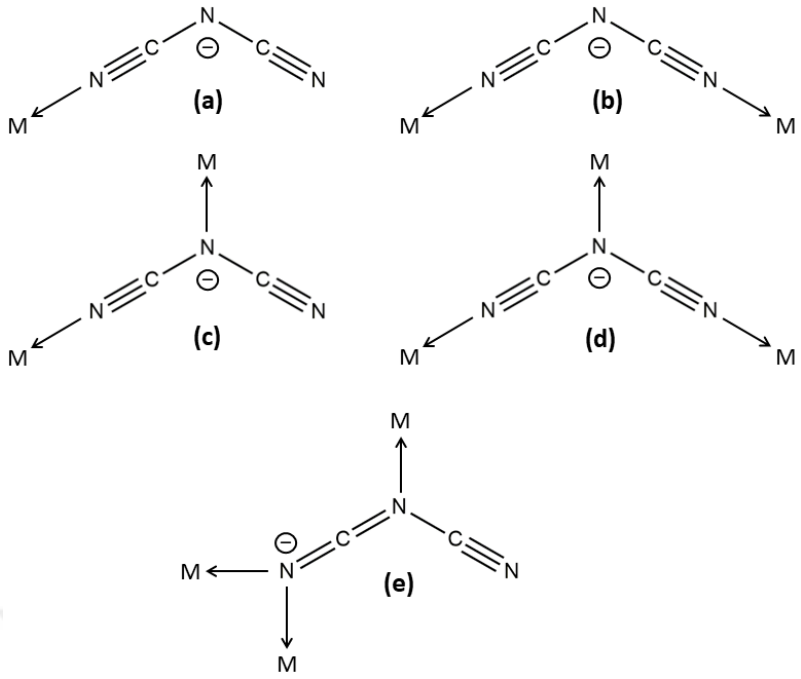

Figure 19. Dicyanamide coordination modes.

The structure of $Co(dca)_2$ contains 3D networks of octahedral metal ions connected by μ−dca ligands. The network is similar to that of rutile (TiO_2), consisting of four nitrile nitrogen atoms in the equatorial plane and two axially-bonded amide-N atoms from six different dicyanamide ligands (Figure 20). The Co–N (amide) bonds are longer than the Co–N (nitrile), while the difference is less than 0.1 Å [150], [151]. Furthermore, a relatively short dicyanamide bridging ligand allows magnetic and electronic communication between metal ions. This communication also provides partial electron transfer between neighboring metal ions, utilized for electrocatalytic and magnetic studies [147], [152].

While a single semiconductor may perform both light-harvesting and catalytic functions, the majority of published systems consist of a light-absorber component combined with a catalyst such as a metal complex, an enzyme, or inorganic particles [25]. For a long time, most studies in the field of visible-light-driven CO_2RR and HER have used ruthenium-based complexes as the PS due to their unique redox and photochemical properties [49], [50], [153]–[160].

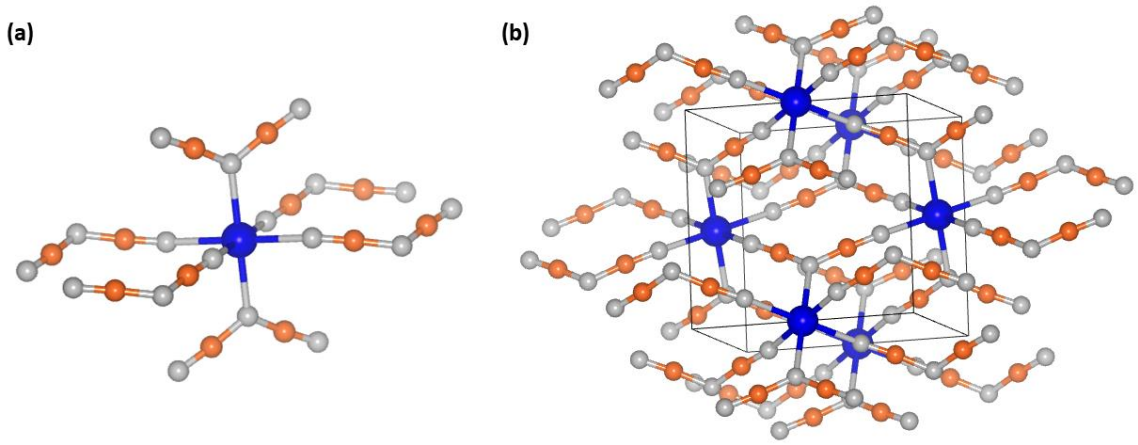

Figure 20. (a) Coordination of the triply coordinating dicyanamide anion to Co, (b) 3D structure of $Co(dca)_2$ (Color code: Co = blue; C = gray; N = orange).

Thus, the photocatalytic performance of several cobalt-containing compounds has been evaluated in the presence of a $[Ru(bpy)_3]^{2+}$ (bpy = 2,2′-bipyridine) PS/a sacrificial electron donor pair[55], [60], [168], [169], [76], [161]–[167]. Given the partial electron delocalization and the proper coordination environment of cobalt ions in cobalt dicyanamide (Co-dca), we aim to utilize a dicyanamide-based coordination polymer for photocatalytic CO_2 reduction and hydrogen evolution for the first time. The photocatalytic activity of a 3D coordination compound, $Co(dca)_2$, was investigated in the presence of $[Ru(bpy)_3]^{2+}$ as the light-harvesting component and various sacrificial electron donor agents.

1.12 Thesis Outline

Chapter 2 provides detailed information about the characterization methods used in this thesis, including materials characterizations, optical characterizations, photocatalytic experiments, and photoelectrochemical measurements. A brief explanation of the theoretical background is also included.

In chapter 3, ZnCr-LDH as the SC and CoFe-PBA as the WOC were combined to afford an earth-abundant photocatalytic hybrid structure. The experimental parameters, including the weight ratio of components, are investigated and optimized. Moreover, the band energy structure of hybrid assembly is extracted from optical and electrochemical results.

In chapter 4, the CoFe-PBA water oxidation catalyst is coupled with Dion−Jacobson type niobate nanosheets, which produces a p−n junction. The semiconductor–catalyst hybrid structure is characterized, and photocatalytic performance is investigated. Furthermore, photoelectrochemical studies are performed to understand the electron transfer mechanism.

Chapter 5 presents our first study on the Co-dca coordination network as a catalyst. For the first time, the catalytic activity of Co-dca for the CO_2RR is evaluated in the presence of a ruthenium-based PS. A series of photocatalytic experiments under various reaction conditions are performed to display the role of the PS, the scavenger, and the solvent in the selectivity and the activity of the catalyst.

In chapter 6, Co-dca is also studied as a hydrogen evolution catalyst in the presence of a Ru PS and triethylamine as a sacrificial electron donor. We also explore the structural and morphological effects of triethylamine on the Co-dca network.

Chapter 2

Characterization Methods and Instrumentation

This chapter offers an overview of various experiments and characterization techniques, along with the theoretical background required to understand the measurements performed.

2.1 Material Characterizations

For structural characterization of as-synthesized and post-catalytic samples, we used the following instruments:

***X-ray diffraction (XRD)*:** Crystallographic structures of materials were determined by a Pananalytical X'PertPro multipurpose X-ray diffractometer (MPD) with Cu K_α X-ray radiation (λ = 1.5405 Å) operating at 45 kV/40 mA. The powder samples were pressed into a silicon single crystal and placed in the diffractometer to be scanned within the range of 3−80° with a scan rate of 0.04 deg s^{-1}.

***Attenuated total reflectance−Fourier transformed infrared (ATR−FTIR) spectroscopy*:** The ATR-FTIR measurements were carried out by a Bruker Alpha Platinum-ATR spectrometer with a diamond sample holder. The spectra were collected in transmittance mode with a resolution of 4 cm^{-1}, 64 scans/spectrum, and a wavenumber range of 400 to 4000 cm^{-1}.

***X-ray photoelectron spectroscopy (XPS)*:** XPS measurements were performed using a Thermo Scientific K-Alpha X-Ray Photoelectron Spectrometer system equipped with an Al K_α micro-focused monochromator source and accompanied by a flood gun for charge neutralization. All spectra were conducted using the aluminum anode (Al K_α = 1486.6 eV), which operates at a 400 µm spot size. The survey spectrum was obtained with a pass energy of 200 eV and a step size of 1 eV. In order to get high-resolution spectra, pass energy of 30 eV was employed, with a step size of 0.1 eV. Powder samples were spread on a conducting copper tape for measurement.

***Scanning electron microscopy (SEM)*:** The morphology and chemical composition of the samples were examined by an SEM (FEI−Quanta 200 FEG ESEM) with an energy dispersive X-ray spectrometer (EDS) analyzer. Powder samples were placed on carbon tape for measurement.

***Transmission electron microscopy (TEM)*:** TEM, scanning transmission electron microscopy (STEM), and high angle annular dark field (HAADF) imaging were carried out at 300 kV using an FEI Technai G2 F30 transmission electron microscope. For the sample preparation, powder samples were dispersed in ethanol and dropped on a carbon-coated copper grid. For elemental analysis, EDX was performed with 100 keV incident electron energy.

2.2 Optical Characterizations

The interaction between light and materials may also provide valuable information about samples. To understand the light-dependent processes, we have employed below optical methods:

***Ultraviolet−visible (UV−Vis) spectroscopy*:** The optical absorption properties of the samples were studied via UV−Vis spectroscopy using a Cary 5000 UV−A−VIS−NIR

spectrometer equipped with a Varian Cary 2500 Internal Diffuse Reflectance (DR) accessory. The spectra were obtained in a wavelength range of 200−800 nm with a scan rate of 600 nm min^{-1}. The spectra of powder samples were recorded in diffuse reflectance mode.

***Kubelka−Munk transformation*:** One of the typical methods for determining the optical band gap of materials is the diffuse reflectance technique, where the propagation of light through inhomogeneous media results in light scattering [170]. For this aim, the UV−Vis spectra of powder samples were collected in diffuse reflection mode, and the Kubelka−Munk model extracted the absorption value of the materials. The well-known Kubelka-Munk function $F(R_\infty)$ is:

$$F(R_\infty) \equiv \frac{(1 - R_\infty)^2}{2R_\infty} = \frac{K}{S} \quad (6)$$

In this equation, $R_\infty = \frac{R_{sample}}{R_{standard}}$ is the reflectance, K is the Kubelka−Munk absorption constant, and S is the Kubelka-Munk scattering constant (The ∞ subscript indicates that the sample is infinitely thick, which means that none of the irradiated light penetrates to the bottom of the sample holder) [170]–[172].

***Band gap energy determination*:** The optical band gap energy of materials can be estimated by converting the Kubelka−Munk absorption data into Tauc's plot using:

$$(\alpha h\nu)^{1/n} = A(h\nu - E_g) \quad (7)$$

where α, h, ν, A, and E_g are the absorption coefficients, Planck constant, light frequency, the proportionality constant, and band gap energy, respectively. The exponent n indicates the transition properties in a semiconductor, where n = 1/2 and n = 2 are used for direct and indirect transitions, respectively. The band gap energy was found by extrapolating the linear part of the curve to the x-axis [171].

***Photoluminescence (PL) spectroscopy*:** The PL spectra were conducted using a Jobin-Yvon Horiba Fluorolog-3 equipped with a Hamamatsu R928 P detector and a 450 W ozone-free Osram XBO xenon arc lamp. The spectra were recorded by dispersing samples in water using a quartz cuvette.

2.3 Photocatalytic Experiments

In order to detect evolved gas during the photocatalytic experiments, a quartz round-bottom flask capped with septa was used as the reactor. In a typical experiment, the reactor was filled with an appropriate solution and a certain amount of materials (detailed information about the solution and containing materials are explained in the experimental procedure of each chapter). The reaction solution was degassed by bubbling N_2 (for OER and HER) or CO_2 (for CO_2RR) gas for 30 min before light irradiation. A Xe lamp (Sciencetech, Model SLB-300B, 300 W; AM 1.5 global filter) was used to simulate sunlight of 100 mW cm^{-2} (1 sun). A 420 nm long−pass filter was utilized for experiments carried out under visible light. The amount of generated gas was determined by injecting 100 μL of the reactor headspace into an Agilent 7829A gas chromatograph (Agilent Technologies, Wilmington, Delaware, USA). The GC was equipped with a thermal conductivity detector (TCD), one split/splitless inlet (2:1 split ratio), and an Agilent 19095P-MS0 column (30 m × 530 μm × 25 μm HP-PLOT MoleSieve 5 A). The oven temperature was set to 40 °C; the temperatures of both the inlet port and the detector were kept at 100 °C. Argon gas was used as the carrier gas at a flow rate of 4 mL/min. The injection was performed by a Hamilton SampleLock syringe (1750SL, volume 0.5 mL, needle size 22 ga bevel tip, and needle L 51 mm).

2.4 (Photo)electrochemical Measurements

(Photo)electrochemical measurements were performed using a Gamry Instruments Interface 1000 potentiostat/galvanostat. A standard three−electrode cell (Bob's cell) was used, with Ag/AgCl (3.5 M KCl) as the reference electrode, a Pt mesh as the counter electrode, and a fluorine doped tin oxide (FTO; 1 × 2 cm; 2 mm slides with 7 Ω sq^{-1} surface resistivity and ∼80% transmittance) as the working electrode. After the measurement, the applied potentials ($E_{Ag/AgCl}$) were converted to the normal hydrogen electrode (NHE) with the Nernst equation:

$$E_{NHE} = E_{Ag/AgCl} + E^{\circ}_{Ag/AgCl} \quad (8)$$

where E_{NHE} is potential estimated vs. NHE, $E_{Ag/AgCl}$ is measured potential vs. Ag/AgCl electrode, and $E^{\circ}_{Ag/AgCl} = 0.205$ V is the standard electrochemical potential of the Ag/AgCl electrode.

Before electrode preparation, the FTO slides were washed by ultrasonication for 10 min each in a basic soapy solution, deionized water, and isopropanol and then annealed at 300 °C for 30 min. The photoanodes were prepared by a drop-casting method. A suspension of the photocatalyst powder (2 mg) and methanol (200 μL) was prepared by ultrasonication for 30 min. Subsequently, 30 μL of the suspension was dropped uniformly on the FTO slide (1 cm^2), and dried at 75 °C. The $KCa_2Nb_3O_{10}$−containing electrode was annealed at 300 °C for 30 min. All (photo)electrochemical measurements were performed in 0.1 M phosphate buffer solution (PBS; pH 7) containing 0.5 M Na_2SO_4 or 1 M KNO_3 at room temperature. Prior to each experiment, the electrolyte solution was bubbled with N_2 gas for 15 min to remove dissolved O_2.

***Cyclic voltammetry (CV)*:** This method involves applying an external voltage at a specific scan rate and recording the output current as a function of this bias. Note that the

applied potential is cycled, i.e., the electrode is alternately reduced and oxidized. This technique demonstrates the typical oxidation and reduction peaks of materials, along with their reversibility. CV measurements were accomplished under dark conditions and at a scan rate of 50 mV s^{-1}. 5 CV scans were performed to achieve a stable response.

***Chronoamperometry (CA)*:** The CA experiment measures the steady-state current at a fixed voltage as a function of time. CA measurements were performed under chopped illumination at a fixed potential of 1 V (vs. NHE).

***Mott−Schottky Analysis*:** The flat band position of the samples can be determined by Mott−Schottky analysis with the following equation:

$$\frac{1}{C^2} = \frac{2}{\varepsilon_0 \varepsilon_r e N_D} \left[V - V_{FB} - \frac{k_B T}{e} \right] \quad (9)$$

where C is the interfacial capacitance, ε_0 is the vacuum permittivity, ε_r is the dielectric constant of the semiconductor, N_D is the carrier density, V is the applied voltage, k_B is Boltzmann's constant, T is the absolute temperature, and e is the electronic charge. The interception point of the linear region of the $1/C^2$ vs. the applied potential (V) curve with the horizontal axis corresponds to V_{FB} [173]. The Mott−Schottky experiments were performed at frequencies of 0.5, 1, and 5 kHz (the 1 kHz result was reported) with the voltage step of 50 mV, in which the R_s was assumed in series with C.

Chapter 3

Photocatalytic Water Oxidation by a Layered Double Hydroxide-Prussian Blue Analogue Hybrid Assembly

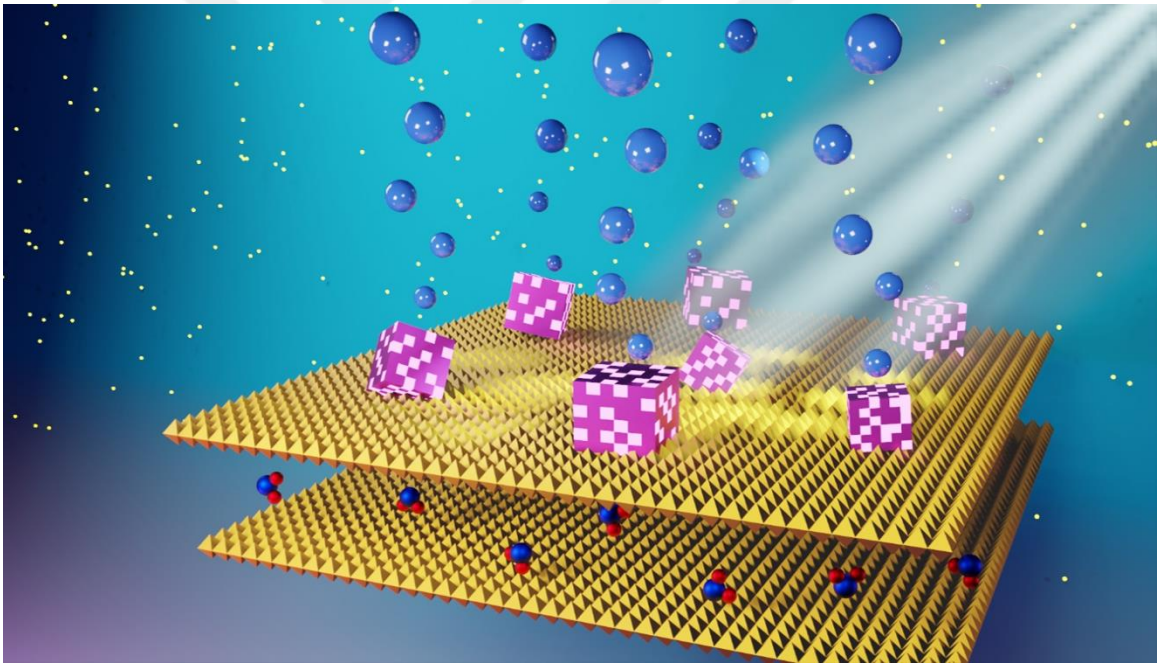

This chapter is based on the publication: **S. S. Akbari** and F. Karadas, "Precious Metal-Free Photocatalytic Water Oxidation by a Layered Double Hydroxide-Prussian Blue Analogue Hybrid Assembly," *ChemSusChem*, vol. 14, no. 2, pp. 679–685, 2021 (Reproduced with permission from John Wiley and Sons, Ref. [142] © 2021, Wiley-VCH GmbH).

3.1 Experimental Procedure

3.1.1 Materials

Zinc(II) nitrate hexahydrate ($Zn(NO_3)_2 \cdot 6H_2O$, Sigma Aldrich, 98%), chromium(III) nitrate nonahydrate ($Cr(NO_3)_3 \cdot 9H_2O$, Sigma Aldrich, 99%), sodium hydroxide (NaOH Sigma Aldrich, 99%), sodium carbonate (Na_2CO_3, Sigma Aldrich, 99%), cobalt(II) nitrate hexahydrate ($Co(NO_3)_2 \cdot 6H_2O$, Alfa Aesar, 99.9%), potassium hexacyanoferrate(II) ($K_3[Fe(CN)_6]$, Sigma Aldrich, 99%), sodium persulfate ($Na_2S_2O_8$, Sigma Aldrich, >99%), silver nitrate ($AgNO_3$, Sigma Aldrich, 99%), potassium nitrate (KNO_3, Sigma Aldrich, 99%), ethanol (EtOH). Potassium phosphate buffer solutions were prepared by 0.1 M KH_2PO_4 and 0.1 M K_2HPO_4 diluted in 500 mL deionized water with a pH close to 7. Deionized water (resistivity: 18 MΩ/cm) is used in all experiments.

3.1.2 Sample Preparation

***Synthesis of ZnCr-LDH*:** The co-precipitation method was used to synthesize ZnCr-LDH, similar to the reported procedure with slight modifications [113]. $Zn(NO_3)_2 \cdot 6H_2O$ and $Cr(NO_3)_3 \cdot 9H_2O$ with a Zn:Cr molar ratio of 2:1 were dissolved in 30 mL of deionized water (solution A). Then, solution A was titrated with another solution containing 1 M NaOH and 1 M Na_2CO_3 (solution B) until reaching pH 7−8 under vigorous stirring at room temperature. The resultant suspension was stirred for 4 h. Subsequently, the mixture was aged at 85 °C for 22 h. The purple slurry was separated by centrifugation, rinsed with deionized water, and finally dried at 75 °C.

***Synthesis of CoFe-PBA*:** CoFe-PBA was synthesized by a precipitation method [174]. First, 2 mmol of $K_3[Fe(CN)_6]$ was dissolved in 20 mL of deionized water. Then, an aqueous solution of $Co(NO_3)_2.6H_2O$ (3 mmol in 20 mL water) was added dropwise to the above

solution at room temperature. The obtained slurry was stirred for 1 h and left to stand overnight. The final precipitate was collected by centrifugation and washed thoroughly with water. The obtained solid was dried at 75 °C.

***Synthesis of LDH-PBA assemblies*:** For the preparation of LDH-PB assemblies, LDH and PBA powder samples with specific quantities were dispersed separately in a water/ethanol (1:1, v/v) mixture and sonicated for 30 min. Then, solutions were mixed with ultrasonication for 2 h. Subsequently, the mixture was stirred at 60 °C for 6 h (Figure 21). The resulting materials with 1:1, 2:1, and 2:3 weight ratios are denoted as LDH-PB-1, LDH-PB-2, and LDH-PB-3, respectively.

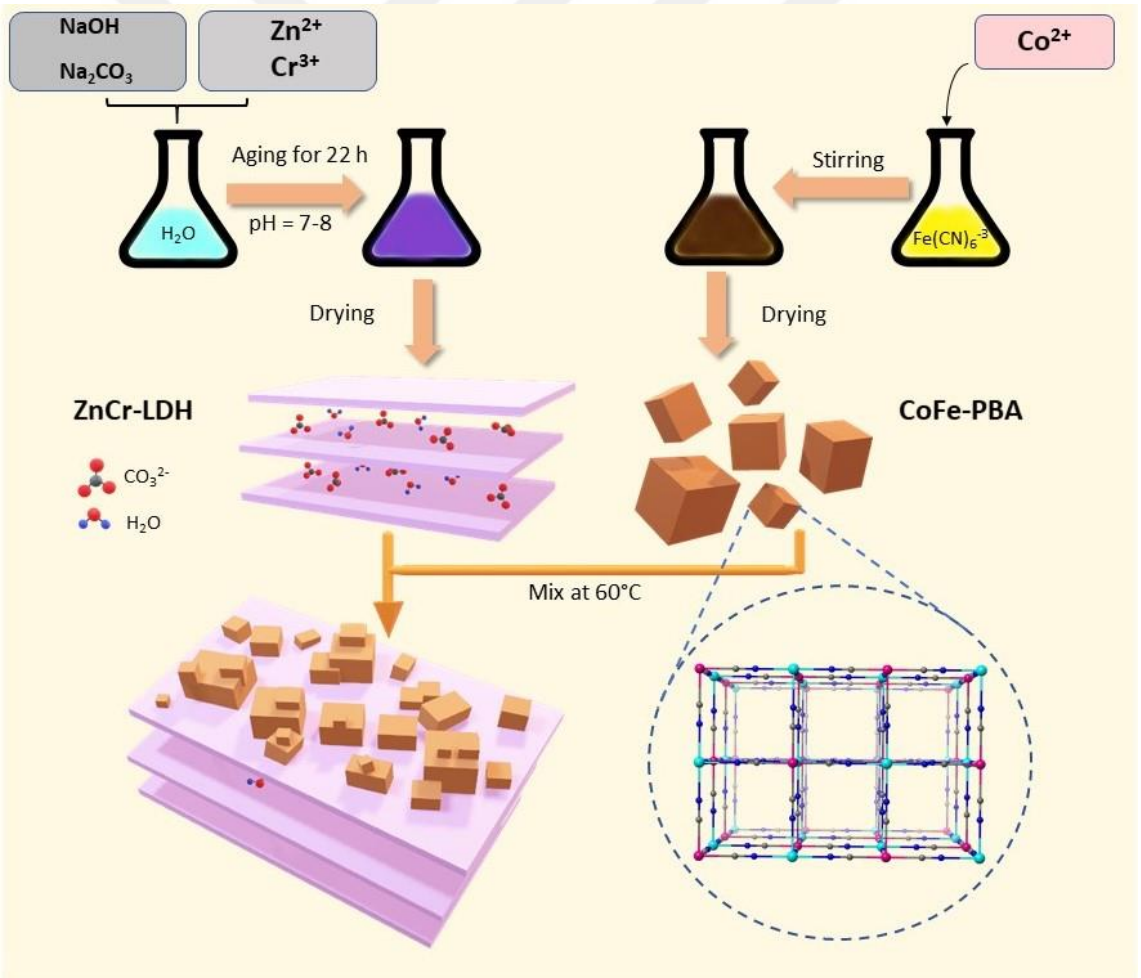

Figure 21. Schematic representation for preparing LDH-PB-n hybrid assemblies by mixing ZnCr-LDH and CoFe-PBA at 60 °C with different weight ratios.

3.1.3 Photocatalytic Experiments

The photocatalytic experiments for oxygen evolution were performed in a 21 mL Pyrex reactor. Catalysts (28 mg; 14 mg for experiments involving bare PBA and LDH samples) were dispersed in an aqueous buffer solution containing 5 mM $Na_2S_2O_8$ as a sacrificial agent. The headspace of the flask was sealed with septa, and the reaction mixtures were purged thoroughly with N_2 to remove air. A Xe lamp (300 W; AM 1.5 global filter.) with a UV cutoff filter ($\lambda > 420$ nm) was used as a light source. The amount of evolved oxygen was determined by injecting 100 μL of the reactor headspace gas into a GC. For each sample, photocatalytic tests were repeated 3 to 5 times to achieve reliable results.

3.2 Results and Discussion

3.2.1 Structural and Morphological Characterization of Materials

ZnCr-LDHs and CoFe-PBAs have been prepared according to previously reported synthetic methods. The compounds were then mixed at 60°C with different weight ratios to afford hybrid assemblies symbolized as LDH-PB-n (n = 1, 2, and 3). All characteristic peaks of an LDH and a PB structure were observed in powder XRD patterns of samples (Figure 22a). The diffraction peaks at 11.7° and 23.5° that are observed for ZnCr-LDH are assigned to (003) and (006) lattice planes of LDH structure, while the ones at 17.5° and 24.8° observed for CoFe-PBA correspond to (200) and (220) lattice planes of cubic PB structure, respectively (Table 1) [112], [174]. These peaks are also observed for LDH-PB-1 without any significant shift, which suggests a physical interaction between components in LDH-PB-1. The relative intensities of the diffraction peaks that belong to PB structures in LDH-PB-1 decrease, and they get broader compared to CoFe-PBA. The average particle size for (200) plane of PB was calculated for LDH-PB-1 and CoFe-PBA samples by the Scherrer equation:

$$d = 0.9\lambda / \beta \cos\theta \quad (9)$$

where β is the full width at half-maximum (FWHM) of the (200) plane, θ is the diffraction angle for the corresponding peak, and λ is the X-ray wavelength [175]. The results indicate that the particle size is reduced from 13 nm to 11 nm during the formation of the hybrid assembly.

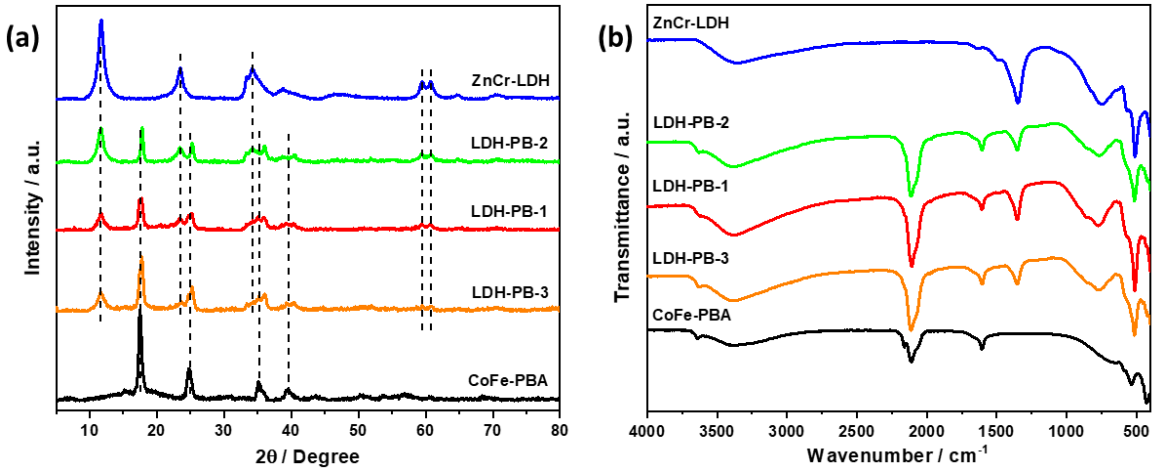

Figure 22. (a) XRD patterns, and (b) ATR-FTIR spectra of LDH, PBA, LDH-PB-1, LDH-PB-2, and LDH-PB-3 samples.

Table 1. Diffraction planes of samples and corresponding 2θ.

sample	Diffraction planes of ZnCr-LDH (degree)					Diffraction planes of CoFe-PBA (degree)			
	(003)	(006)	(009)	(110)	(113)	(200)	(220)	(400)	(420)
ZnCr-LDH	11.7°	23.5°	34.2°	59.5°	60.8°	-	-	-	-
CoFe-PBA	-	-	-	-	-	17.5°	24.8°	35.1°	39.6°
LDH-PB-1	11.6°	23.5°	34.2°	59.4°	60.7°	17.8°	25.2°	35.1°	39.6°
LDH-PB-2	11.6°	23.5°	34.2°	59.4°	60.7°	17.8°	25.3°	35.1°	39.6°
LDH-PB-3	11.7°	23.6°	34.2°	59.5°	60.8°	17.8°	25.2°	35.1°	39.6°

The FTIR spectra for ZnCr-LDH and LDH-PB-n reveal a broad band at 3370 cm^{-1} and a sharp one at 1632 cm^{-1}, which are attributed to the M–O–H stretching mode and the bending mode of H_2O. The broadness of the O–H band indicates the presence of hydrogen

bonds between water molecules and anions in the interlayer space of LDH. The two bands at 1487 cm^{-1} and 1348 cm^{-1} are assigned to the asymmetric stretching of the carbonate species placed in between the layers. The spectra for CoFe-PBA and LDH-PB-n reveal a sharp band at 2110 cm^{-1} with two shoulders at 2160 cm^{-1} and 2070 cm^{-1}, which are assigned to Co^{III}–NC–Fe^{II}, Co^{II}–NC–Fe^{III}, and Co^{II}–NC–Fe^{II} coordination modes, respectively. The relative decrease in the intensity of the shoulder at 2160 cm^{-1} for LDH-PB-n suggests an electron transfer from LDH to PBA structures (Figure 22b) [176], [177].

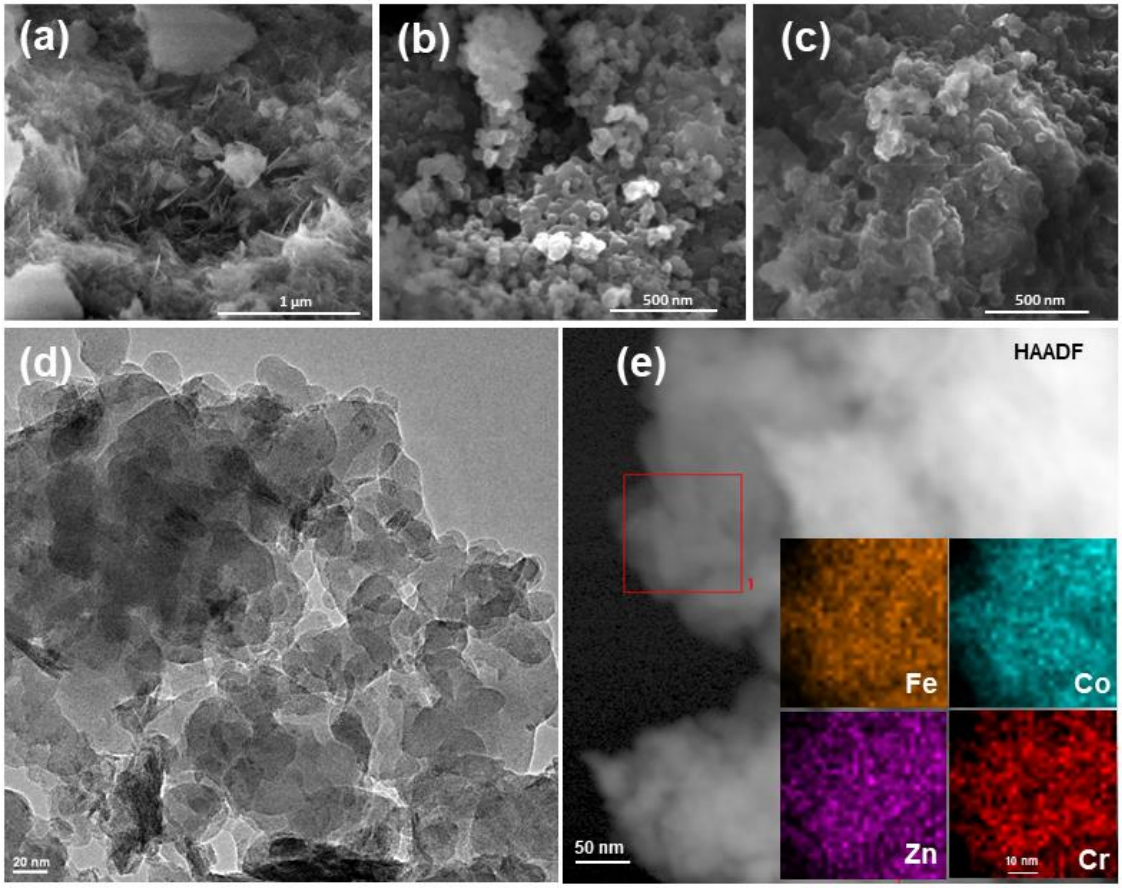

Figure 23. SEM images of (a) ZnCr-LDH, (b) CoFe-PBA, and (c) LDH-PB-1. (d) TEM images of LDH-PB-1. (e) High-angle annular dark field (HAADF) image of the LDH-PB-1 sample. The inset shows the selected area EDS elemental mapping.

The morphology and structure of the samples were investigated by SEM and TEM images. The layered structure of ZnCr-LDH was confirmed with SEM analysis (Figure

23a), which is surrounded by PB structures after mixing to produce hybrid assemblies (Figure 23b,c). The morphology of LDH-PB-1 has also been investigated with TEM analysis since it exhibits the highest photocatalytic water oxidation performance (Figure 23d). Scanning TEM (STEM) elemental mapping confirms that CoFe-PBA particles are distributed on the surface of LDH layers in LDH-PB-1 (Figure 23e) [113], [178].

EDS elemental scanning reveals an elemental ratio of Co:Fe and Zn:Cr as 3:2 and 2:1, respectively, which is consistent with our synthetic procedure. The decomposition of LDH during the photocatalytic experiment, as evidenced by the reduced quantity of Zn and Cr elements in the ZnCr-LDH post-catalytic sample, will be discussed in more detail in section 3.3.2. (Figure 24 and Table 2). EDS mapping indicates that the PB and LDH structures are well-dispersed to form a uniform hybrid assembly (Figure 25).

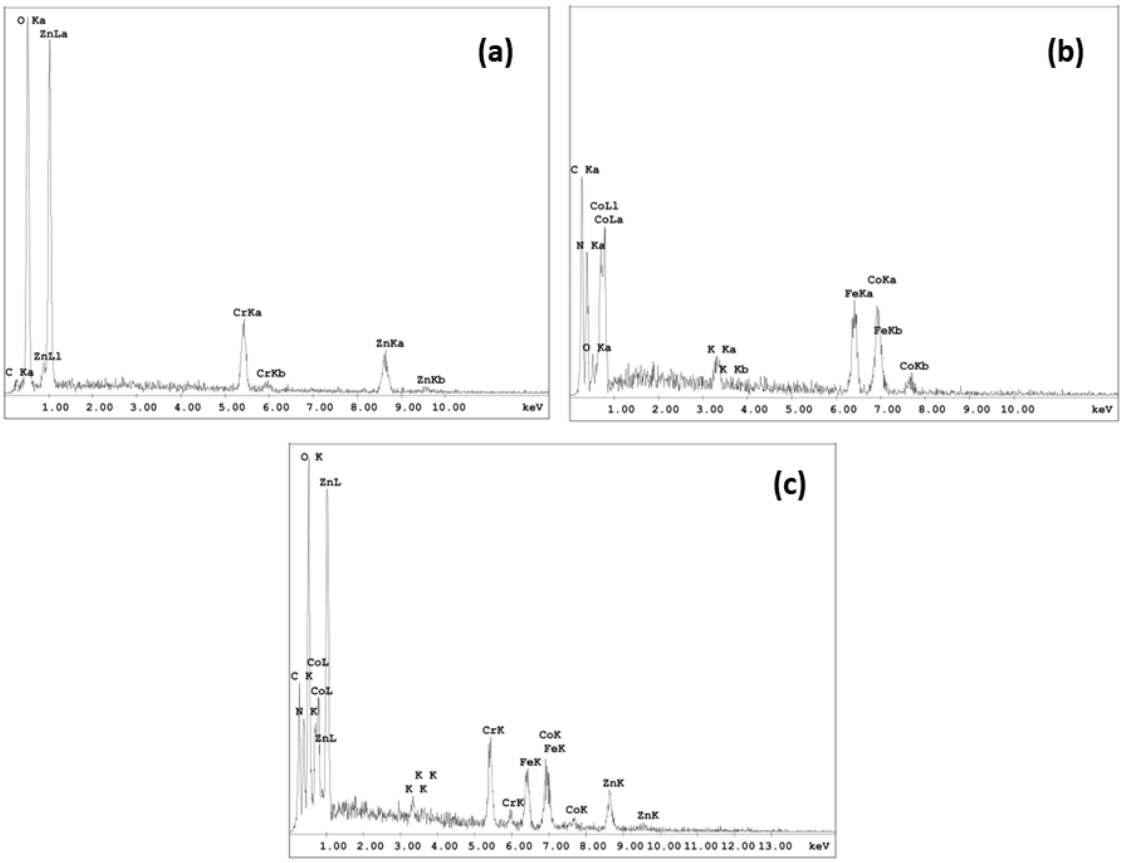

Figure 24. SEM−EDS analysis of (a) ZnCr-LDH, (b) CoFe-PBA, and (c) LDH-PB-1 samples.

Table 2. Atomic percent of elements for pristine and post-catalytic samples.

Sample	Co	Fe	Zn	Cr	C	N	O	K	P
CoFe-PBA	22	13	-	-	30	30	3	2	-
ZnCr-LDH	-	-	20	10	7	-	63	-	-
LDH-PB-1	6	4	7	4	27	21	30	1	-
ZnCr-LDH-postcat.	-	-	13	7	6	-	64	2	6
LDH-PB-1-postcat.	6	4	6	3	23	18	34	4	2

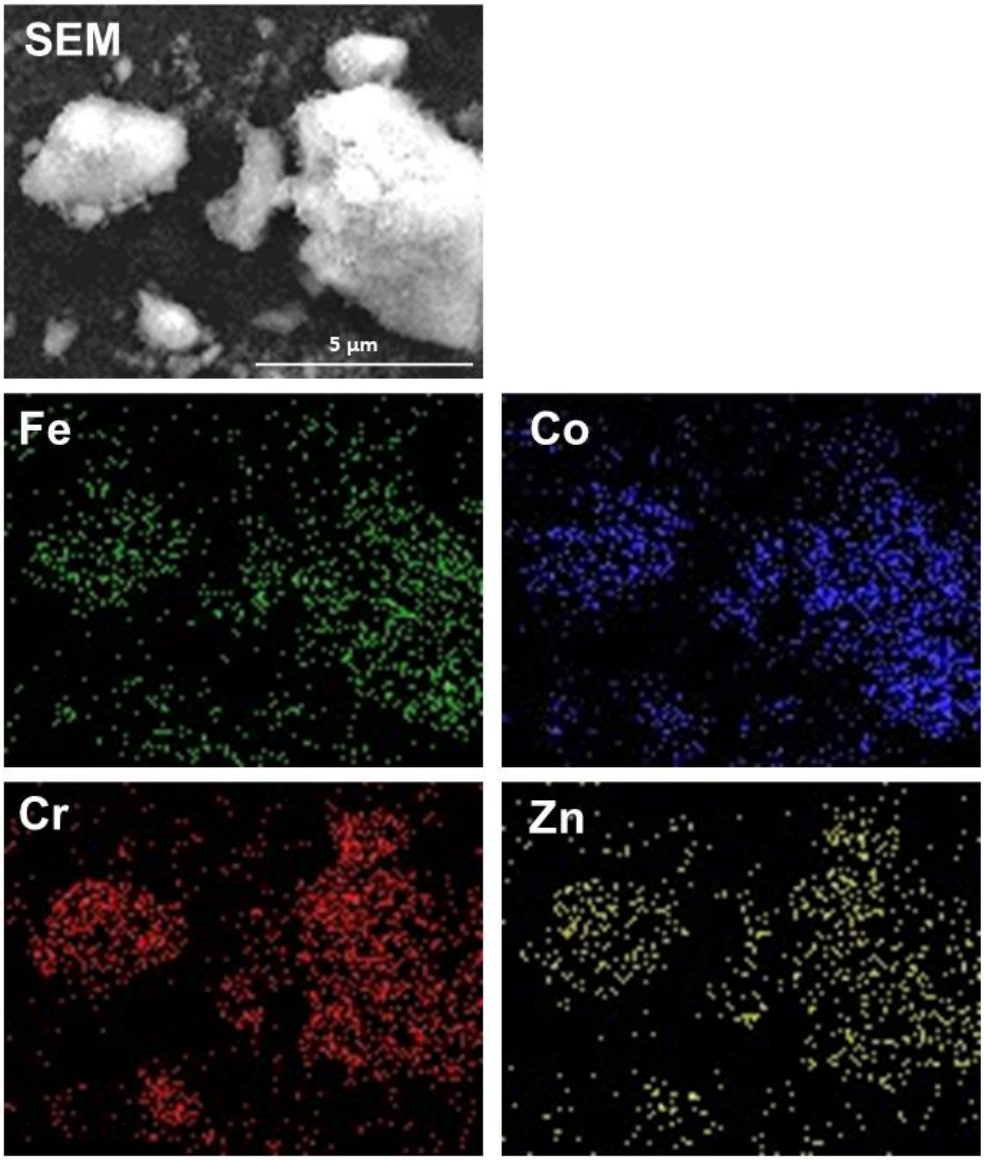

Figure 25. SEM image and related EDS elemental mappings of Fe, Co, Cr, and Zn for LDH-PB-1 sample.

The possible electron transfer between LDH and PB is also observed in XPS studies. Figure 26 shows corresponding binding energies for Co 2p, Fe 2p, N 1s, and C 1s, which are in good accordance with the expected profiles of CoFe-PBA. The Fe 2p spectrum consists of +2 and +3 oxidation states. The peaks at binding energies of 708.5 and 721.4 eV correspond to $2p_{3/2}$ and $2p_{1/2}$ of Fe^{2+}, and the $2p_{3/2}$ and $2p_{1/2}$ of Fe^{3+} are located at 710.1 and 723.6 eV, respectively [179].

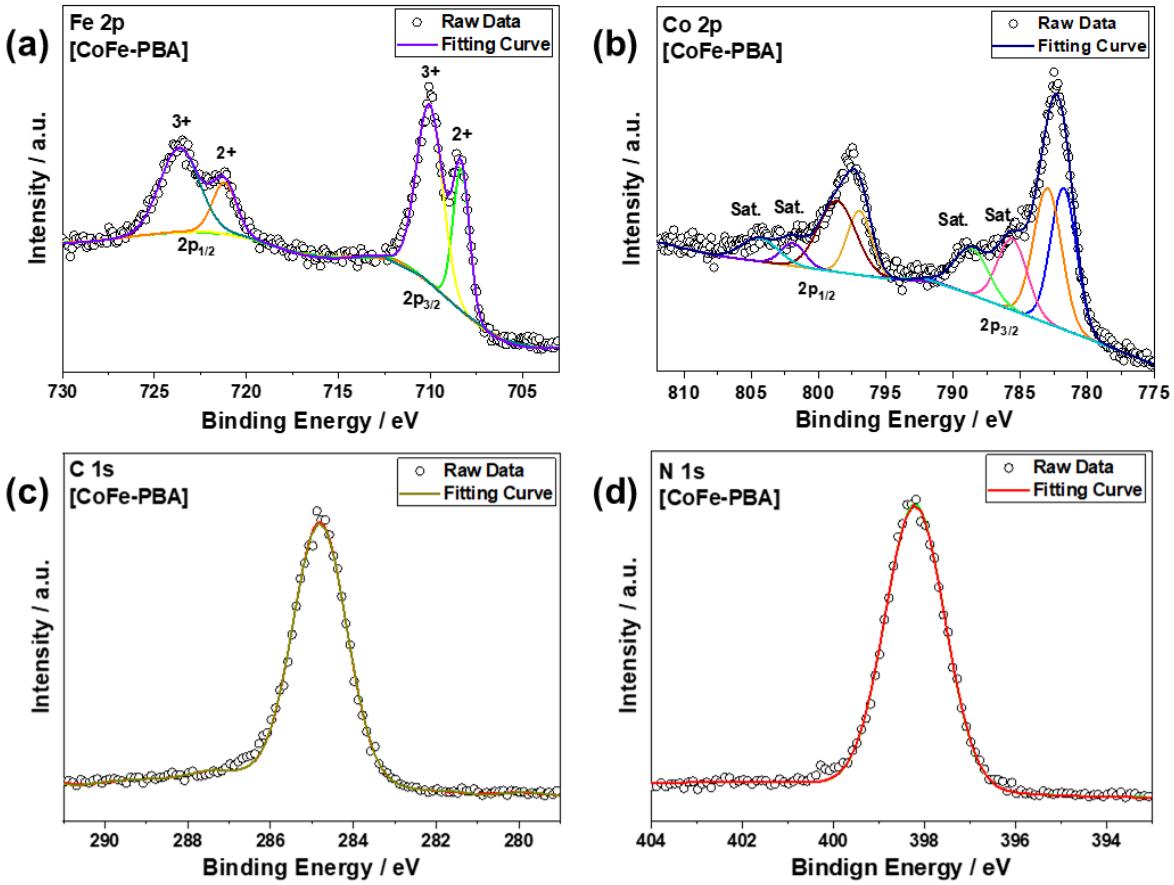

Figure 26. XPS spectra of the CoFe-PBA sample (a) Fe 2p, (b) Co 2p, (c) C 1s, and (d) N 1s. Circles and lines represent raw data and fitted curves, respectively.

The Co $2p_{3/2}$ and Co $2p_{1/2}$ signals have two main components with shake-up satellite peaks at higher binding energies. These satellite peaks suggest the existence of a Co^{2+} oxidation state in the PBA sample [180]–[182]. According to previous studies, the values of the $2p_{1/2}$–$2p_{3/2}$ peak separation for Co(III) and Co(II) complexes are 16 and 15 eV,

respectively [183]–[185]. The ΔE (ΔE = $2p_{1/2}$−$2p_{3/2}$) value of Co 2p spectrum is about 15.3 eV for CoFe-PBA sample, which is intermediate between Co(II) and Co(III) complexes [186]. These results indicate that cobalt cation involves both +3 and +2 oxidation states, which is in agreement with the presence of Co^{III}–NC–Fe^{II}, Co^{II}–NC–Fe^{III}, and Co^{II}–NC–Fe^{II} coordination modes in the FTIR spectrum of CoFe-PBA sample.

The XPS spectra of bare ZnCr-LDH are shown in Figure 27. The Zn 2p spectrum displays two distinct peaks of Zn $2p_{3/2}$ and Zn $2p_{1/2}$ at binding energies of 1021.7 and 1044.9 eV, respectively. The Cr 2p doublet (Cr $2p_{3/2}$ and Cr $2p_{1/2}$) are located at binding energies of 577.4 and 586.8 eV, respectively. Three peaks can fit the O 1s region: i) the lattice oxygen (530.2 eV), ii) the hydroxyl group (531.3 eV), and iii) the carbonate oxygen (532.3 eV) [187].

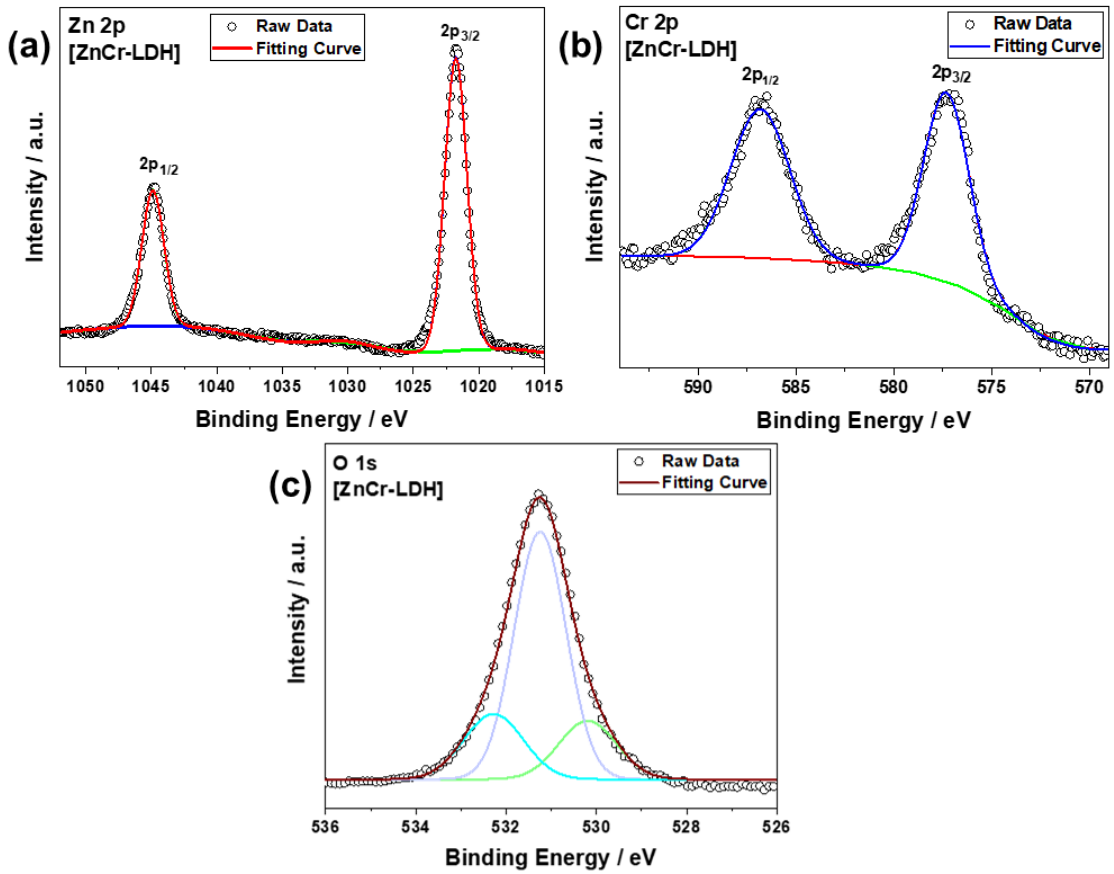

Figure 27. XPS spectra of the ZnCr-LDH sample (a) Zn 2p, (b) Cr (2p), and (c) O 1s. Circles and lines represent raw data and fitted curves, respectively.

A comparison of XPS profiles before and after mixing indicates that the binding energies of Zn 2p and Cr 2p exhibit slightly positive shifts after mixing [115]. On the other hand, cobalt retains its +2 and +3 oxidation states, while the amount of Fe^{2+} ions in the mixed-valent iron sites increases upon mixing, suggesting an electron transfer from LDH to PBA structures (Figure 28) [85]. These results are in accordance with FTIR analysis, in which the intensity of the shoulder at 2160 cm^{-1} (Co^{II}–NC–Fe^{III} coordination mode) decreases while the intensity of the band at 2110 cm^{-1} (Co^{III}–NC–Fe^{II} coordination mode) increases after hybridization.

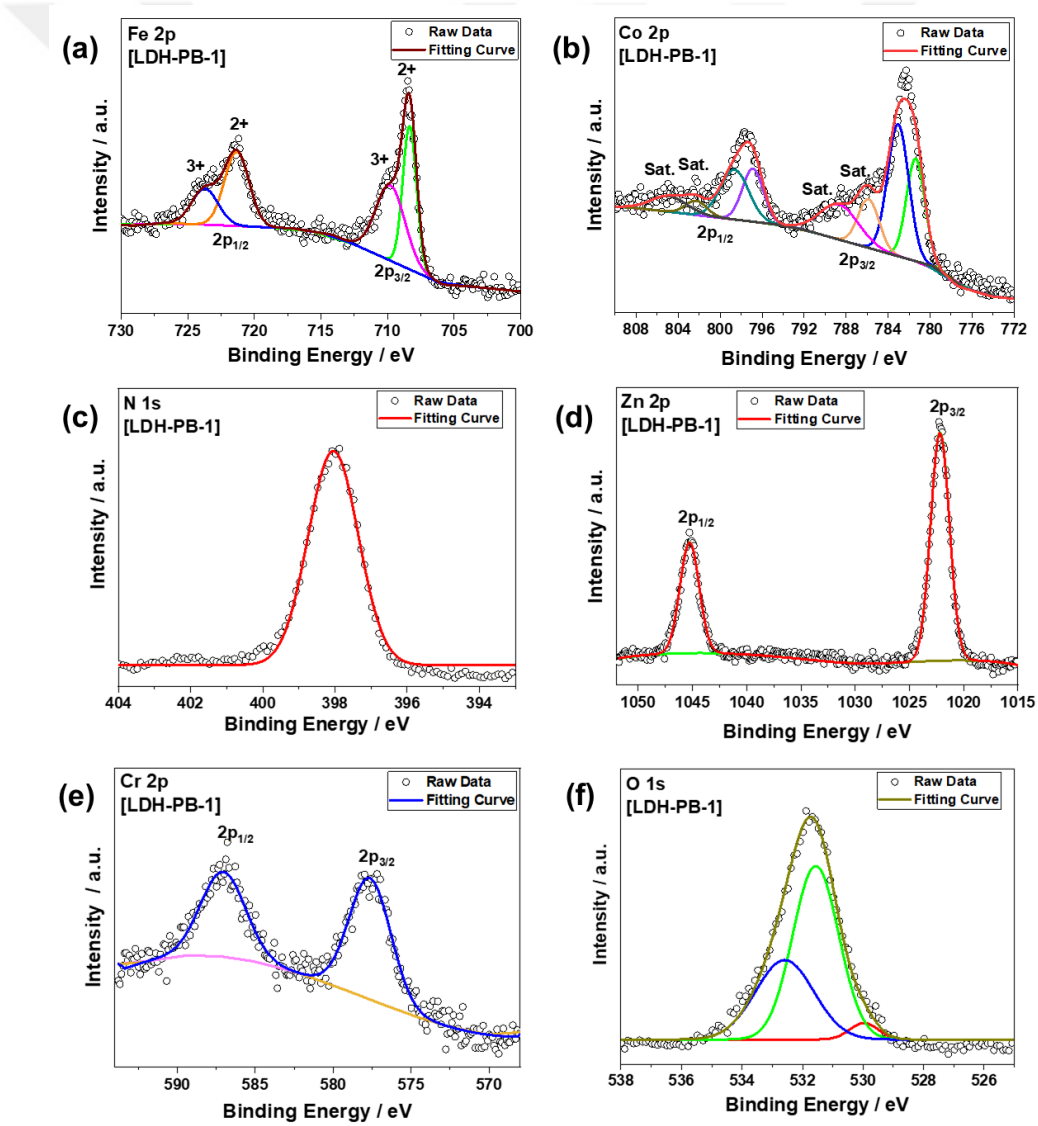

Figure 28. XPS spectra of the LDH-PB-1 sample: (a) Fe 2p; (b) Co 2p; (c) N 1s; (d) Zn 2p; (e) Cr 2p; (f) O 1s. Circles and lines represent raw data and fitted curves, respectively.

3.2.2 Photocatalytic Oxygen Evolution

The photocatalytic performances of bare LDH (14 mg) and LDH-PB-n (28 mg) samples were evaluated by monitoring the amount of generated oxygen from water in the presence of 5 mM $Na_2S_2O_8$ as a sacrificial agent under visible light irradiation (Figure 29a). ZnCr-LDH exhibits a considerable photocatalytic activity, which decreases gradually in the second cycle (0.64 mmol g^{-1} h^{-1}). LDH-PB-1 exhibits a three-fold increase in activity (1.83 mmol g^{-1} h^{-1}) compared to bare ZnCr-LDH and CoFe-PBA, which maintains its activity even during the third cycle (Figure 29b). The trend in the photocatalytic activity clearly shows that coupling a PBA structure as a WOC enhances not only the activity but also the stability of LDH structures under photocatalytic conditions. The highest photocatalytic activity and stability are obtained when the mole ratio of LDH to PBA is 1:1 (LDH-PB-1), which maintains its activity during a 6 h photocatalytic experiment.

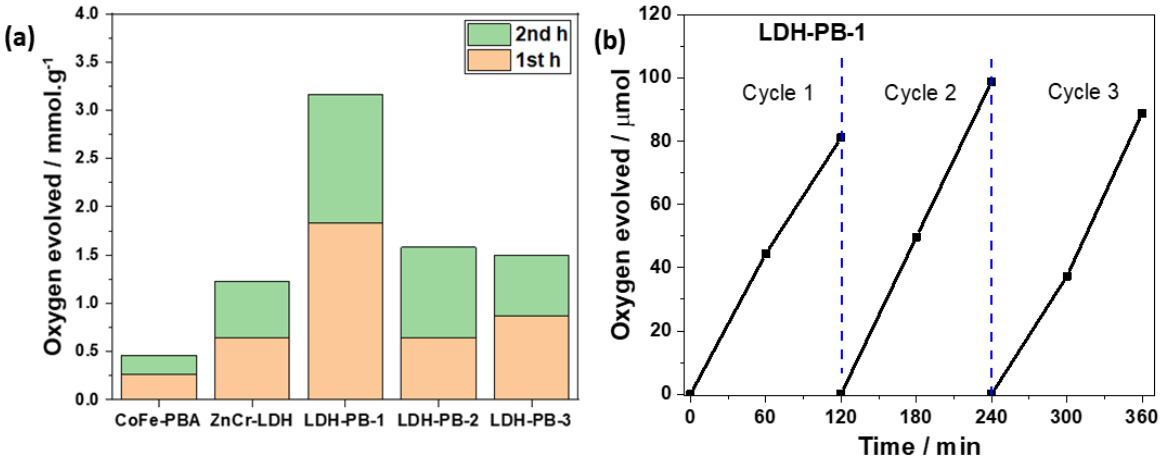

Figure 29. (a) Bar diagrams of photocatalytic O_2 evolution of CoFe-PBA, ZnCr-LDH and LDH-PB-1, LDH-PB-2, and LDH-PB-3 samples (mmol of produced O_2 per g of catalyst) in a pH 7 KPi buffer containing 5 mM $Na_2S_2O_8$ as a sacrificial agent under visible-light irradiation ($\lambda > 420$ nm). (b) Rate of O_2 generation in 3 consecutive cycles for LDH-PB-1. After each cycle, 5 mM $Na_2S_2O_8$ was added to the reaction solution.

When the mole ratio of the LDH component is two times higher than that of the PBA one (LDH-PB-2), the activity decreases to approximately half its value (0.64 mmol g^{-1} h^{-1}), which could be attributed to the decrease in the weight ratio of the catalyst in the assembly. On the other hand, for LDH-PB-3, which has a mole ratio of 2:3, the activity is ca. 0.87 mmol g^{-1} h^{-1} in the first cycle. The activity of LDH-PB-3 in the second cycle is, however, poorer (0.63 mmol g^{-1} h^{-1}) due to a possible photodecomposition. The lower stability in LDH-PB-3 could be attributed to a higher degree of aggregation of excess PB particles, which leads to a relatively inefficient electron transfer between components.

Furthermore, the physically mixed LDH+PBA sample displays a similar activity to LDH-PB-1 over the first cycle, which decreases significantly in the second cycle (Figure 30) due to the decomposition of the ZnCr-LDH structure (Figure 31). These studies indicate that both the synthetic method and the mole ratio of the components play an essential role in tuning the physical interaction between the components and, thus, in the activity and photostability.

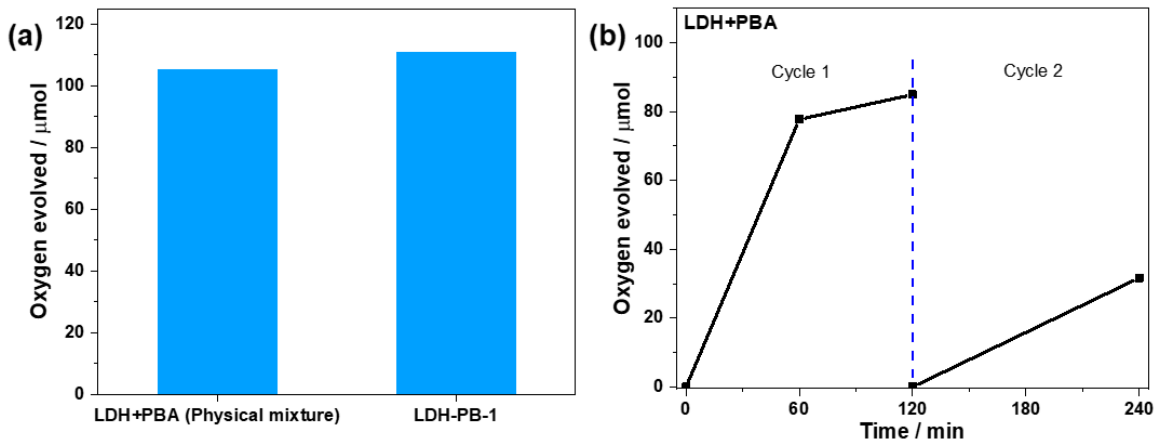

Figure 30. (a) Bar diagrams of photocatalytic O_2 generation of the physically mixed LDH+PBA and LDH-PB-1 samples after 2 h. (b) Rate of gas generation in 2 cycles for the physically mixed LDH+PBA sample.

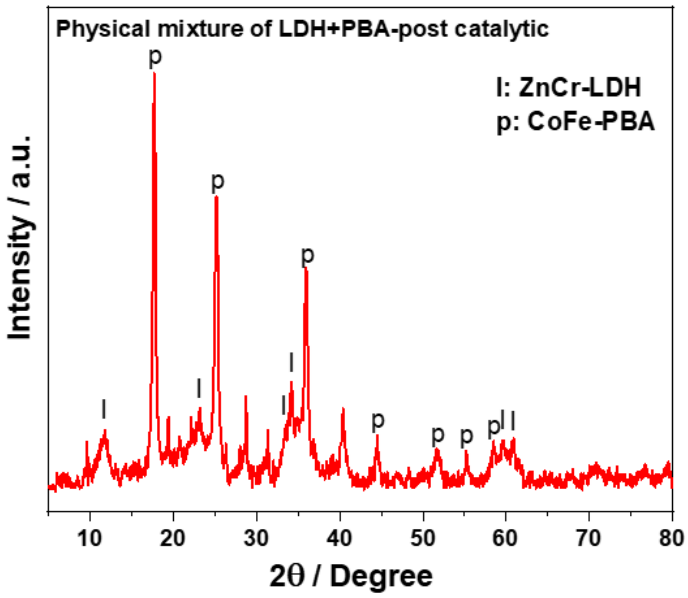

Figure 31. XRD pattern for post-catalytic of physically mixed LDH+PBA sample. "p" and "l" represent CoFe-PBA and ZnCr-LDH peaks, respectively. The additional peaks suggest the decomposition of the LDH structure.

We also studied the effect of the sacrificial agent by evaluating the photocatalytic activity of ZnCr-LDH and LDH-PB-1 with $AgNO_3$ as well. While ZnCr-LDH exhibits a similar activity in the presence of different sacrificial agents, the activity of LDH-PB-1 depends highly on the type of electron scavenger. The activity of LDH-PB-1 is around two times higher in $S_2O_8^{2-}$ compared to $AgNO_3$ (Figure 32). When an electron is added to persulfate, sulfate (SO_4^{2-}) and a sulfate radical ($SO_4^{\bullet-}$) are formed. The intermediate sulfate radical is a strong oxidant ($SO_4^{2-}/SO_4^{\bullet-}$, $E° > 2.4$ V vs. NHE), and it can extract an electron from the conduction band of a semiconductor. [188], [189].

Turnover frequency (TOF) is also an important indicator for comparing the activity of the catalytic site, which is defined as the number of O_2 or H_2 per active catalytic site per time [190], [191]. A rough molecular formula was extracted from EDS analysis for the lower-bound TOF value estimation, and all the cobalt sites are assumed to be catalytically

active. The TOF for LDH-PB-1 is obtained to be around 2.1×10^{-4} s^{-1}, which is comparable to previously reported TOF values for PB-based systems [85], [87], [88].

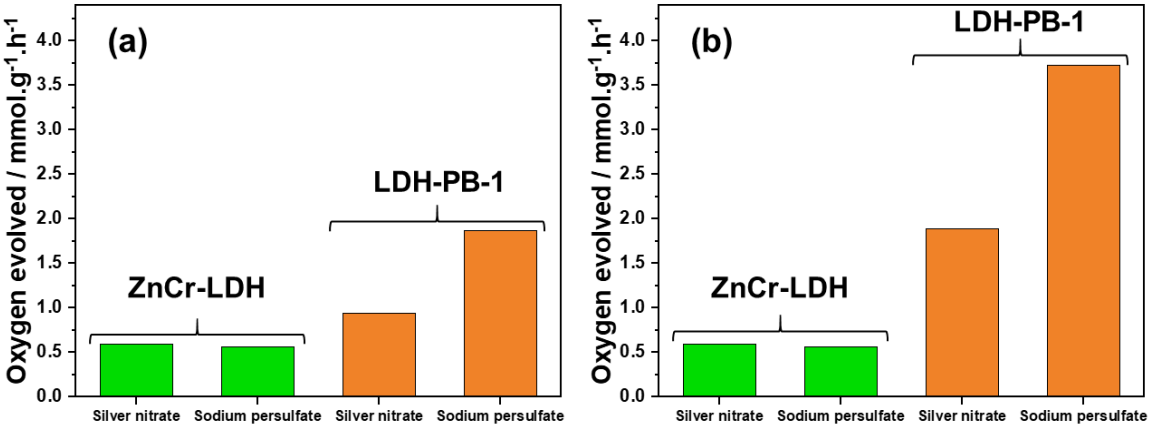

Figure 32. The comparison of $AgNO_3$ and $Na_2S_2O_8$ as the sacrificial agent. Bar diagrams of photocatalytic O_2 evolution of ZnCr-LDH and LDH-PB-1 samples (a) mmol of produced O_2 per g of the total amount of catalyst, (b) mmol of produced O_2 per g of ZnCr-LDH amount.

3.2.3 Optical Properties and Band Structure Estimation

The band structure and optical properties of ZnCr-LDH, CoFe-PBA, and mixed samples were investigated with UV−Vis diffuse reflectance spectroscopy (DRS). As plotted in Figure 33a, ZnCr-LDH exhibits two strong bands at 410 and 570 nm corresponding to the $^4A_{2g} \rightarrow {}^4T_{1g}$ (F) and $^4A_{2g} \rightarrow {}^4T_{2g}$ (F) d−d transition of chromium ions, respectively [109], [190], [192]. The absorption band initiated at 344 nm can be assigned to the ligand to metal charge transfer (LMCT) from the O 2p orbital to the Cr 3d(e_g) and Zn 4s orbitals [193]. When it is coupled with CoFe-PBA, the background absorption of the compound is significantly increased due to electronic coupling between ZnCr-LDH and PBA structures. Two broad absorption regions in CoFe-PBA can be attributed to the charge transfer in the structure [194].

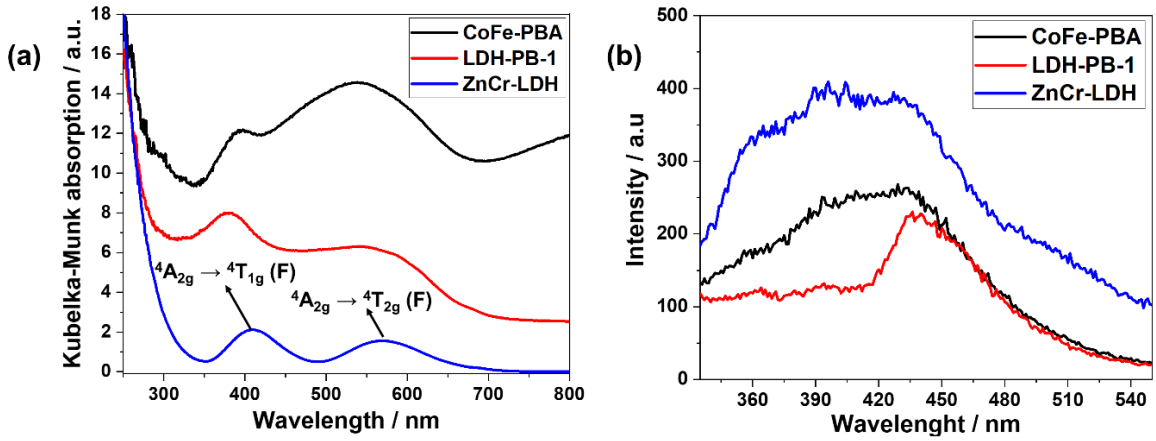

Figure 33. (a) Diffuse reflectance UV−Vis spectra (plotted as the Kubelka-Munk function of the reflectance, R) of CoFe-PBA, ZnCr-LDH, and LDH-PB-1 samples. (b) PL spectra of CoFe-PBA, ZnCr-LDH, and LDH-PB-1 samples (λ_{ex} = 290 nm) at room temperature.

The enhancement in the photocatalytic activity of the LDH-PB-1 sample is investigated by PL spectroscopy. In Figure 33b, ZnCr-LDH displays a remarkable depression of PL peaks upon hybridization with the PBA structure. Taking into account the higher visible light absorption of the LDH-PB-1 sample compared to the pristine LDH, the PL results suggest an efficient electron transfer between ZnCr-LDH and PBA components, which could sufficiently suppress the recombination of photo-generated electrons and holes [109], [195].

CV measurements and DRS results were evaluated to estimate the band energy diagram. The literature is contradictory on the assignment of band energy levels of ZnCr-LDH mainly due to the presence of $3d^3$ states of Cr^{3+} ions in addition to conduction and valence bands (Table 3). A cyclic voltammogram of ZnCr-LDH is utilized to assign the position for the d(t_{2g}) level, which can be 1.64 V or 1.92 V vs. NHE. In both cases, the d(t_{2g}) state of LDH is more positive than the HOMO level of CoFe-PBA, which is positioned at 1.48 V vs. NHE (Figure 34). Cyclic voltammograms of CoFe-PBA and ZnCr-LDH samples indicate that CoFe-PBA exhibits a much lower onset overpotential (~600 mV) for water oxidation than ZnCr-LDH (above 800 mV). Therefore, CoFe-PBA should

be the water oxidation catalyst in this hybrid assembly. The bandgap of ZnCr-LDH is found to be 3.97 eV based on the fitting of absorption data with Tauc's plot (Figure 35).

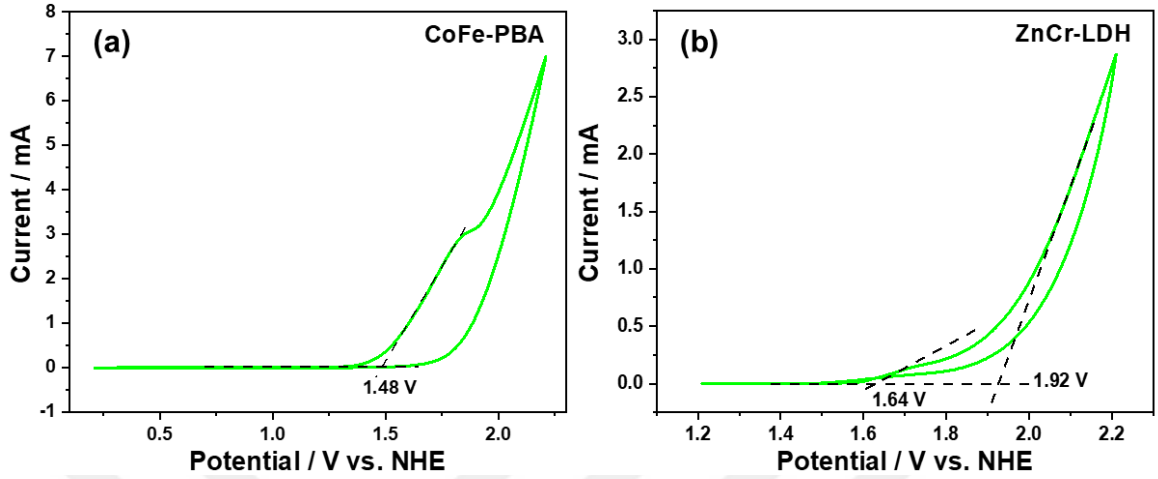

Figure 34. Cyclic voltammograms of (a) CoFe-PBA, and (b) ZnCr-LDH in KPi buffer 1 M KNO_3 solution at pH = 7 and 100 $mV.s^{-1}$ sweep rate.

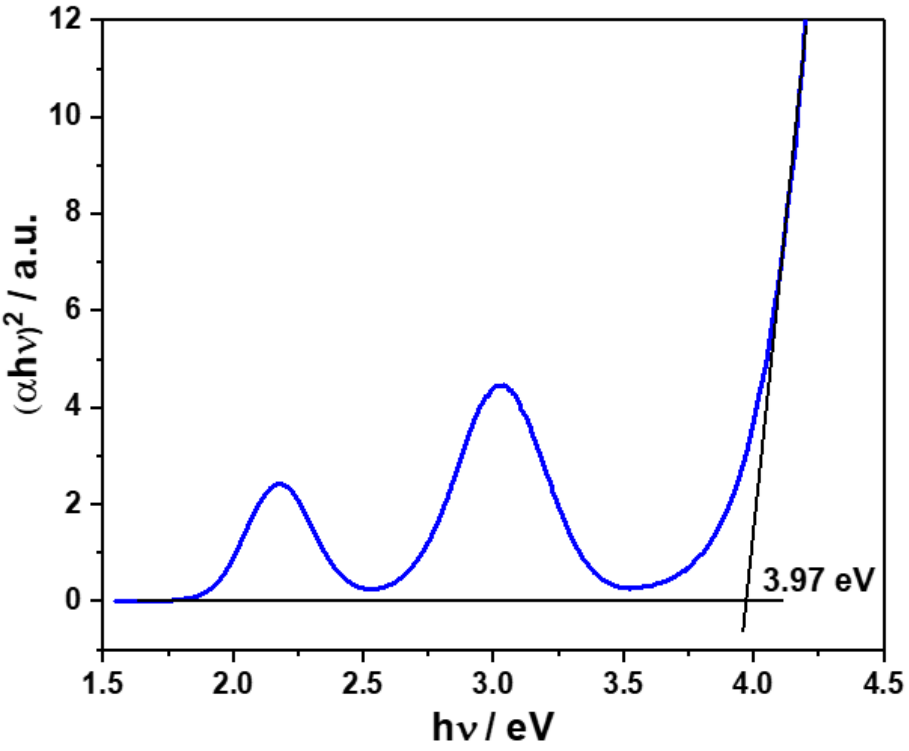

Figure 35. Tauc's plot of ZnCr-LDH for the estimation of the band gap.

Table 3. Band gap energy estimation of ZnCr-LDH in previous studies.

Photocatalyst	Estimated band gap energy	Ref.
ZnCr-LDH/titanate	~ 3 eV (d-d transition of Cr^{3+})	[109]
ZnCr-LDH	(From Cr-3d-t_{2g} to Cr-3d-e_g)	[111]
ZnCr-LDH/graphene	~ 3 eV (From O 2p to Cr 3de_g)	[116]
ZnCr-LDH/POM	~ 3 eV (From O 2p to Cr 3de_g)	[117]
ZnCr-LDH/graphene	2.12 eV (From Cr-3d-t_{2g} to Cr-3d-e_g)	[196]
ZnCr-LDH/CdSe	2.45 eV	[118]
Tb-ZnCr-LDH	2.3 eV	[112]
ZnCr-LDH/g-C_3N_5	2.76 eV (From O 2p to Cr 3de_g)	[197]
ZnCr-LDH/Cu_2O	2.52 eV	[114]
ZnCr-LDH (Theoretical)	2.63 eV (From O 2p to Cr d orbitals)	[104]
ZnCr-LDH/$Co(OH)_2$	2.5 eV (From O 2p to Cr 3d t_{2g})	[113]
ZnCr-LDH/Cu_2O	3.9 eV (MMCT from Cr 3d(t_{2g}) to Zn 4s)	[193]
ZnCr-LDH/MOF	2.6 eV (From O 2p to Cr 3d t_{2g})	[119]
WO_{3-X}/Ag/ZnCr LDH	2.5 eV (d-d transition of Cr^{3+})	[115]
ZnCr-LDH	1.93 eV	[198]

As illustrated in Figure 36, the HOMO level of PBA is located at a higher energy level compared to the d(t_{2g}) level of ZnCr-LDH. The electrons in d(t_{2g}) orbitals of LDH are excited to the unoccupied interband states by absorbing visible light. As a result, the photogenerated holes can be injected into the HOMO level of PBA, which causes an efficient charge separation.

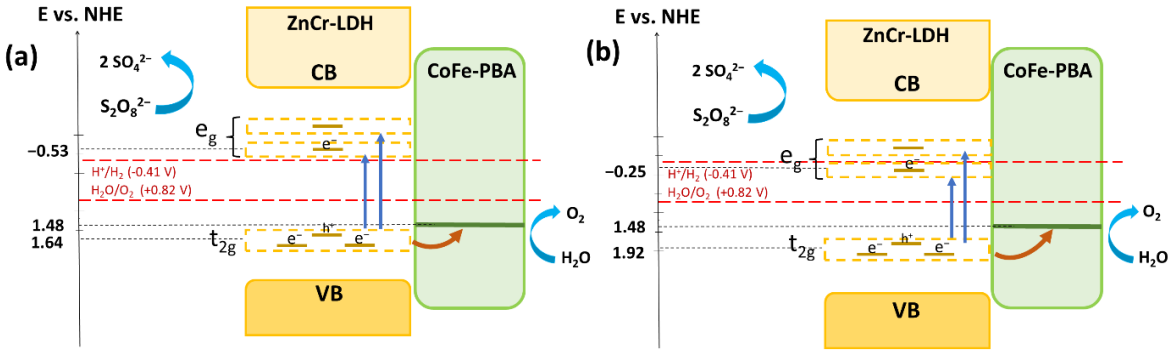

Figure 36. A schematic illustration for the estimated band structure of the LDH-PB-1 sample (pH = 7), when the d(t_{2g}) level of LDH is assumed to be located at (a) 1.64 V, and (b) 1.92 V vs. NHE.

3.2.4 Post-catalytic Studies

The robustness of the hybrid assembly is elucidated with XPS and XRD studies performed on post-catalytic powder samples. For the Cr 2p and Zn 2p bands, a slight shift to higher binding energy was observed. On the other hand, the corresponding Fe^{3+} peaks are diminished significantly, while those of Fe^{2+} remain unchanged. These results support the thesis that electron transfer occurs between LDH and PBA during the photocatalytic water oxidation process, reducing Fe^{3+} to Fe^{2+}. No significant change in the Co 2p profile is observed in pristine and post-catalytic samples, indicating the stability of the Co^{2+} sites (Figure 37a-d).

XRD patterns were also studied for pristine and post-catalytic powder samples of CoFe-PBA, ZnCr-LDH, and LDH-PB-1. Similar to previous studies, the CoFe-PBA sample was

observed to be stable during the photocatalytic water oxidation process based on the comparison of XRD profiles of pristine and post-catalytic CoFe-PBA samples (Figure 38a). ZnCr LDH, however, exhibits additional peaks in the post-catalytic sample, which reveals that it decomposes partially to $K_2Zn_4O(CrO_4)_4.3H_2O$ under photocatalytic conditions (Figure 38b). The decrease in the activity of ZnCr-LDH in the 2nd cycle could, thus, be attributed to its low stability. On the other hand, for LDH-PB-1, all the peaks obtained in the pristine and post-catalytic samples correspond to those for PB cubic and LDH structures (Figure 38c). It should be noted that a possible decomposition to an amorphous structure cannot be ruled out merely based on XRD studies.

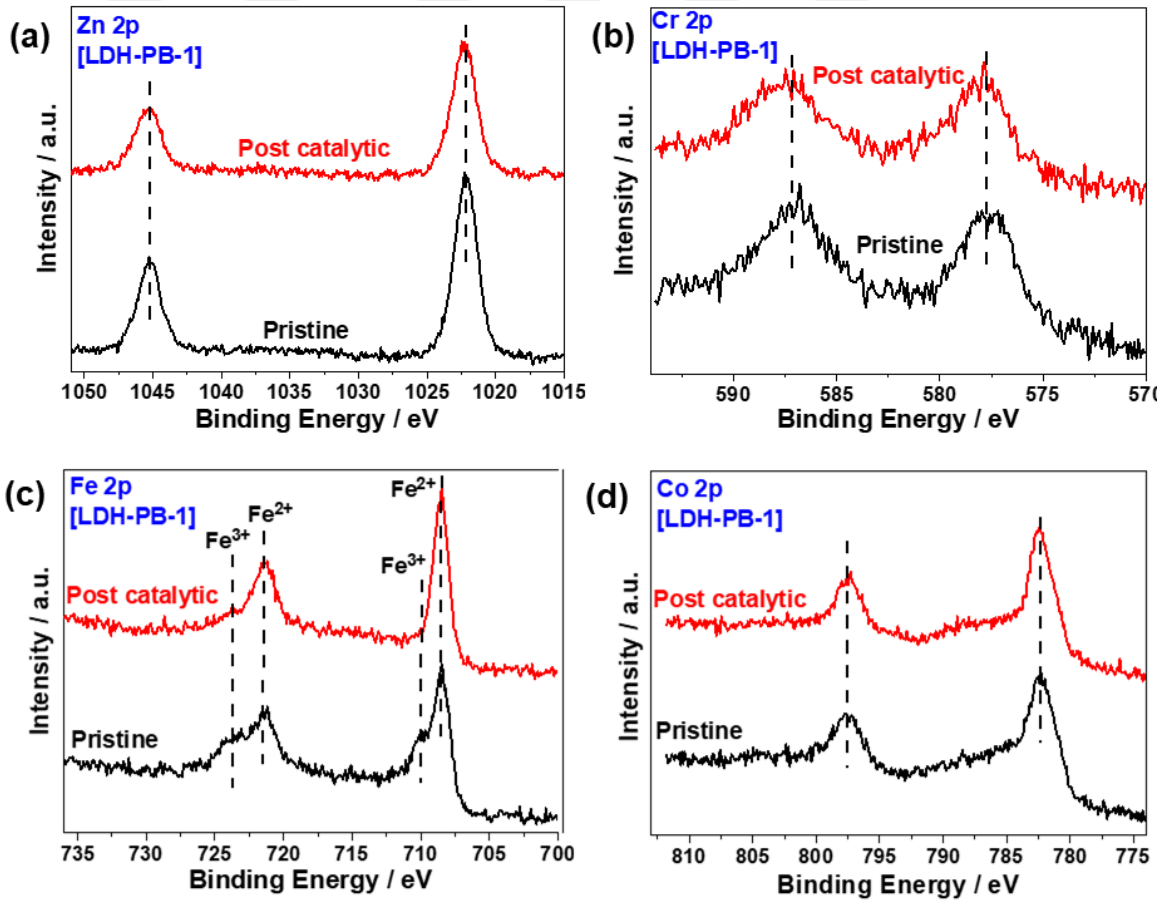

Figure 37. XPS spectra of (a) Zn 2p, (b) Cr 2p, (c) Fe 2p, and (d) Co 2p for pristine (black line) and post-catalytic (red line) of LDH-PB-1 sample.

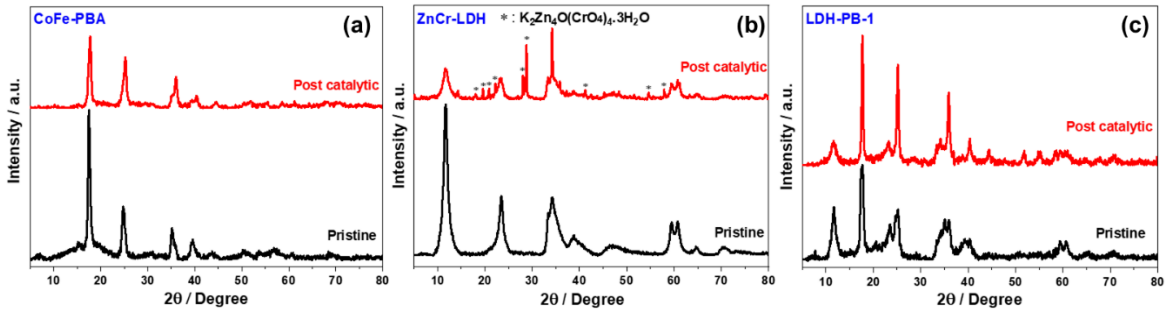

Figure 38. XRD patterns of (a) CoFe-PBA, (b) ZnCr-LDH, and (c) LDH-PB-1 for pristine (black line) and post-catalytic (red line) samples.

The steady profile of the photocatalytic activity throughout several cycles with LDH-PB-1 and XRD studies performed on pristine and post-catalytic CoFe-PBA, ZnCr-LDH, and LDH-PB-1 samples reveal that the LDH structure exhibits a remarkable enhancement in the stability once it is coupled with CoFe-PBA to form LDH-PB-1. No additional peaks that can be attributed to a decomposed product are observed in the Infrared spectra of pristine and post-catalytic samples for ZnCr-LDH and LDH-PB-1 (Figure 39).

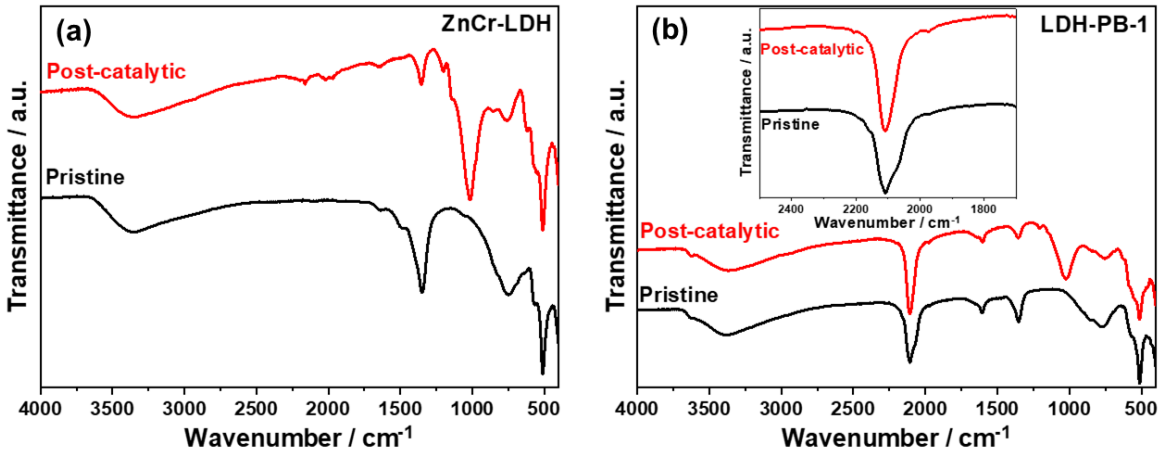

Figure 39. ATR-FTIR spectra of (a) ZnCr-LDH, and (b) LDH-PB-1 for pristine (black line) and post-catalytic (red line) samples. Inset: The cyanide stretch mode for bare and post-catalytic samples. The band at 1020 cm^{-1} in post-catalytic samples corresponds to the stretching modes of remaining phosphate anions of KPi buffer.

The FTIR spectrum of the LDH-PB-1 sample after the photocatalytic experiment shows an increase in the intensity of the band at 2160 cm^{-1} (Co^{III}–NC–Fe^{II} coordination mode)

while the shoulders disappear. These results reveal an electron transfer process between LDH and PBA, which is consistent with XPS investigations.

3.3 Summary

In summary, the strengths of LDHs and PB structures were combined to develop an entirely earth-abundant semiconductor-catalyst assembly for the visible-light-driven water oxidation process. We systematically changed experimental parameters including the mixing temperature and weight ratio of components and optimized the synthetic methodology to obtain a combination of enhanced activity and stability. The summary of photocatalytic performances of previously reported ZnCr-LDHs listed in Table 4 indicates that LDH-PB assembly exhibits a remarkable activity among LDH-based systems. ZnCr-LDH is an efficient visible light-absorbing semiconductor, while CoFe-PBA plays an active role in catalytic water oxidation. The photocatalytic assembly is easy-to-prepare and is composed of earth-abundant components. The well-placed energy level of the CoFe-PB structure between the water oxidation and the valence band of ZnCr-LDH makes it an ideal catalyst for efficient hole transfer from the semiconductor to the water oxidation process. This efficient electron transfer not only reveals a three-fold enhancement in the photocatalytic performance compared to bare LDH but also improves its stability under photocatalytic conditions. We also observed that the mole ratio of LDH and PB components could be tuned to enhance the activity and stability of LDH-PB assemblies.

Table 4. A comparison study between the LDH-PB-1 sample in this work and previously reported photocatalysts for visible-light water oxidation.

Photocatalyst	**Light Source**	**Incident Light λ (nm)**	**Scavenger**	**O_2 Evolved (mmol g^{-1} h^{-1})**	**Ref.**
ZnCr-LDH	200 W Xe lamp	> 400	0.01 M $AgNO_3$	1.06	[199]
ZnCr-LDH/Titanate	450 W Xe lamp	> 420	0.01 M $AgNO_3$	1.18	[109]
ZnCr-LDH/Graphene	450 W Xe lamp	> 420	0.01 M $AgNO_3$	1.2	[116]
ZnCr-LDH/POM	450 W Xe lamp	> 420	0.01 M $AgNO_3$	2.4	[117]
Tb doped ZnCr-LDH	150 W Xe lamp	> 420	0.01 M $AgNO_3$	1.02	[112]
ZnCr-LDH/Cu_2O	300 W Xe lamp	> 400	Pure water	0.022	[114]
ZnCr-LDH/$Co(OH)_2$	125 W Xe lamp	> 420	0.05 M $AgNO_3$	14	[113]
ZnCr-LDH/CoFe-PBA	300 W Xe lamp	> 420	5 mM $Na_2S_2O_8$	1.60	This Work

Chapter 4

Photocatalytic Water Oxidation with a CoFe Prussian Blue Analogue−Layered Niobate Hybrid Material

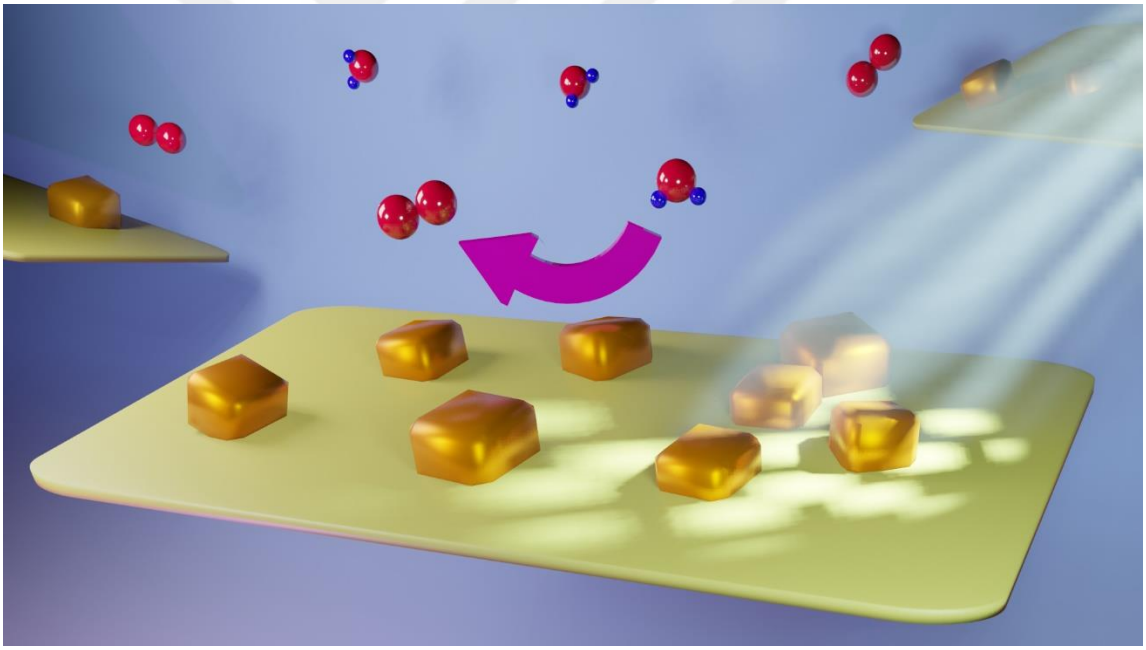

This chapter is based on the publication: **S. S. Akbari**, U. Unal, and F. Karadas, "Photocatalytic Water Oxidation with a CoFe Prussian Blue Analogue–Layered Niobate Hybrid Material," *ACS Appl. Energy Mater.*, vol. 4, no. 11, pp. 12383–12390, 2021 (Reproduced with permission from American Chemical Society, Ref. [200] Copyright © 2021, American Chemical Society).

This work was carried out in collaboration with the group of Assoc. Prof. Ugur Unal (Department of Chemistry, Koç University).

4.1 Experimental Procedure

4.1.1 Materials

Niobium(V) chloride ($NbCl_5$, Alfa Aesar, 99.999%), calcium carbonate ($CaCO_3$, Alfa Aesar, 99.9%), potassium carbonate (K_2CO_3, anhydrous, Alfa Aesar, 99%), anhydrous citric acid (CA, Sigma Aldrich, ACS Reagent 99.5%), ethylene glycol (EG, Sigma Aldrich, >99%), nitric acid (HNO_3, Sigma Aldrich, 70%), tetra(n-butyl)ammonium hydroxide (TBA, Aldrich, 40 wt % in H_2O), cobalt(II) nitrate hexahydrate ($Co(NO_3)_2 \cdot 6H_2O$, Alfa Aesar, 99.9%), potassium hexacyanoferrate(III) ($K_3[Fe(CN)_6]$, Sigma Aldrich, 99%), sodium persulfate ($Na_2S_2O_8$, Sigma Aldrich, >99%), sodium sulfate (Na_2SO_4, Acros Organics, 98%), methanol (MeOH). Potassium phosphate buffer solutions were prepared by 0.1 M KH_2PO_4, and 0.1 M K_2HPO_4 diluted in 500 mL deionized water with a pH close to 7. Deionized water (resistivity: 18 MΩ/cm) is used in all experiments.

4.1.2 Sample Preparation

***Synthesis of layered $KCa_2Nb_3O_{10}$*:** Dion-Jacobson phase $KCa_2Nb_3O_{10}$ layered structure was synthesized by a complex polymerization method [140]. $NbCl_5$ (3.06 g), $CaCO_3$ (0.77 g), K_2CO_3 (0.30 g), anhydrous citric acid (CA; 21.83 g), and ethylene glycol (EG, 25.40) were used as precursors materials. In a typical synthesis, $NbCl_5$ was dissolved in 113.43 mL of methanol. Then, appropriate amounts of $CaCO_3$ and K_2CO_3 were added to the solution in a ratio to sustain charge neutrality with continuous stirring. Anhydrous citric acid was used as a chelating agent so that [$NbCl_5$]/[CA] ratio was 0.1. Moreover, ethylene glycol was added to the mixture in a [CA]/[EG] ratio of 4. An excess of K_2CO_3 (10 mol %

of K) was added to the solution to compensate for volatilization in the calcination step. The reaction mixture was heated at ~100 °C for 6−8 h on a hot plate stirrer. The as-obtained transparent solution was heated to ~300−350 °C to promote polyesterification between EG and CA in a heating mantle. The mixture yielded a glassy resin first, and black powder was obtained at the end of the carbonization reaction. The black powder was calcined at 650 °C for 6 h in an Al_2O_3 crucible to remove the residual organic content. The obtained white precursor was then further calcined at 800−1200 °C for 2−5 h in an Al_2O_3 crucible.

***Preparation of the proton−exchanged powders*:** Proton exchange was carried out in an aqueous nitric acid (6 M) at room temperature for 3 days. The products were collected by vacuum filtration, washed extensively with double distilled H_2O, and dried at 80 °C overnight.

***Preparation of the nanosheets*:** Exfoliation of the as-prepared proton-exchanged materials was performed using aqueous tetra(n-butyl)ammonium hydroxide (TBA) at room temperature as reported by Maeda et al. [140]. The powder was shaken in an aqueous solution containing TBA for 1 week with the molar ratio $[TBA]/[H^+]=1$. The reaction was performed on a shaker for 7 days. Final nanosheet solutions were obtained by storing the supernatant after centrifugation of the solutions at 3000 rpm for 30 min.

***Preparation of Niobate/PB hybrid assembly*:** For the preparation of the hybrid structure, 0.18 mmol of $Co(NO_3)_2.6H_2O$ was dissolved in 10 mL of deionized water, added dropwise to a solution containing exfoliated $Ca_2Nb_3O_{10}^-$ layers at room temperature, and stirred for 1 h. The $Co/[Ca_2Nb_3O_{10}^-]$ precipitate was collected by centrifugation and washed with water. The obtained pinkish solid was dispersed in deionized water and sonicated for 20 min. Subsequently, an aqueous solution of $K_3[Fe(CN)_6]$ (0.12 mmol in 10 mL water)

was added dropwise to the above solution and stirred for 18 h. The final precipitate was separated by centrifugation, rinsed with deionized water, and dried at 75 °C.

4.1.3 Photocatalytic O_2 Evolution

The photocatalytic experiments were carried out in a 16 mL Pyrex reactor at room temperature. A 5 mg portion of the catalyst was suspended in 10 mL of deionized water containing 5 mM $Na_2S_2O_8$ as a sacrificial agent. The reaction solution was degassed by bubbling N_2 gas for 30 min before light irradiation. A Xe lamp (300 W; AM 1.5 global filter.) was used as a light source. The amount of generated O_2 was determined at 1 h intervals by injecting 100 µL of the reactor headspace gas into GC. Two rubber septa were used to seal the reactor, where the space between them was purged with N_2 gas to avoid a possible O_2 leak during the measurements.

4.2 Results and Discussion

4.2.1 Synthesis and Characterization of Materials

$KCa_2Nb_3O_{10}$ compound was synthesized and exfoliated according to the reported procedures in the literature [140], [201]. The exfoliated calcium niobate nanosheets were restacked by cobalt ions and subsequently reacted with a solution of $[Fe(CN)_6]^{3-}$ to afford a hybrid assembly (abbreviated from now on as Niobate/PB), which is composed of niobate nanosheets and uniform CoFe-PB cubic structures (Figure 40a). Figure 40b shows XRD patterns of the pristine $KCa_2Nb_3O_{10}$ and the Niobate/PB samples. The XRD pattern of $KCa_2Nb_3O_{10}$ exhibits no impurity phase and shows that the layered structure was successfully prepared. The combination of niobate sheets with PB results in a shift of the (020) peak of the layered niobate structure to 4.8°, which corresponds to an interlayer distance of around 18.2 Å. Other peaks at 2Θ = 23.09°, 32.88°, and 47.14° belong to the

(110), (112), and (040) lattice planes, respectively. The loss of other peaks belonging to the layered $KCa_2Nb_3O_{10}$ structure and the broad peak at 2Θ = 4.8° show that the exfoliation/restacking process and formation of PB arrange $Ca_2Nb_3O_{10}^-$ nanosheets in a stratified structure. The diffraction peaks on the diffraction pattern of the hybrid structure at 17.5°, 24.8°, 35.2°, and 39.5° correspond to (200), (220), (400), and (420) lattice planes of a cubic PB structure. The XRD pattern of Niobate/PB, thus, indicates that the PB structure was prepared successfully on the niobate nanosheets [85].

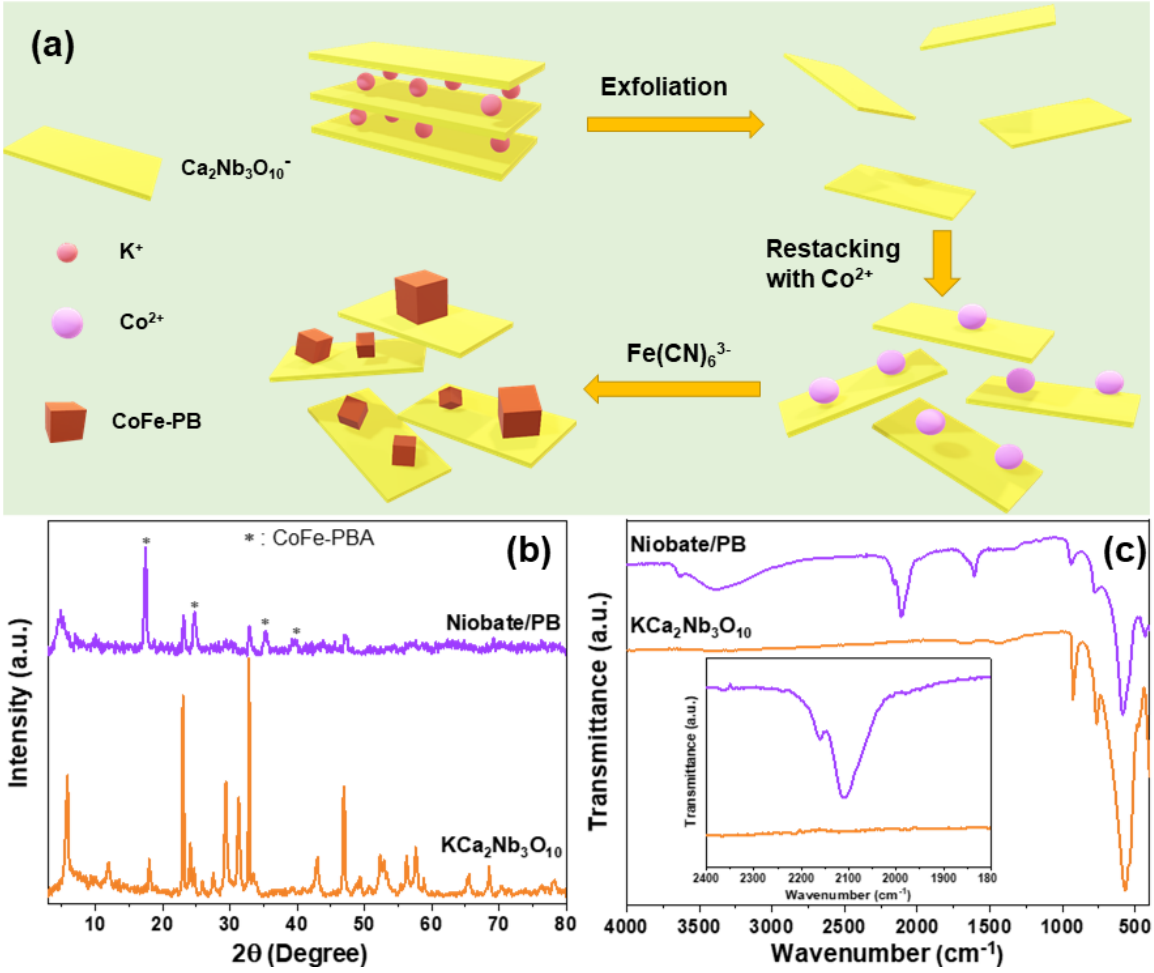

Figure 40. (a) Schematic representation for the in-situ synthesis of CoFe-PB on exfoliated $Ca_2Nb_3O_{10}^-$ nanosheets at room temperature. (b) XRD patterns of $KCa_2Nb_3O_{10}$ and Niobate/PB samples. (c) ATR-FTIR spectra of $KCa_2Nb_3O_{10}$ and Niobate/PB samples. Inset: the cyanide stretching mode.

FTIR spectrum of Niobate/PB, the strong band at 585 cm^{-1} can be assigned to the asymmetric stretching vibration of central Nb−O bonds in the NbO_6 octahedron of the perovskite layer. The asymmetric stretching vibration of the bridge Nb−O in the terminal NbO_6 group results in a peak at 778 cm^{-1}, whereas the peak at 939 cm^{-1} can be assigned to the stretching vibration of the terminal Nb−O [202], [203]. Once the niobate nanosheets are coupled to PB particles, the intensity of the band at 778 cm^{-1} decreases, which could be attributed to the interaction of terminal Nb−O bonds in the perovskite layer with PB structures. The broad band at 3386 cm^{-1} and the sharp one at 3641 cm^{-1} are attributed to the OH stretching of water molecules on the surface of PB particles. Another sharp band at 1606 cm^{-1} can be assigned to the bending mode of water molecules inside the PB structure [177]. The two bands at 2110 cm^{-1} and 2162 cm^{-1} are attributed to Co(III)–NC–Fe(II) and Co(II)–NC–Fe(III) coordination modes, respectively (Figure 40c) [176].

The structure and morphology of the samples were also studied by SEM and TEM images. SEM images reveal the presence of a platelike layered structure of calcium niobate nanosheets in $KCa_2Nb_3O_{10}$ (Figure 41a-c). Niobate/PB also displays lamellar morphology, while the size of its layers is relatively smaller than that of $KCa_2Nb_3O_{10}$, suggesting a decrease in size of the layered niobate during the exfoliation−restacking route (Figure 41d-f). While exfoliation drastically reduces the thickness of layered perovskites, restacking can re-increase their thickness to some degree.

The atomic ratio of Co:Fe:Nb for the hybrid sample is found to be around 5:3.5:4.2 by an EDS analysis (Figure 41g,h). EDS elemental mapping of the Niobate/PB sample reveals that the PB structure is well-dispersed on calcium niobate layers to form a uniform hybrid assembly (Figure 42).

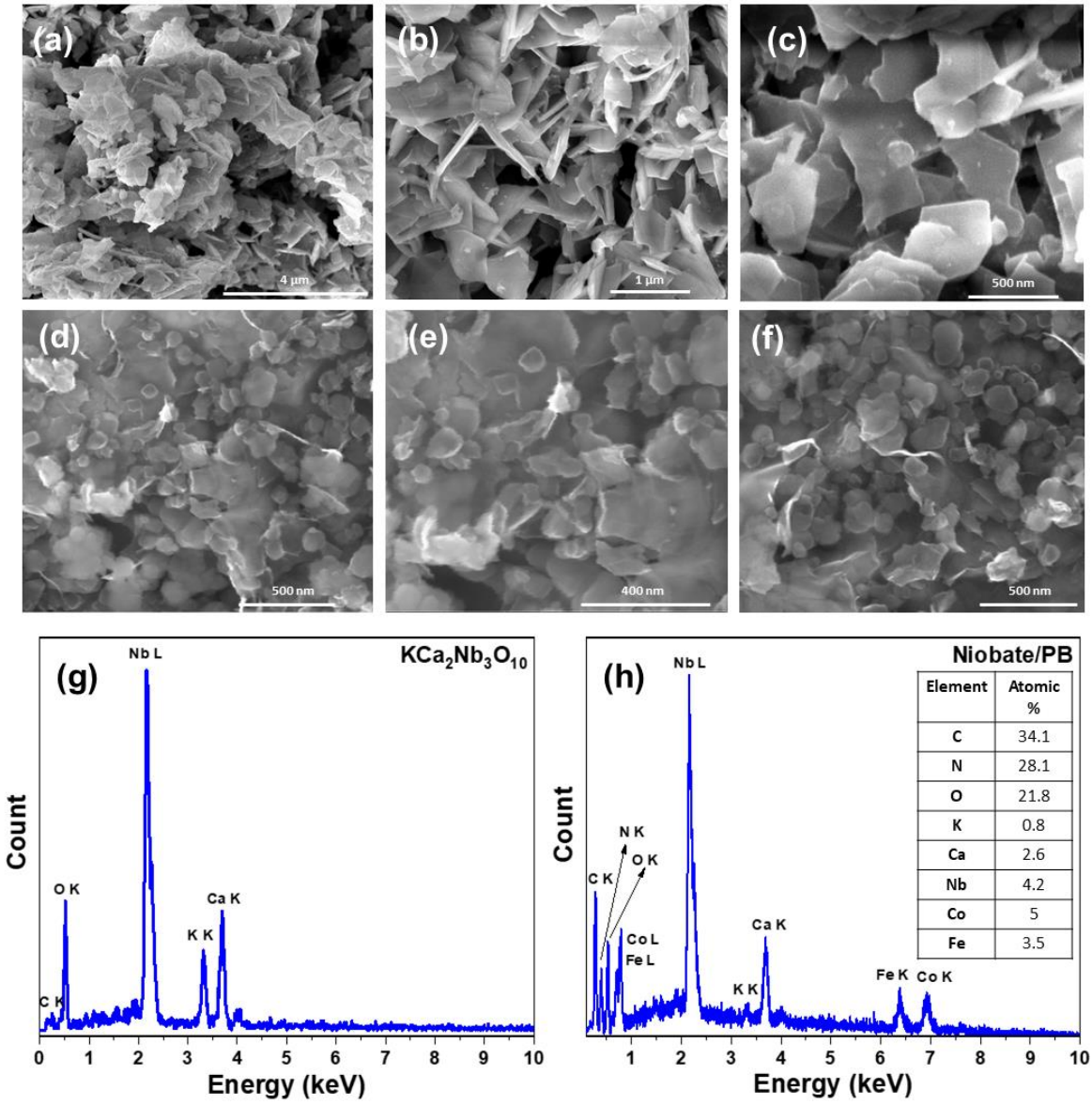

Figure 41. SEM images of (a-c) $KCa_2Nb_3O_{10}$, and (d-f) Niobate/PB samples. SEM-EDS analysis of (g) $KCa_2Nb_3O_{10}$, and (h) Niobate/PB samples. Inset: The atomic ratio of all elements for the Niobate/PB sample.

TEM analysis of the Niobate/PB sample indicates the formation of a cubic Prussian blue structure with a size of 20−50 nm on the niobate layers (Figure 43). Moreover, STEM images and corresponding EDS elemental analysis confirm the presence of Co and Fe elements in the structure of produced cubes (Figure 44).

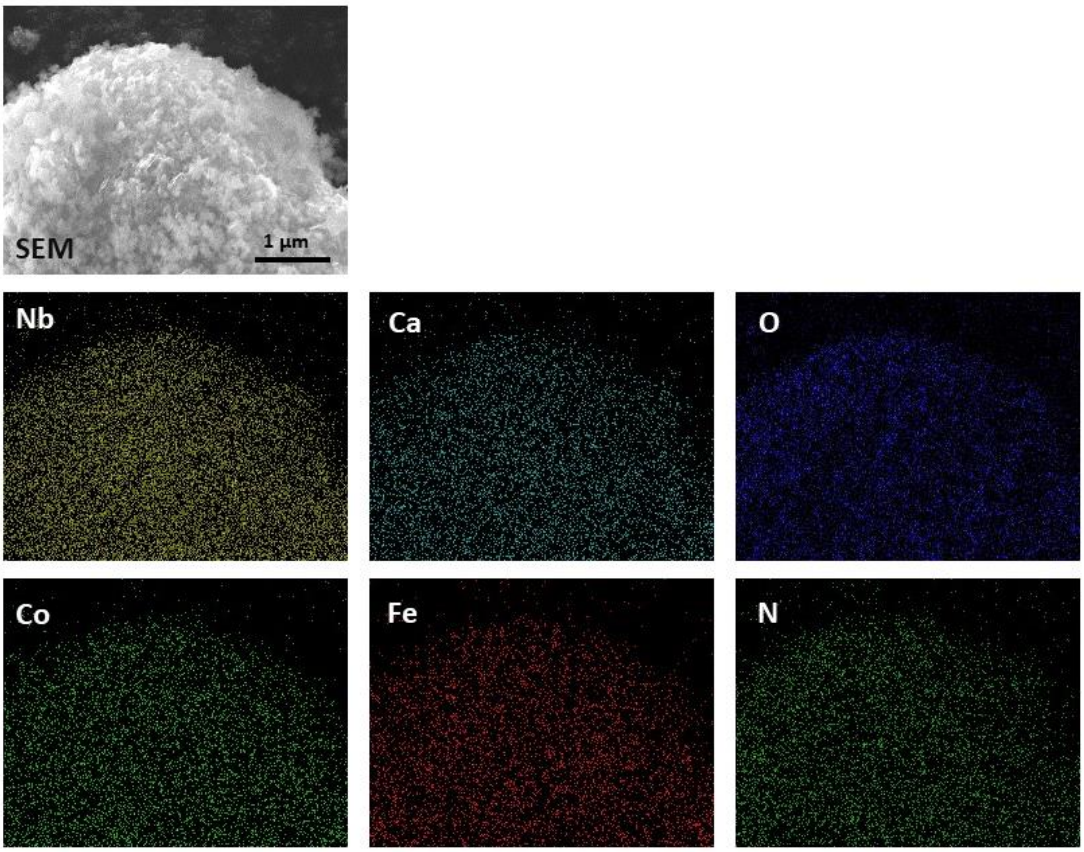

Figure 42. SEM image and related EDS elemental mappings of Nb, Ca, O, Co, Fe, and N for the Niobate/PB sample.

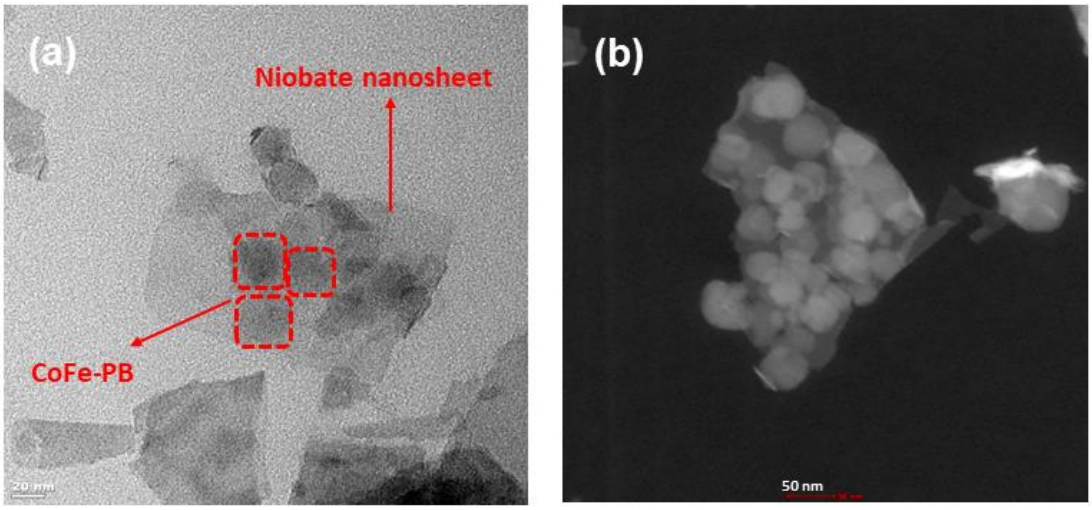

Figure 43. (a) The TEM image of the Niobate/PB sample. (b) HAADF image of the Niobate/PB sample.

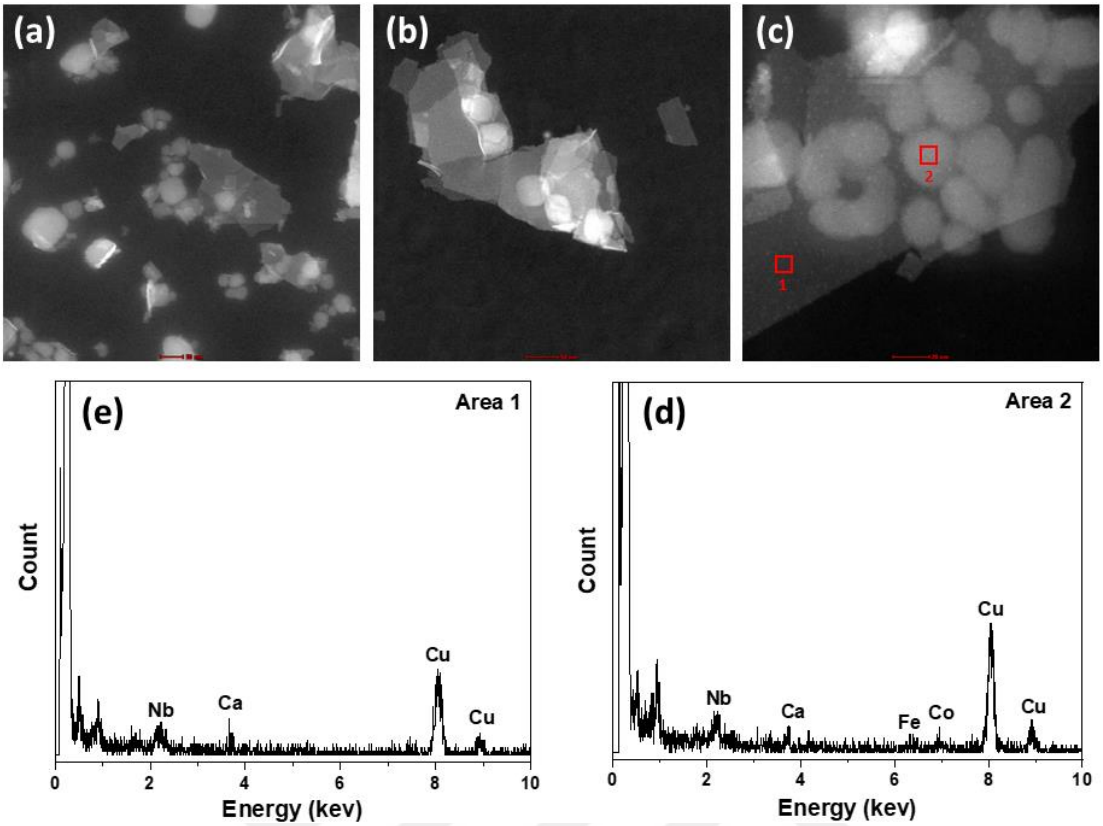

Figure 44. (a-c) HAADF-STEM images of the Niobate/PB sample. (e-d) EDS elemental analysis of selected areas.

4.2.2 Photocatalytic Activity and Band Structure

The optical properties of $KCa_2Nb_3O_{10}$ and Niobate/PB samples were studied with UV−Vis diffuse reflectance spectroscopy (Figure 45). The characteristic absorption band of $KCa_2Nb_3O_{10}$ extends up to 350 nm, which is associated with the electronic transition from the VB consisting of the O 2p orbitals to the CB consisting of empty Nb 4d orbitals [139]. On the other hand, the Niobate/PB sample exhibits a broad background absorption in the 350−800 nm region due to the electronic interaction between the calcium niobate nanosheets and PB particles. This can be confirmed by the difference in the color of the white bare niobate nanosheets and the dark purple hybrid sample. Two broad absorption regions in the 350–800 nm range illustrate the characteristic charge transfer in CoFe-PB structures and prove that the hybrid system is active in the visible region [194]. However,

the niobate layers' inherent band structure remains unchanged in the hybrid structure since the crystal and chemical structures of the niobate layers are not modified.

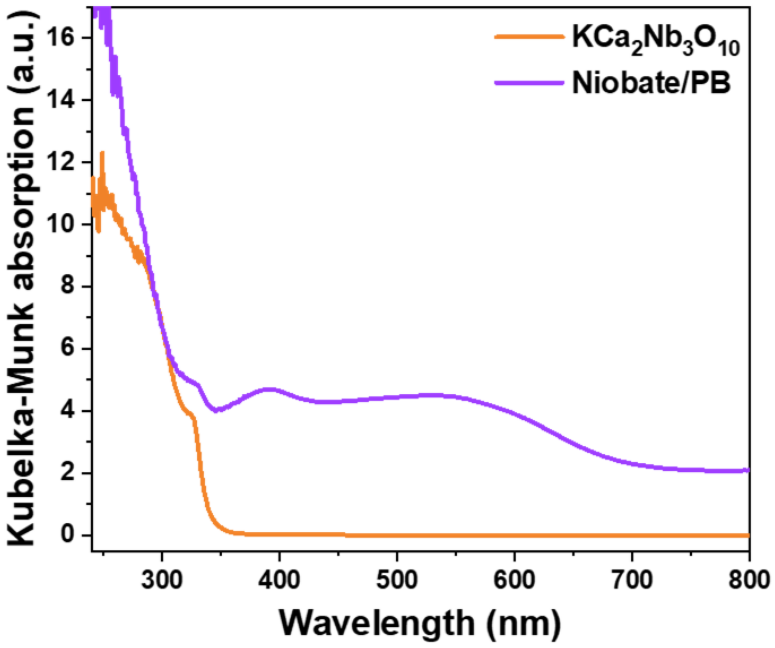

Figure 45. Diffuse reflectance UV−Vis spectra (plotted as the Kubelka−Munk function of the reflectance, R) of $KCa_2Nb_3O_{10}$ and Niobate/PB samples.

The photocatalytic oxygen evolution performance of $KCa_2Nb_3O_{10}$ and PB-modified calcium niobate samples were evaluated under UV−Vis irradiation in the presence of 5 mM $Na_2S_2O_8$ as a sacrificial agent (Figure 46). A set of four cycles, each with a 3 h duration, was performed. The Niobate/PB hybrid sample exhibits an enhanced water oxidation photocatalytic activity (89.5 µmol g^{-1} h^{-1}) in the 1st h of each cycle, which is ca. 6.5 times higher than that of $KCa_2Nb_3O_{10}$ (13.4 µmol g^{-1} h^{-1}). During all four cycles, the activity decreases gradually after the 1st h, which could be attributed to the consumption of the electron scavenger. Before each cycle, $S_2O_8^{2-}$ was added to the suspension. The similarity of all cycles suggests the hybrid assembly maintains its activity and stability during a 12 h experiment. This enhancement could be attributed to a more effective charge separation process in comparison to the bare niobate sample in addition to the large surface area

provided by the exfoliation−restacking route, which maintains its activity even during the 4th cycle.

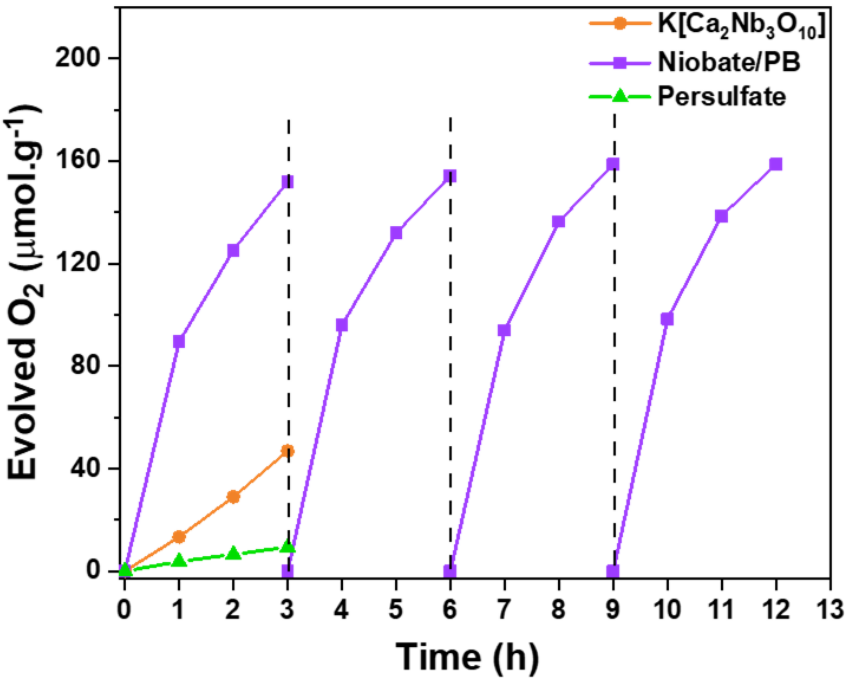

Figure 46. Photocatalytic oxygen evolution activities of persulfate, $KCa_2Nb_3O_{10}$, and Niobate/PB samples (μmol of generated O_2/g of catalyst) in water containing 15 mg of the catalyst and 5 mM $Na_2S_2O_8$ as the sacrificial agent under UV−Vis irradiation (300 W Xe lamp). After each cycle, 5 mM $Na_2S_2O_8$ was added to the reaction solution.

The photocatalytic activity of restacked $KCa_2Nb_3O_{10}$ sheets has previously been reported to be 14 μmol g^{-1} h^{-1} in the presence of IO_3^- ions. RuO_2−loading was realized as an effective method for promoting water oxidation activity (126 μmol g^{-1} h^{-1}) [139]. Pt intercalation could also improve the photocatalytic activity of calcium niobate layers (75 μmol g^{-1} h^{-1}) [134]. Hybrid assemblies incorporating earth-abundant catalysts, however, exhibit much lower activities. For example, the photocatalytic activity of niobate nanosheets was reduced to 10 μmol g^{-1} h^{-1} when they were coupled with CoO_x [138]. Photocatalytic experiments with a 420 nm cutoff filter were also performed to determine the activity of the bare niobate and the Niobate/PB sample under visible light illumination (Figure 47). While bare niobate nanosheets are not active under visible light irradiation, an

activity of 48.6 μmol g^{-1} h^{-1}, although around two times lower compared to the "no filter" case, is observed with the Niobate/PB sample. The lower activity under visible light irradiation suggests that the hybrid assembly is active in both the UV and visible regions. CoFe-PB, thus, serves not only as a water oxidation catalyst but also as a visible-light absorber in the hybrid sample.

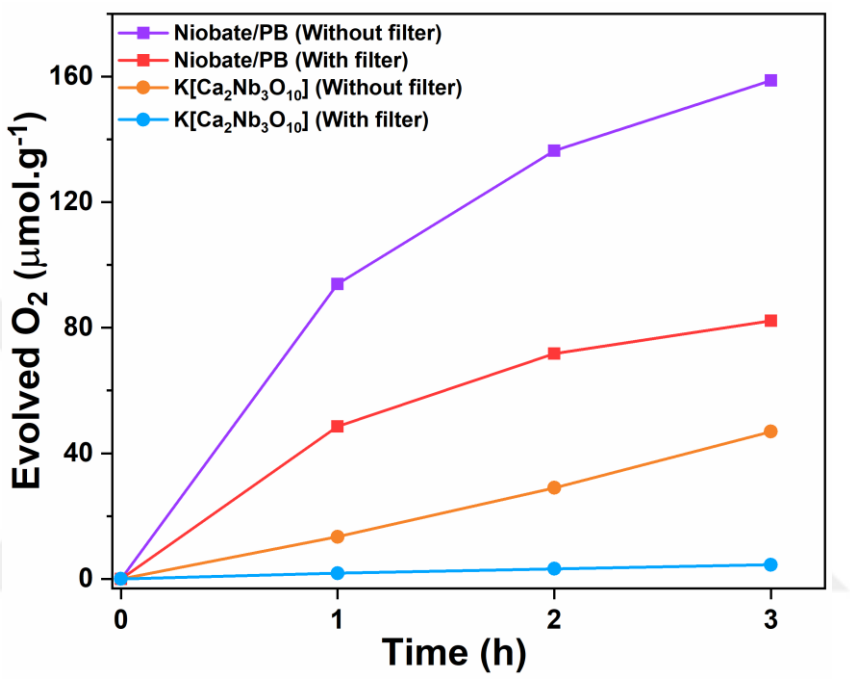

Figure 47. Photocatalytic oxygen evolution activity of $KCa_2Nb_3O_{10}$ and Niobate/PB samples in water containing 5 mM $Na_2S_2O_8$ as the sacrificial agent under light irradiation, without filter (purple and orange lines) and with a 420 nm long−pass filter (red and blue lines).

PEC experiments were carried out to understand the charge transfer process and the electron−hole separation efficiency of bare niobate and hybrid samples (Figure 48a). The enhanced photocurrent response of Niobate/PB compared to $KCa_2Nb_3O_{10}$ suggests a much higher migration and separation rate of photogenerated electrons and holes under UV−Vis light illumination. The Mott−Schottky plots of $KCa_2Nb_3O_{10}$, CoFe-PB, and Niobate/PB electrodes were also obtained, as shown in Figure 48. The positive slope obtained for the $KCa_2Nb_3O_{10}$ electrode reveals that the niobate nanosheets are n-type semiconductors. The

flat band potential of niobate nanosheets is estimated as −0.6 V (vs. NHE), which is consistent with a previous report (Figure 48b) [173]. It is assumed that the conduction band edge potential of the n−type metal oxide semiconductor is 0.1−0.4 eV more negative relative to the flat band potential [204]. According to the literature, this value is assumed to be 0.4 eV for niobate semiconductors. Therefore, the conduction band edge for niobate nanosheets was obtained as −1 V (vs. NHE) [173], [205]. The p-type semiconducting character of the PB structure is evidenced by the Mott−Schottky analysis and a previous study (Figure 48c) [206].

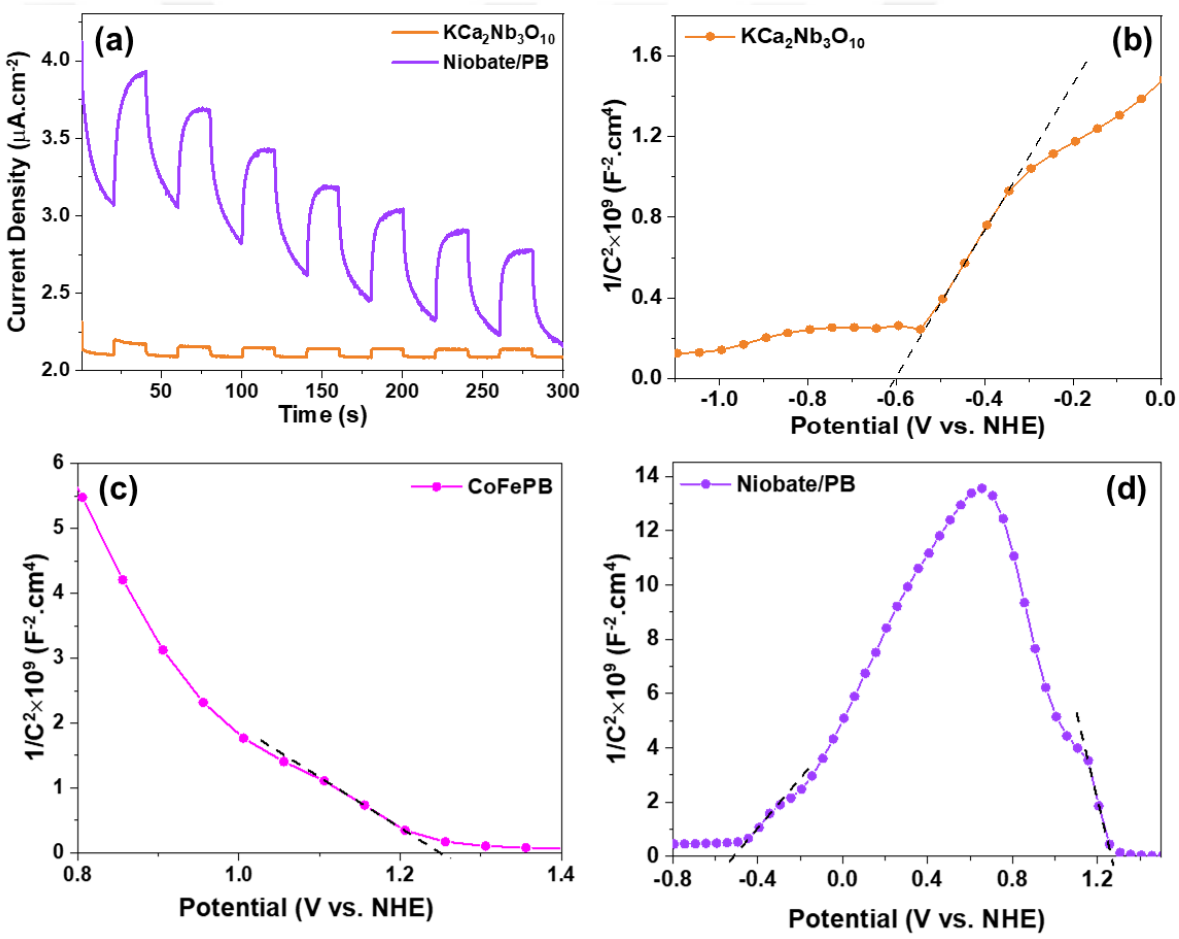

Figure 48. (a) Transient photocurrent responses of $KCa_2Nb_3O_{10}$ and Niobate/PB samples in 0.1 M PBS (pH = 7) containing 0.5 M Na_2SO_4 under UV−Vis irradiation (300 W Xe lamp). Mott-Schottky plots of (b) $KCa_2Nb_3O_{10}$, (c) CoFe-PB, and (d) Niobate/PB electrodes.

As seen in Figure 48d, the flat band potential for the Niobate/PB shifted to more positive potentials, suggesting a decrease in the bending of the niobate band edges. The reverse V−shaped Mott−Schottky plot for the Niobate/PB system is typical evidence for a p−n junction formation, which clearly explains the increase in the photocurrent and photocatalytic water oxidation activity for the Niobate/PB sample [207]–[209]. The formation of the p−n junction results in a strong electric field within the space charge region and decreases the charge transfer resistance at the interface, which enhances the charge carrier dynamics at the electrode/electrolyte interface. The alignment of bands makes the hole transfer through the p−type PB beneficial for the water oxidation reaction.

Layered niobate has a proper band structure for both hydrogen and oxygen evolution reactions similar to that of various wide band gap metal oxide semiconductors [40], [210]. The bulk structure of the 2D layered niobate, however, is not an efficient photocatalyst when compared to its individual nanosheets obtained after exfoliation. In addition, the long diffusion length for electron−hole pairs in bulk structures increases the probability of electron−hole recombination, which, in turn, decreases the photocatalytic activity of the semiconductor [40], [211]. Exfoliation, on the other hand, separates the metal oxide building blocks of the layered structure into its individual nanosheets, which produce a larger surface area. Exfoliated nanosheets of the layered structure also behave as a single crystalline structure with much shorter diffusion lengths for electron−hole pairs [124], [211]. Another advantage of exfoliation is that the band gap of a nanosheet is greater than that of the bulk structure due to the confinement effect. The increase in the water oxidation photocatalytic activity after the exfoliation/restacking route for the Niobate/PB system can also be attributed to the higher surface area, short diffusion length for electron/hole pairs, and greater availability of reaction sites on both PB structure and individual nanosheets. In addition, the strong electric field established at the p−n junction formed by niobate

nanosheets and PB particles enhances the photocatalytic water oxidation activity. The band gap of niobate nanosheets was estimated to be 3.54 eV by fitting the absorption data with a Tauc plot (Figure 49) [205], [212].

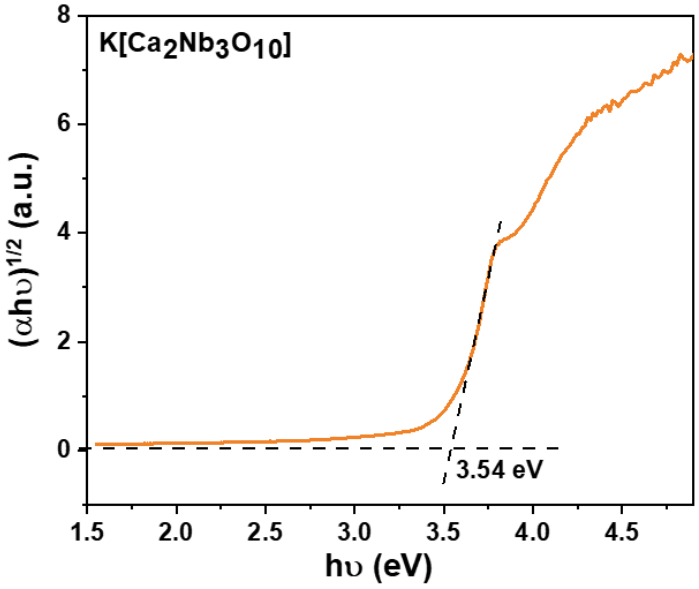

Figure 49. Tauc's plot of $KCa_2Nb_3O_{10}$ for the estimation of the band gap.

A cyclic voltammetry measurement reveals the HOMO level of the PB structure to be around 1.41 V vs. NHE (Figure 50).

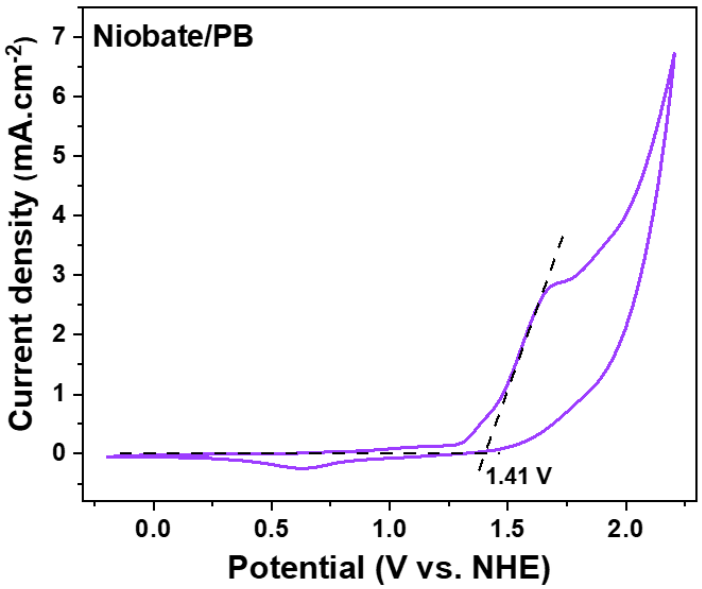

Figure 50. Cyclic voltammetry (CV) curves for the Niobate/PB electrode in 0.1 PBS (pH=7) containing 0.5 M Na_2SO_4 at the scan rate of 50 mV/s.

Since the VB of the niobate nanosheets is at a more positive potential in comparison to that of PB, the hybrid assembly exhibits a proper band energy alignment for efficient hole transfer from the niobate nanosheets to the PB structure during the water oxidation process (Figure 51).

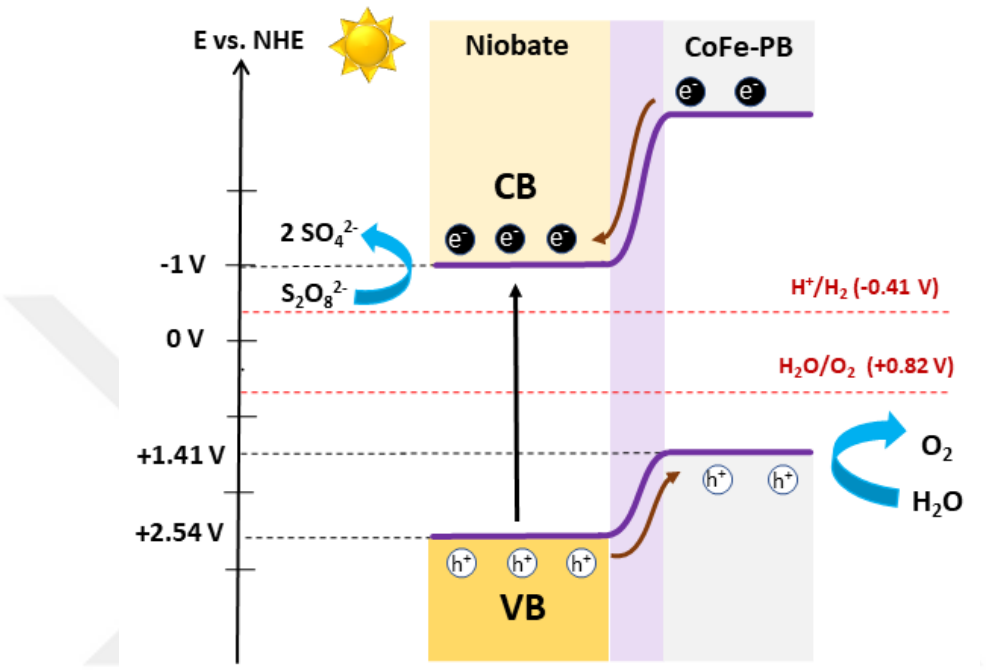

Figure 51. Schematic representation of the Niobate/PB p−n junction and charge-transfer mechanism under light irradiation.

4.2.3 Catalyst Stability Tests

An XPS analysis was performed to study the chemical composition of the Niobate/PB sample. The Nb 3d spectrum for the pristine sample exhibits two peaks at binding energies of 207.4 and 210.1 eV, corresponding to Nb $3d_{5/2}$ and $3d_{3/2}$, respectively (Figure 52a). The Ca 2p spectrum is deconvoluted to two strong peaks at 347.3 and 350.8 eV, which are assigned to Ca $2p_{3/2}$ and Ca $2p_{1/2}$ binding energies, respectively (Figure 52b). The O 1s region displays a strong peak at a binding energy of 530.4 eV, corresponding to the lattice oxygen. At higher binding energies, two additional peaks at 531.8 and 532.9 eV are

observed, which can be attributed to the surface-adsorbed hydroxyl and carbonate groups (Figure 52c) [187], [213].

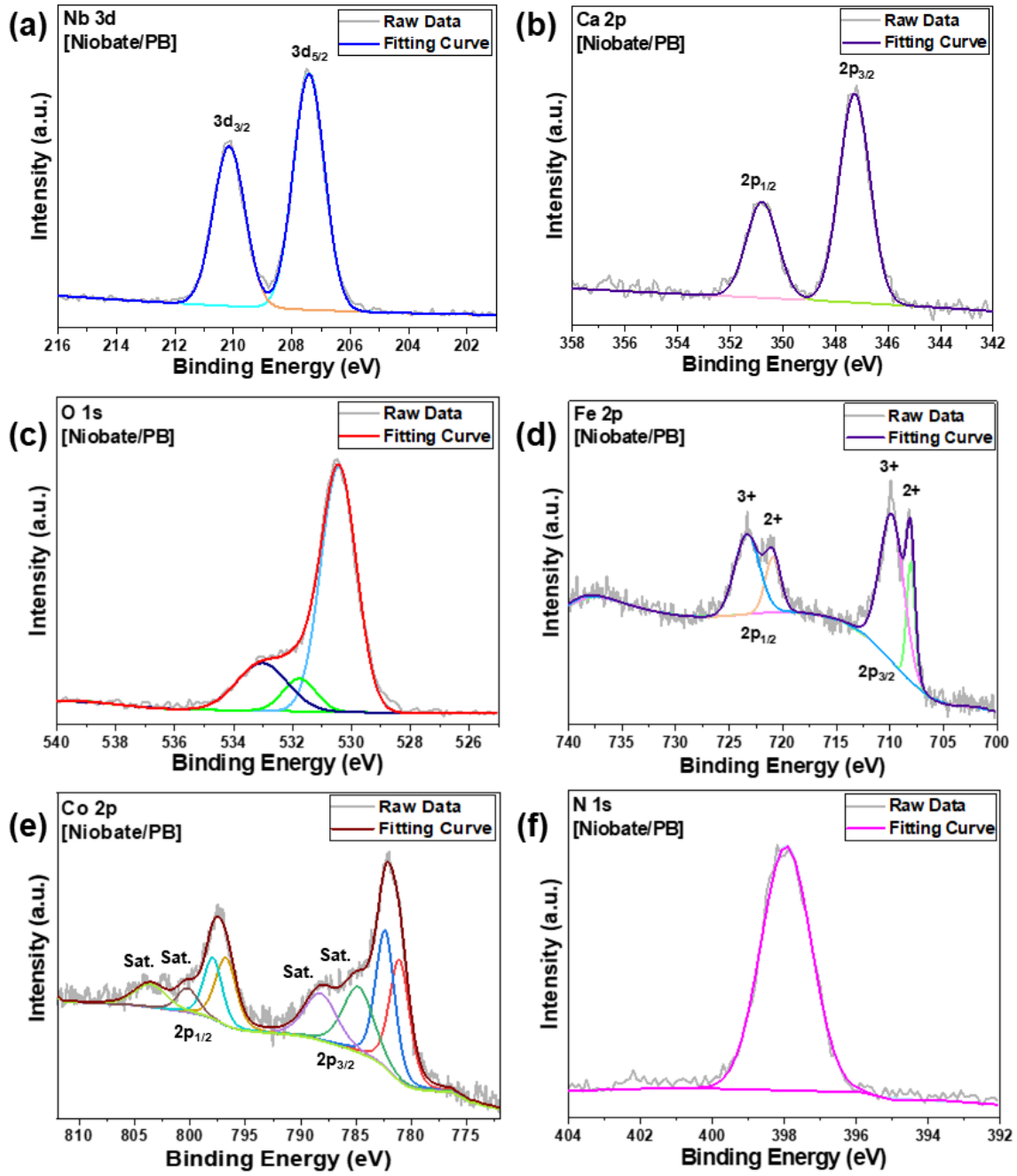

Figure 52. XPS spectra of the Niobate/PB sample (a) Nb 3d, (b) Ca 2p, (c) O 1s, (d) Fe 2p, (e) Co 2p, and (f) N 1s.

The Fe 2p spectrum reveals the presence of both +2 and +3 oxidation states in the hybrid sample. The peaks at 708.2 and 721.2 eV are assigned to Fe^{2+} $2p_{3/2}$ and Fe^{2+} $2p_{1/2}$,

respectively. Another doublet with slightly higher binding energies can be ascribed to $2p_{3/2}$ (709.9 eV) and $2p_{1/2}$ (723.4 eV) signals of the Fe^{3+} cation (Figure 52d) [179]. The Co $2p_{3/2}$ and Co $2p_{1/2}$ signals are deconvoluted into two main components in addition to shakeup satellite peaks at higher binding energies. The appearance of these satellites confirms the presence of Co^{2+} cations in the PB structure [180]–[182]. In general, the binding energy differences between $2p_{1/2}$ and $2p_{3/2}$ peaks ($\Delta E = 2p_{1/2}-2p_{3/2}$) are 15 and 16 eV for diamagnetic Co^{III} and paramagnetic Co^{II} complexes, respectively [183]–[185]. The presence of Co^{III} in the Niobate/PB sample is supported by ΔE = 15.4 eV, which is intermediate between the values of Co^{II} and Co^{III} complexes (Figure 52e) [186]. The copresence of +2 and +3 oxidation states for cobalt cations is also consistent with the FTIR results of the Niobate/PB sample, in which both Co(III)–NC–Fe(II) and Co(II)–NC–Fe(III) coordination modes were observed.

A comparison of XPS profiles of the Niobate/PB sample before and after the photocatalytic reaction reveals that the Nb 3d, Ca, 2p, and N 1s peaks remain unchanged during the photocatalytic experiment (Figure 53). As shown in Figure 53c, the peaks at 531.8 and 532.9 eV in the post-catalytic sample are more intense, indicating the adsorption of more hydroxyl and sulfate groups (from the decomposition of persulfate as the sacrificial agent) on the surface of Niobate/PB during the photocatalytic experiment [213], [214]. The amount of Fe^{2+} cations in the PB structure increases during the photocatalytic reaction (Figure 53d). The reduced intensities of Co $2p_{3/2}$ and $2p_{1/2}$ satellites and the lower value of spin−orbit splitting (ΔE = 15.2 eV) in the post-catalytic sample compared to the pristine one support the thesis that the Co^{2+} ions are partially oxidized to higher oxidation states during the photocatalytic process (Figure 53e) [180], [185].

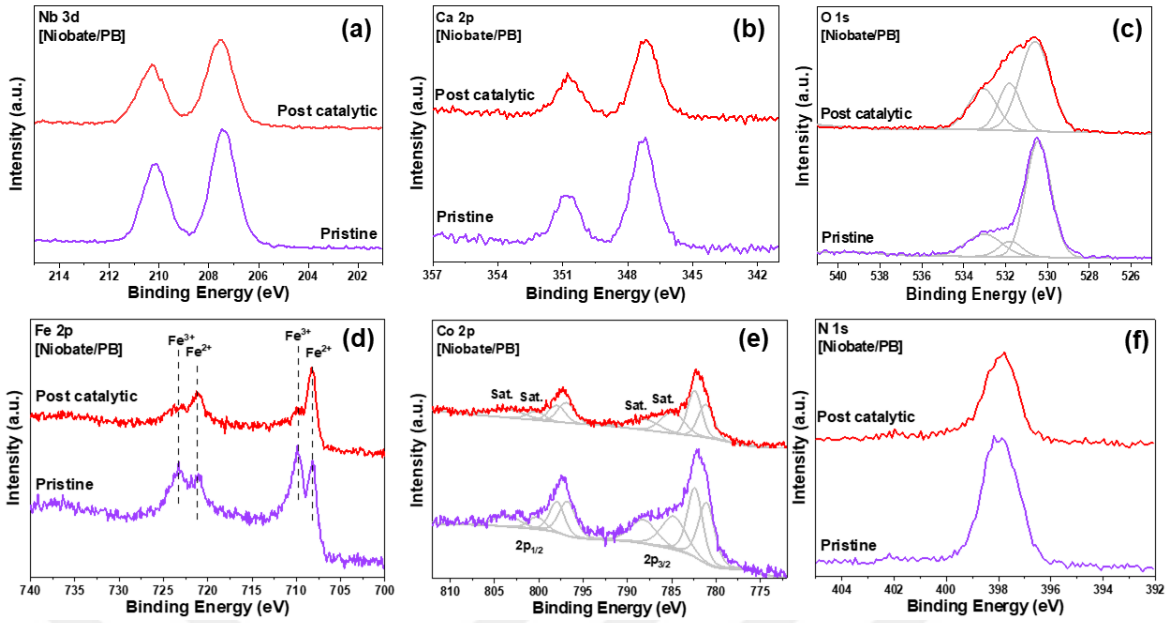

Figure 53. XPS spectra of (a) Nb 3d, (b) Ca 2p, (c) O 1s, (d) Fe 2p, (e) Co 2p, and (f) N 1s for pristine (purple line) and post-catalytic (red line) Niobate/PB samples.

These results are also in agreement with post-catalytic FTIR of the Niobate/PB sample, where the intensity of the band at 2160 cm^{-1} (Co(II)–NC–Fe(III) coordination mode) decreases compared to the one at 2110 cm^{-1} (Co(III)–NC–Fe(II) coordination mode; Figure 54).

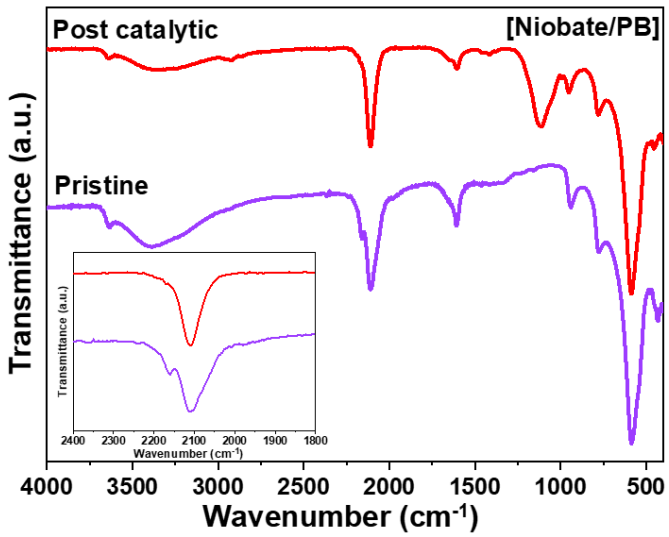

Figure 54. ATR-FTIR spectra of the Niobate/PB sample for pristine (purple line) and post-catalytic (red line) samples. Inset: the cyanide stretch mode for pristine (purple line) and post-catalytic (red line) samples.

The stability of the hybrid assembly is also confirmed by an SEM analysis of the post-catalytic sample (Figure 55). The layered structure of niobate nanosheets was preserved throughout the photocatalytic experiment.

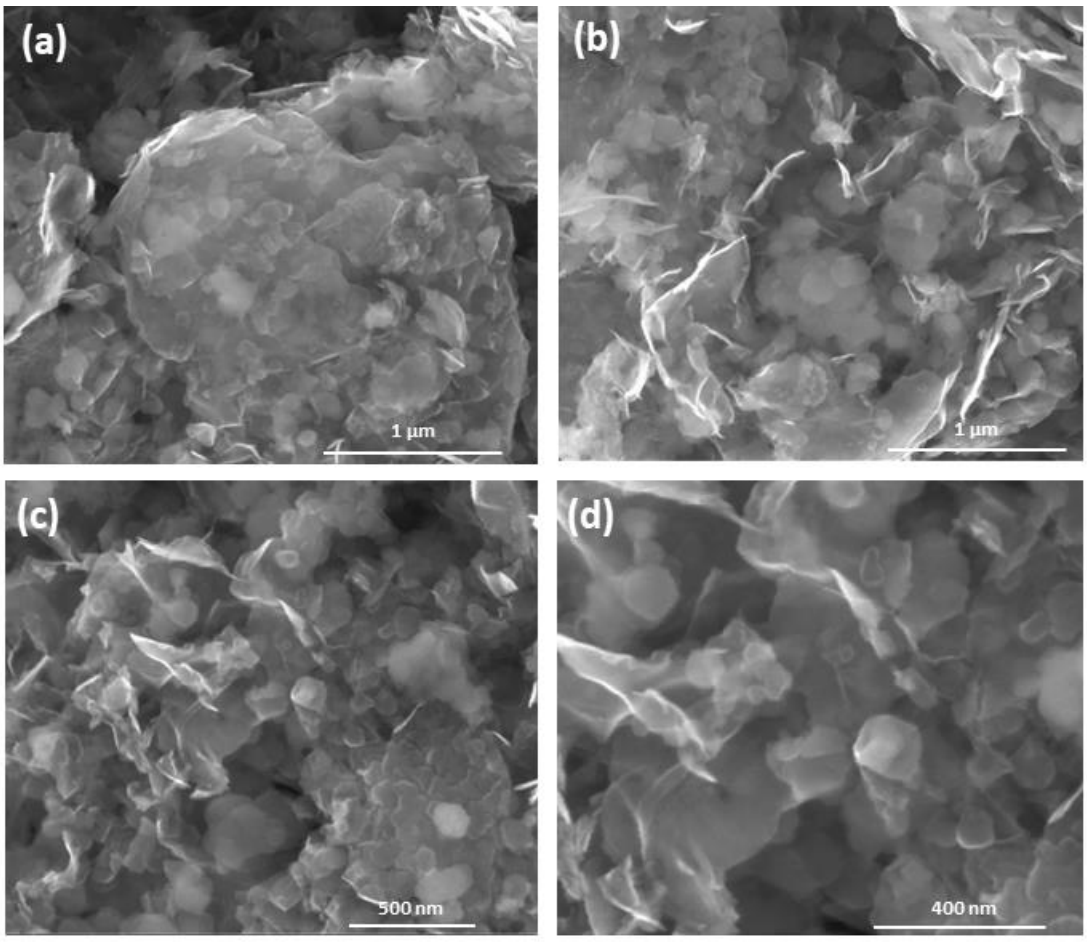

Figure 55. (a-d) SEM images of the post-catalytic Niobate/PB sample.

4.3 Summary

A CoFe-PBA was prepared in situ on niobate nanosheets to afford a semiconductor−catalyst hybrid assembly. The assembly is composed of niobate nanosheets and PB nanostructures with a particle size of around 50 nm. Photocatalytic water oxidation studies were performed on both bare niobate nanosheets and the hybrid assembly in the presence of an electron scavenger, $S_2O_8^{2-}$, to reveal that the hybrid assembly exhibits an enhanced activity throughout a 12 h photocatalytic experiment. Characterization studies on

the post-catalytic sample suggest that not only that the hybrid assembly retains its structural integrity, but also an electron transfer occurs between the niobate and PB components.

In conclusion, the hybrid assembly represents one of the first efficient p−n junction type niobate hybrid assemblies with an earth-abundant cocatalyst since it exhibits a catalytic activity of around 6.5 times higher than that of a bare niobate sample. The p−n junction feature allows the hybrid assembly to be active in the visible and UV regions. Easy structural tuning of both the niobate nanosheets and Prussian blue particles with metal doping allows several facile strategies to explore the niobate/PB interaction further, which are currently under investigation.

Table 5. A comparison study between the Niobate/PB sample in this work and previously reported photocatalysts for water oxidation.

Photocatalyst	**Cocatalyst**	**Incident Light λ (nm)**	**Scavenger**	**O_2 Evolved (μmol g^{-1} h^{-1})**	**Ref.**
$KCa_2Nb_3O_{10}$	-	UV−Vis	$AgNO_3$	8	[215]
$KCa_2Nb_3O_{10}$	RuO_x	UV−Vis	-	156.7	[216]
$KCa_2Nb_3O_{10}$	-	UV−Vis	$NaIO_3$	14	[133]
$KCa_2Nb_3O_{10}$	RuO_2	UV−Vis	$NaIO_3$	126	
$KCa_2Nb_3O_{10}$	Pt	UV−Vis	NaI	75	[134]
$KCa_2Nb_3O_{10}$	-	UV−Vis	$NaIO_3$	16	[138]
$KCa_2Nb_3O_{10}$	MnO_x	UV−Vis	$NaIO_3$	4	
$KCa_2Nb_3O_{10}$	CoO_x	UV−Vis	$NaIO_3$	10	
$KCa_2Nb_3O_{10}$	RhO_x	UV−Vis	$NaIO_3$	38	
$KCa_2Nb_3O_{10}$	IrO_x	UV−Vis	$NaIO_3$	110	
$KCa_2Nb_3O_{10}$	RuO_x	UV−Vis	$NaIO_3$	546	
$KCa_2Nb_3O_{10}$	Pt	UV−Vis	NaI	74.8	[135]
$KCa_2Nb_3O_{10}$	Pt	UV−Vis	KI	24	
$KCa_2Nb_3O_{10}$	Pt	UV−Vis	K_2SO_4	4.4	
$KCa_2Nb_3O_{10}$	Pt	UV−Vis	Na_2SO_4	40	
$KCa_2Nb_3O_{10}$	-	UV−Vis	$Na_2S_2O_8$	13.4	This
$KCa_2Nb_3O_{10}$	CoFe-PB	UV−Vis	$Na_2S_2O_8$	89.5	work

Chapter 5

Selective Photocatalytic CO_2 Reduction by Cobalt Dicyanamide

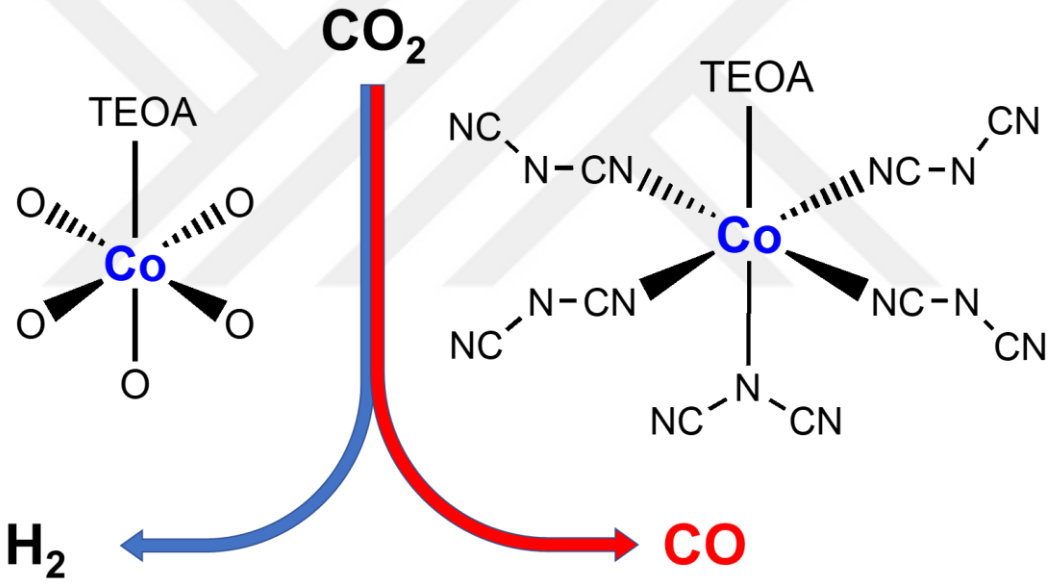

This chapter is based on the publication: **S. S. Akbari** and F. Karadas, "Selective photocatalytic CO_2 reduction by cobalt dicyanamide," *Dalt. Trans.*, 2022. vol. 51, no. 33, pp. 12569–12575, 2022. (Reproduced with permission from Royal Society of Chemistry Ref. [217] Copyright © 2022, Royal Society of Chemistry).

5.1 Experimental Procedure

5.1.1 Materials

Sodium dicyanamide ($NaN(CN)_2$, Acros Organics, 97%), cobalt(II) nitrate hexahydrate ($Co(NO_3)_2 \cdot 6H_2O$, Alfa Aesar, 99.9%), tris(2,2′−bipyridyl)ruthenium(II) dichloride hexahydrate ($[Ru(bpy)_3]Cl_2 \cdot 6H_2O$, Sigma Aldrich, 99%), potassium hexacyanoferrate(II) ($K_3[Fe(CN)_6]$, Sigma Aldrich, 99%), acetonitrile (MeCN, Sigma Aldrich, >99.9%), triethanolamine (TEOA, Acros Organics, 97%). Deionized water (resistivity: 18 MΩ/cm) is used in all experiments.

5.1.2 Sample Preparation

***Synthesis of Co-dca*:** Typically, an aqueous solution (4 mL) of $NaN(CN)_2$ (9 mmol) was added dropwise to a solution containing $Co(NO_3)_2.6H_2O$ (4 mL, 4.5 mmol) at room temperature. After 4 h stirring, the resulting light-pink precipitate was collected by centrifugation, rinsed thoroughly with water, and dried at 75 °C.

***Synthesis of CoFe-PB*:** For the synthesis of CoFe-PB, $K_3[Fe(CN)_6]$ (2 mmol) was dissolved in deionized water (20 mL), then an aqueous solution of $Co(NO_3)_2.6H_2O$ (3 mmol in 20 mL water) was added to the above solution at room temperature. The obtained slurry was stirred for 1 h and collected by centrifugation after rinsing with water. The obtained solid was dried at 75°C

5.1.3 Photocatalytic CO_2 Reduction Experiment

The photocatalytic experiments were carried out in a 16.5 mL Pyrex reactor at room temperature. Typically, 10 mg catalyst, 3.74 mg $[Ru(bpy)_3]Cl_2 \cdot 6H_2O$ (0.5 mM), 8 mL MeCN, and 2 mL TEOA as the sacrificial agent were added to the reactor. The reaction

solution was purged with CO_2 gas for 30 min before light irradiation. A Xe lamp (300 W; AM 1.5 global filter) equipped with a UV filter ($\lambda > 420$ nm) was used as a light source. The amount of generated gas was determined by injecting 100 µL of the reactor headspace gas into a GC.

5.2 Results and Discussion

5.2.1 Synthesis and Characterization of Co-dca

Co-dca was prepared by a straightforward precipitation method [149]. Each cobalt site is coordinated to six $[N(CN)_2]^-$ ligands via the four nitrile nitrogens and two central amido nitrogens. The octahedral cobalt sites are slightly elongated, in which the two axial amido nitrogens are located slightly farther from the metal center than the four equatorial nitrile nitrogens [151]. Cobalt sites on the surface, thus, exhibit coordination environments similar to those in CoFe-PBAs and cobalt phthalocyanines since they are surrounded by a combination of water molecules and nitrogen atoms of the dicyanamide groups [84].

The structure of Co-dca is elucidated with FTIR spectroscopy and XRD. The FTIR spectrum of Co-dca reveals absorption bands in the 2030–2420 cm^{-1} range, which correspond to the asymmetric and symmetric stretches of $\nu(C{\equiv}N)$. Two bands are also observed at 963 cm^{-1} and 1314 cm^{-1}, which can be assigned to $\nu_s(N{-}C)$ and $\nu_{as}(N{-}C)$, respectively (Figure 56 and Table 6) [152], [218], [219].

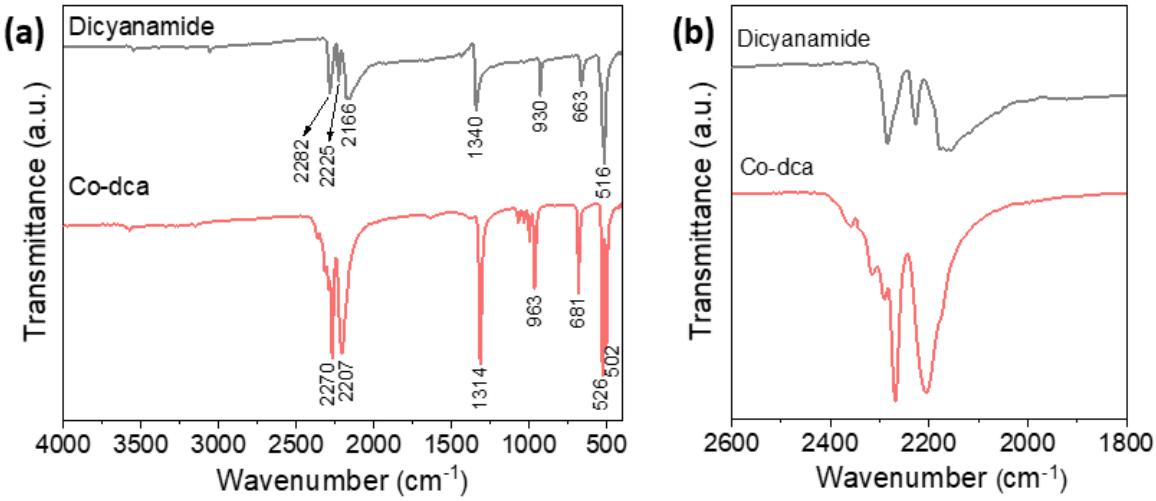

Figure 56. ATR-FTIR spectra of Co-dca sample and $NaN(CN)_2$ between (a) 400−4000 cm^{-1}, and (b) 1800−2600 cm^{-1}.

Table 6. ATR- FTIR data of Co-dca sample.

Vibration	**Wavenumber (cm^{-1})**
δ(N−C≡N)	502
γ(N−C≡N)	526
δ(N−C≡N)	681
ν(N−C)	963
ν(N−C)	1314
ν(C≡N)	2207
ν(C≡N)	2270

The obtained experimental powder XRD pattern is identical to a previously reported $Co(dca)_2$ crystal structure (CCDC 117729), in which octahedral cobalt sites are surrounded by dicyanamide ligands to form a 3D coordination network (Figure 57a). Dicyanamide ligand uses both its nitrile (–CN) and amide (NC–N–CN) nitrogen atoms for coordination (Figure 57b) [149], [152].

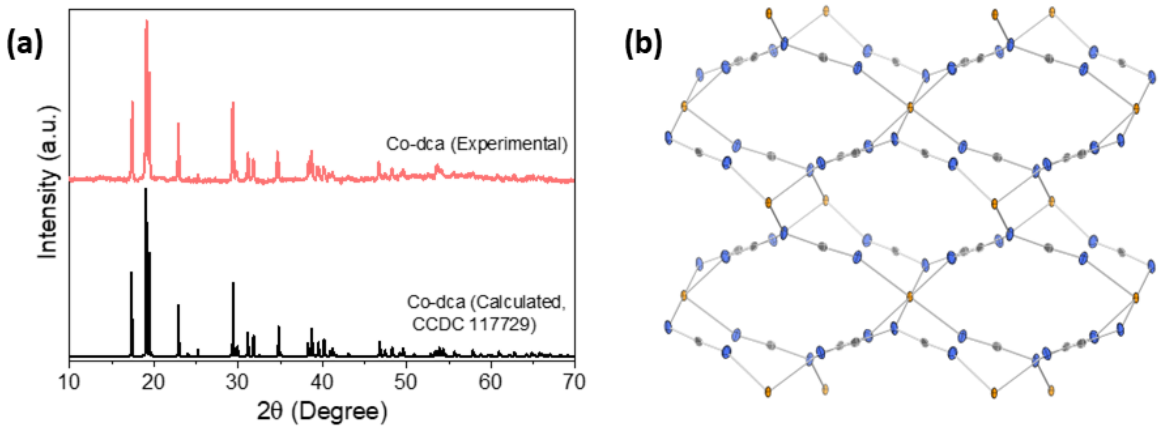

Figure 57. (a) Experimental and calculated (CCDC 117729) XRD patterns of Co-dca. (b) (b) 3D structure $Co(dca)_2$ (Color code: Co = orange; C = gray; N = blue).

The morphology and structure of the sample were studied by SEM and TEM analysis. SEM and TEM images reveal that the Co-dca is constructed with cubic brick subunits with a micrometer size (Figures 58 and 59a-c). The chemical composition of Co-dca was determined by EDS, and the Co:C:N elemental ratio was found to be 7.7:38.7:52.1, which is in agreement with the stoichiometric ratio of Co-dca (Figure 59d).

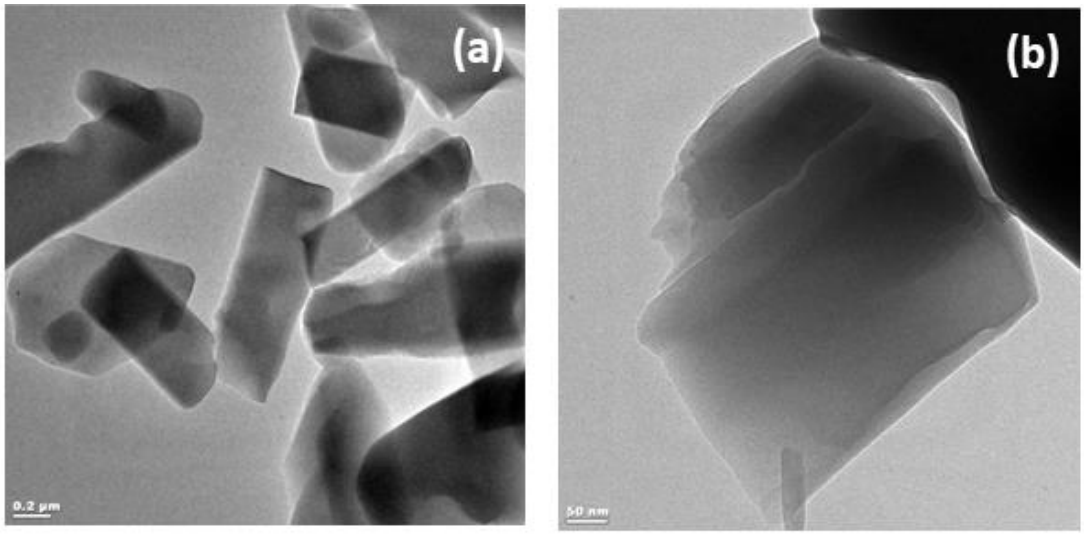

Figure 58. (a-b) TEM images of Co-dca.

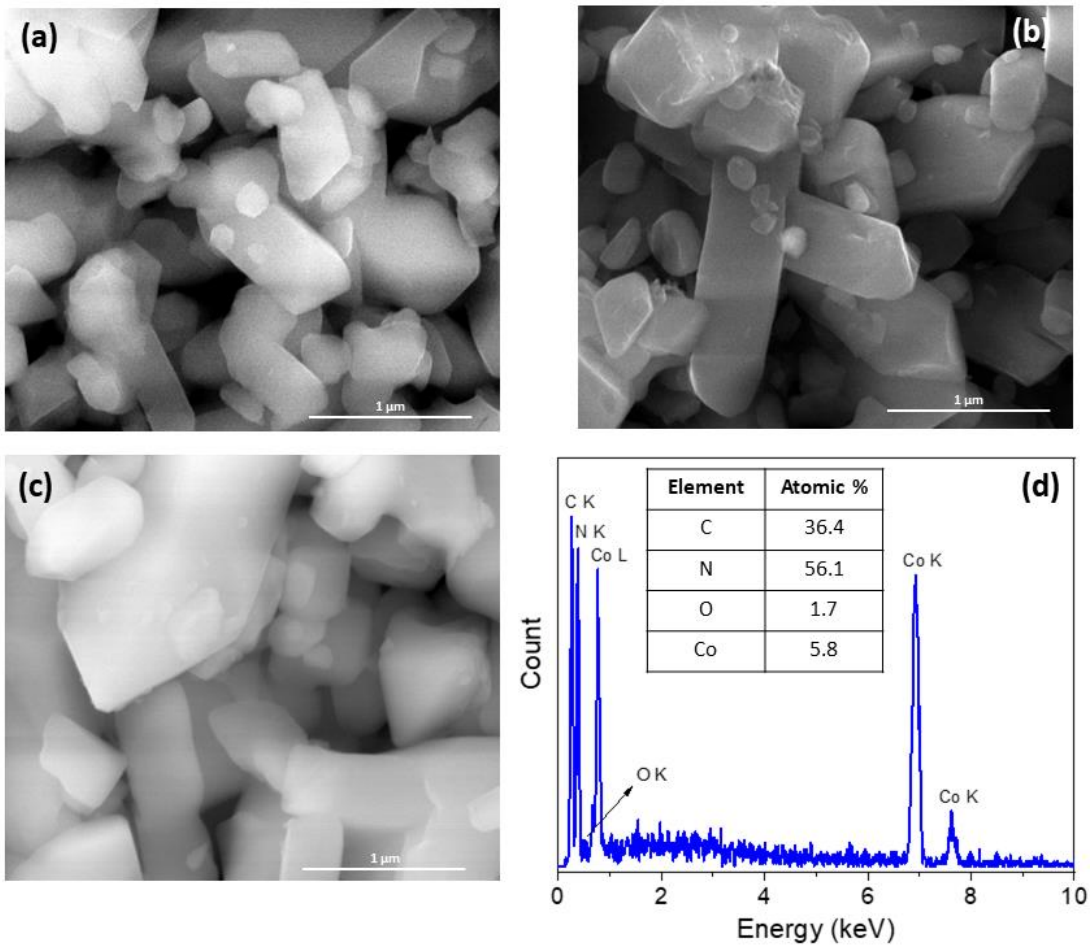

Figure 59. (a-c) SEM images and (b) SEM-EDS analysis of Co-dca. Inset: the atomic ratio of all elements for the Co-dca.

An XPS analysis was carried out to investigate the chemical composition of the Co-dca. In the C 1s spectrum, the three peaks at 284.8, 287.1 and 288.6 eV correspond to C−C, carbon bonded to N in the dicyanamide (N−C≡N), and the surface C=O bond, respectively (Figure 60a) [220], [221]. The N 1s region is deconvoluted to two peaks at 398.7 and 399.9 eV, which are assigned to the nitrile nitrogen and the central amido nitrogen in the dicyanamide structure, respectively (Figure 60b) [222], [223]. The Co 2p spectrum exhibits two broad peaks at 781.8 and 797.9 eV, ascribed to Co $2p_{3/2}$ and Co $2p_{1/2}$, respectively. Another doublet at slightly higher binding energies can be attributed to shake-up satellite peaks (Figure 60c). Previous studies reveal that the Co $2p_{3/2}$−Co $2p_{1/2}$ spin-orbit splitting is 15 eV for diamagnetic Co(III) complexes and 16 eV for paramagnetic Co(II) complexes

[185]. Moreover, cobalt(II) complexes show broader $2p_{3/2}$ and $2p_{1/2}$ lines with more intense satellite peaks than cobalt(III) complexes [180], [183]. The presence of satellite peaks, broad $2p_{3/2}$ and $2p_{1/2}$ lines, and spin-orbit splitting of 16.1 eV suggests that cobalt cations are mainly in their +2 oxidation states in Co-dca [180], [224].

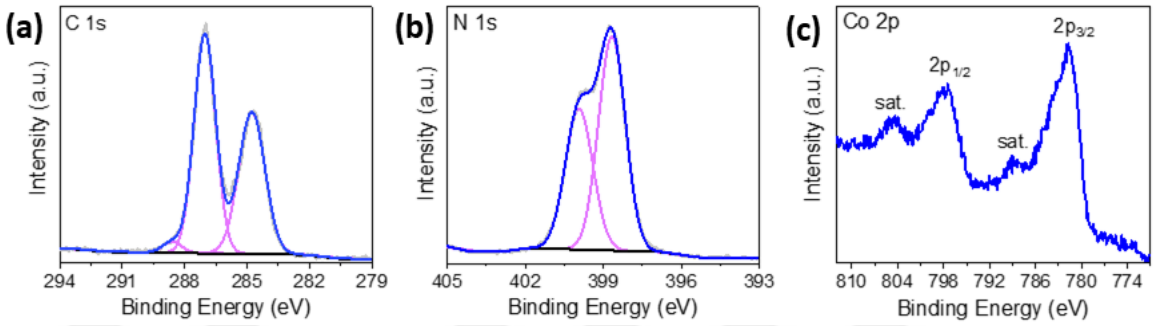

Figure 60. XPS spectra of (a) C 1s, (b) N 1s, and (c) Co 2p for pristine Co-dca.

5.2.2 Photocatalytic Reduction of CO_2

The photocatalytic activity of Co-dca was evaluated in the presence of a ruthenium PS (Ru PS), $[Ru(bpy)_3]Cl_2 \cdot 6H_2O$ (bpy=2'2−bipyridine), and an electron donor, TEOA, under visible light irradiation. A series of control experiments were performed to determine the role of each component in the photocatalytic CO_2 reduction process (Figure 61a-b). In the presence of the PS and catalyst (10 mg), CO_2 was reduced into CO with a rate of 2.54 µmol h^{-1} and H_2 with a rate of 0.7 µmol h^{-1}, which yields a selectivity of 79% (*entry 1*). The complete inhibition of the activity without a Ru PS or without light irradiation (dark condition) proves that the CO_2 reduction process involves the excitation of the photosensitizer by the absorption of light (*entries 2 and 3*). When the catalyst, Co-dca, is not present, the amount of produced CO is reduced drastically from 2.54 µmol h^{-1} to 0.37 µmol h^{-1} and an approximately three-fold increase is observed in the amount of evolved H_2. In other words, HER dominates over CO_2RR when Co-dca is absent, indicating the critical role of Co-dca as the catalyst in selective photocatalytic CO_2RR (*entry 4*). To

examine the effect of dca ligand on the catalytic activity of $[Ru(bpy)_3]^{2+}$, bare dca was employed in the photocatalytic CO_2 reduction (*entry 5*). The total production of CO and H_2 was significantly decreased, which reveals that the interaction between dca and decomposed Ru PS does not lead to an active catalyst for CO_2RR and HER. $Co(NO_3)_2$ was also replaced with Co-dca to elucidate the effect of dca groups on the catalytic activity (*entry 6*). When $Co(NO_3)_2$ is used as the catalyst, a similar CO production rate is obtained to the "without catalyst" case, *entry 2*, while HER activity increases up to around 8.1 μmol h^{-1}. The dramatic difference in the selectivity indicates that a cobalt site surrounded with nitrogen atoms of dca ligand is selective towards CO_2RR, while the dominant process is HER when a bare cobalt ion is surrounded with oxygen atoms [225], [226]. Our photocatalytic experiments also confirm that CO_2-to-CO conversion is not observed when TEOA is replaced with triethylamine (TEA; *entry 7*). Under the N_2 atmosphere, no generation of CO was observed, confirming that CO is derived exclusively from CO_2, as expected (*entry 8*).

We further studied the effect of the concentration of Ru PS on photocatalytic performance (Figure 61c). The H_2 evolution rate increases with increasing the concentration of the Ru PS. The activity of CO_2RR reaches a maximum in the presence of 0.5 mM Ru PS. However, the selectivity for CO_2-to-CO conversion is gradually reduced with increasing the amount of Ru photosensitizer, and the highest selectivity is obtained when 0.1 mM Ru is used (93%).

When the amount of catalyst is varied, CO_2RR activity reaches a maximum value of 254 μmol g^{-1} h^{-1} when 10 mg catalyst is used (Figure 61d). In contrast, the H_2 production rate is gradually reduced with increasing the amount of catalyst, revealing that Co-dca is more selective towards CO_2 reduction than H_2 evolution. The selectivity profiles in Figure 61c,d, thus, suggest that catalytic HER mainly occurs on the ruthenium sites, which are

produced by the decomposition of molecular $[Ru(bpy)_3]^{2+}$ complexes during photoexcitation [49], [227], [228].

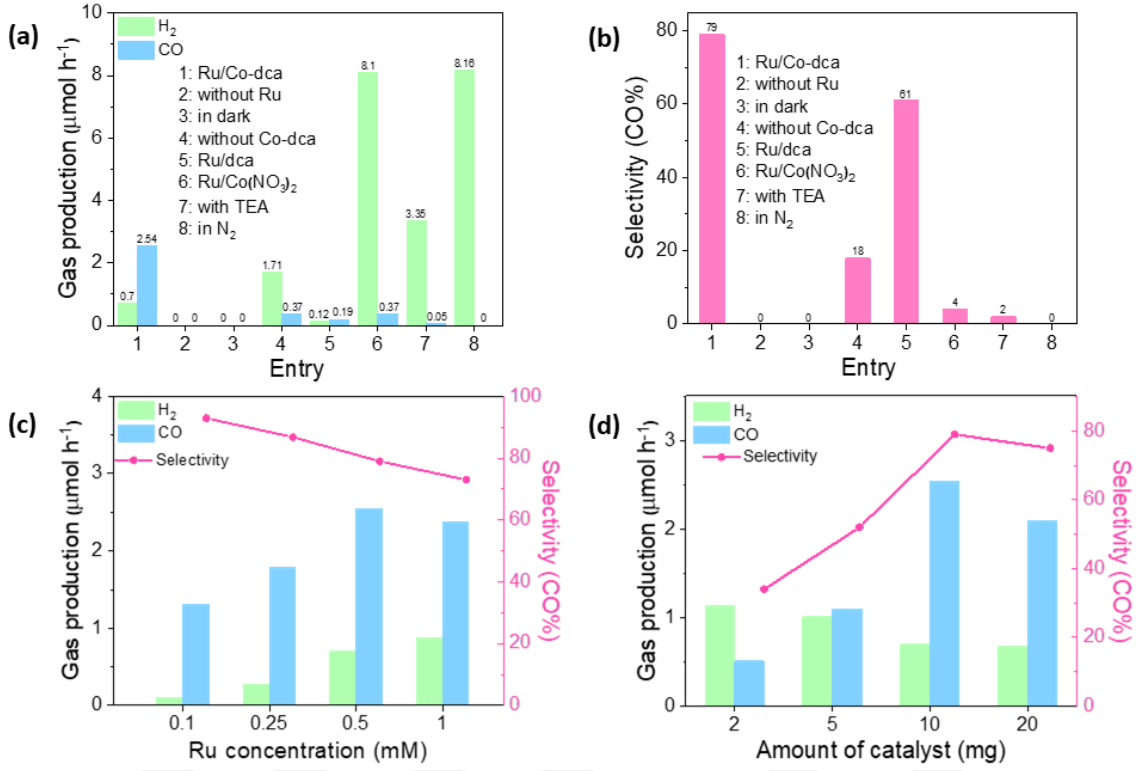

Figure 61. (a) Rates of CO and H_2 evolution, and (b) corresponding selectivity of photocatalytic CO_2 to CO conversion over H_2 evolution. The reactions are performed with Co-dca, $[Ru(bpy)_3]^{2+}$, and TEOA (*entry 1*), without $[Ru(bpy)_3]^{2+}$ (*entry 2*), without light (*entry 3*), without Co-dca (*entry 4*), when bare dca ligand is used as the catalyst *(entry 5)*, when Co-dca is replaced with $Co(NO_3)_2$ as the catalyst (*entry 6*), when TEOA is replaced with TEA (*entry 7*), and when the measurement is performed under N_2 atmosphere in place of CO_2 (*entry 8*). Regular reaction conditions: 10 mg catalyst, 3.74 mg $[Ru(bpy)_3]Cl_2{,}6H_2O$ (0.5 mM), 8 mL acetonitrile, and 2 mL TEOA at 25 °C, 30 min purging with CO_2 under visible light irradiation ($\lambda > 420$ nm). (c) The effect of the concentration of $[Ru(bpy)_3]Cl_2$ on the evolution of CO, H_2, and the selectivity of CO over H_2 under photocatalytic conditions. (d) The effect of the quantity of Co-dca on the evolution of CO, H_2, and the selectivity of CO over H_2 under photocatalytic conditions.

Studies on the reaction time reveal a linear relationship between the amount of CO and the irradiation time during the 1st hour of the photocatalytic process. The activity is,

however, gradually lost and the CO production rate significantly decreases during the 2nd cycle (Figure 62).

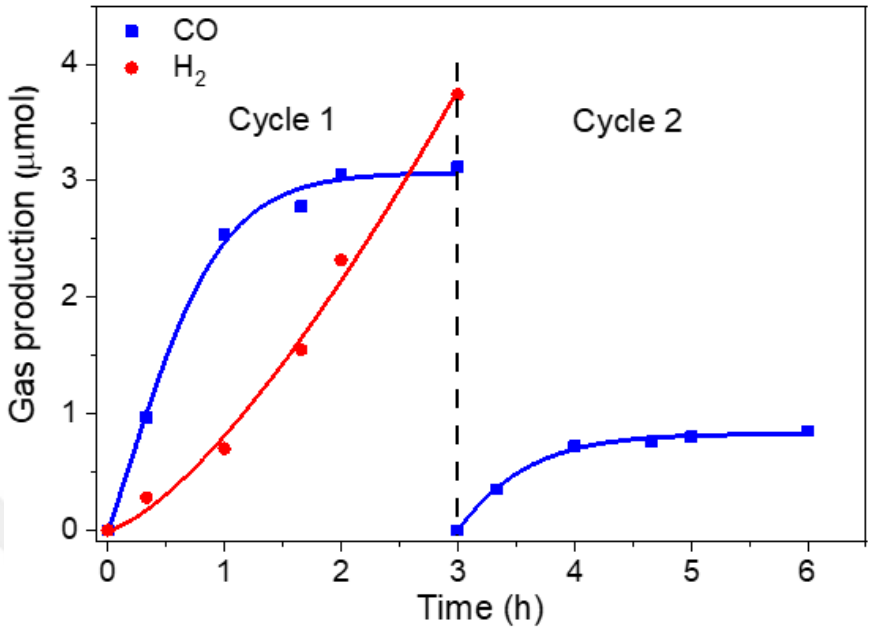

Figure 62. Yields of H_2 and CO from the CO_2 under visible light irradiation over 2 cycles. Reaction conditions: 10 mg Co-dca, 3.74 mg $[Ru(bpy)_3]Cl_2.6H_2O$ (0.5 mM), 8 mL acetonitrile, 2 mL TEOA, 25 °C, 30 min purging with CO_2, under visible light irradiation ($\lambda > 420$ nm). After the first cycle, the catalyst was dispersed in a fresh solution, and 3.74 mg of Ru photosensitizer was added.

The catalytic activity of Co-dca was compared with CoFe-PB, which has recently been studied for photocatalytic CO_2RR in the presence of Ru PS. The maximum activity for CoFe-PB was obtained when the concentration of the Ru PS was 1 mM. Co-dca exhibits a CO generation activity of 2.38 μmol h^{-1} in the 1st hour, which is ca. 3.5 times higher than that of CoFe-PB (Figure 63a). The higher selectivity of CO_2RR obtained for Co-dca compared to CoFe-PB reveals that cobalt is more selective towards CO_2RR when it is surrounded with dicyanamide groups compared to cyanide groups (Fig. 63b).

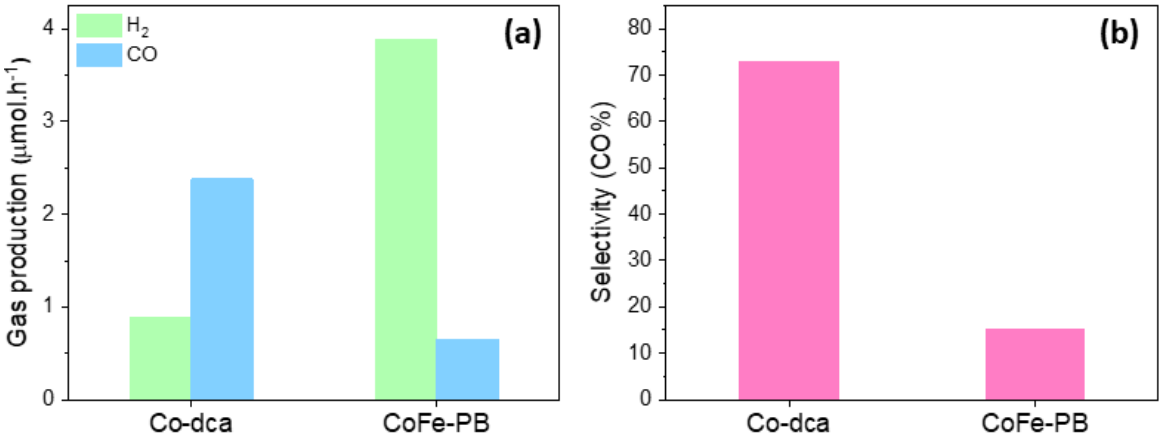

Figure 63. Comparison of (a) the photocatalytic CO and H_2 evolution activity and (b) corresponding selectivity of photocatalytic CO_2 to CO conversion over H_2 evolution of Co-dca and CoFe-PB. Reaction conditions: 10 mg catalyst, 7.48 mg $[Ru(bpy)_3]Cl_2.6H_2O$ (1 mM), 8 mL acetonitrile, 2 mL TEOA, 25 °C, 30 min purging with CO_2, under visible light irradiation ($\lambda > 420$ nm).

Previous studies on CO_2RR report that water should be used for photocatalytic CO_2 reduction [49]. Our results, however, demonstrate that Co-dca exhibits a higher performance in the absence of water (Figure 64).

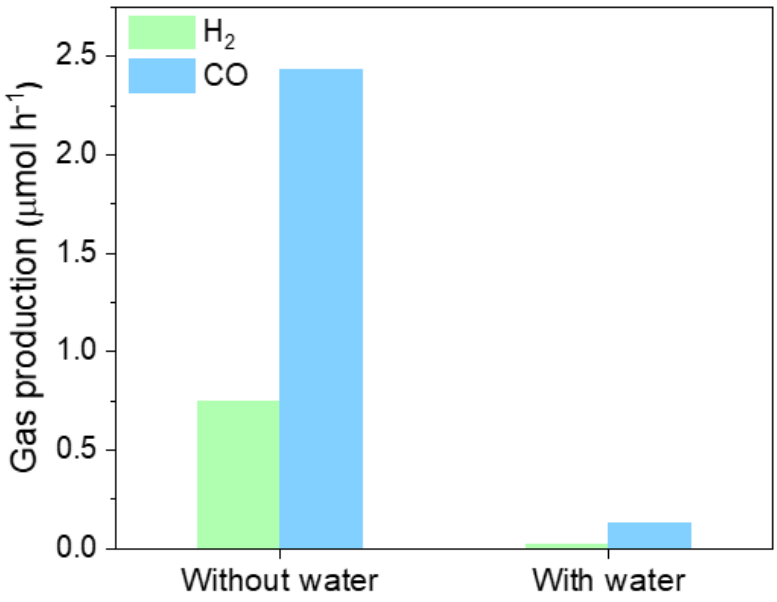

Figure 64. Photocatalytic CO_2 reduction activity of Co-dca sample without water (MeCN/TEOA, 4/1, v/v) and with water (MeCN/H_2O/TEOA, 3/1/1, v/v/v).

5.2.3 The Solvent Effect on Co-dca

Co-dca was dispersed in various solvents to understand the effect of the solvent molecules on the structure of the catalyst (Figure 65a). Co-dca exhibits a pink color in H_2O and MeCN similar to its color in the powder form, a red color in TEOA and H_2O/TEOA, and a dark green color in MeCN/TEOA and MeCN/H_2O/TEOA solutions. Note that Co-dca is not soluble in MeCN. When the transparent solution of Co-dca in the MeCN/TEOA solution is bubbled with CO_2 and stirred for 2 h, the dark greenish color turns to a cloud due to the formation of a precipitate (Figure 654b). Infrared studies performed on this precipitate reveal that the coordination environment of cobalt sites is altered slightly as cyanide stretch modes shift to lower wavenumbers compared to pristine Co-dca powder (Figure 65c).

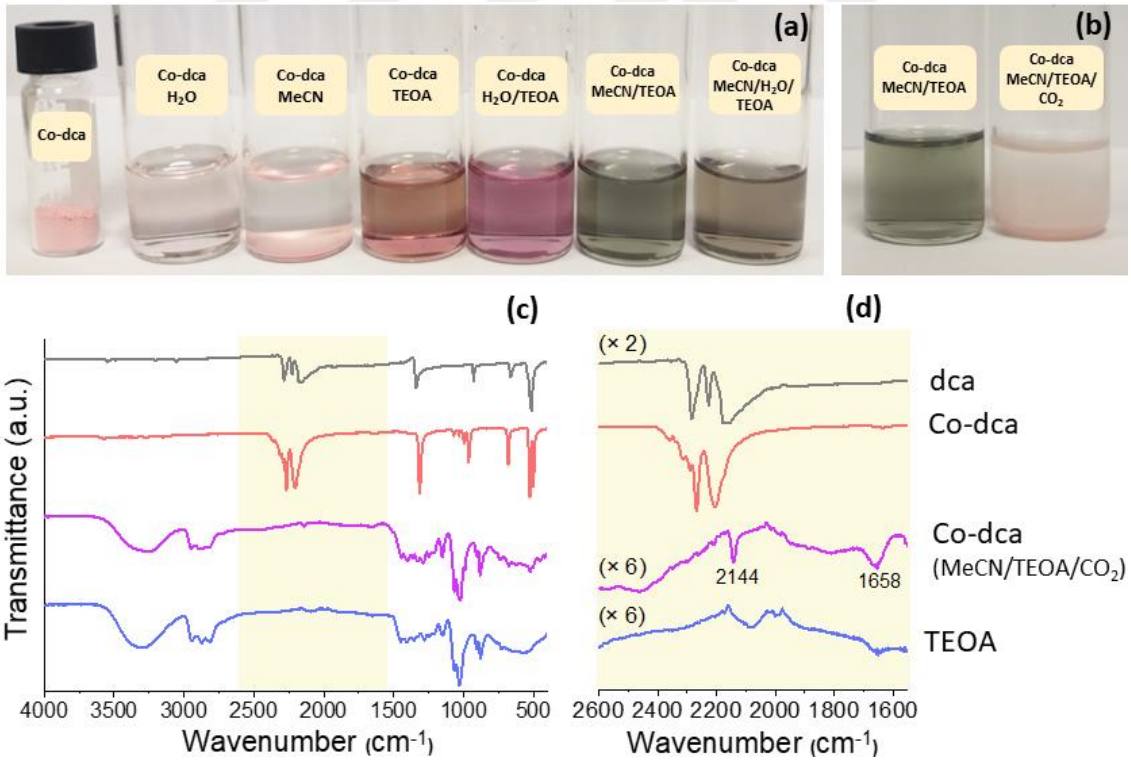

Figure 65. (a) Co-dca powder dispersed in different solutions. (b) Co-dca powder dispersed in MeCN/TEOA solution with and without CO_2 bubbling. ATR-FTIR spectra of dca, Co-dca, Co-dca in MeCN/TEOA/CO_2 solution, and TEOA between (c) 400−4000 cm^{-1}, and (d) 1550−2600 cm^{-1}.

Previous studies indicate that TEOA serves not only as a scavenger but also participates actively in the catalytic mechanism by binding to the catalytic metal center to assist the activation of CO_2 molecules [229], [230]. The color change with the addition of TEOA could, thus, be attributed to the coordination of TEOA to the cobalt sites and the formation of a precipitate after purging with CO_2 is due to the binding of TEOA groups to the CO_2 molecule. The C=O stretching vibration at 1658 cm^{-1} is observed for Co-dca in MeCN/TEOA/CO_2, which supports the assumption that TEOA may react with CO_2 (Figure 65d) [231].

The UV−Vis absorption spectra of Co-dca in H_2O and MeCN/TEOA solutions were investigated (Figure 66). The clear color change and different absorption profile in TEOA could be attributed to the coordination of TEOA molecules to accessible cobalt sites.

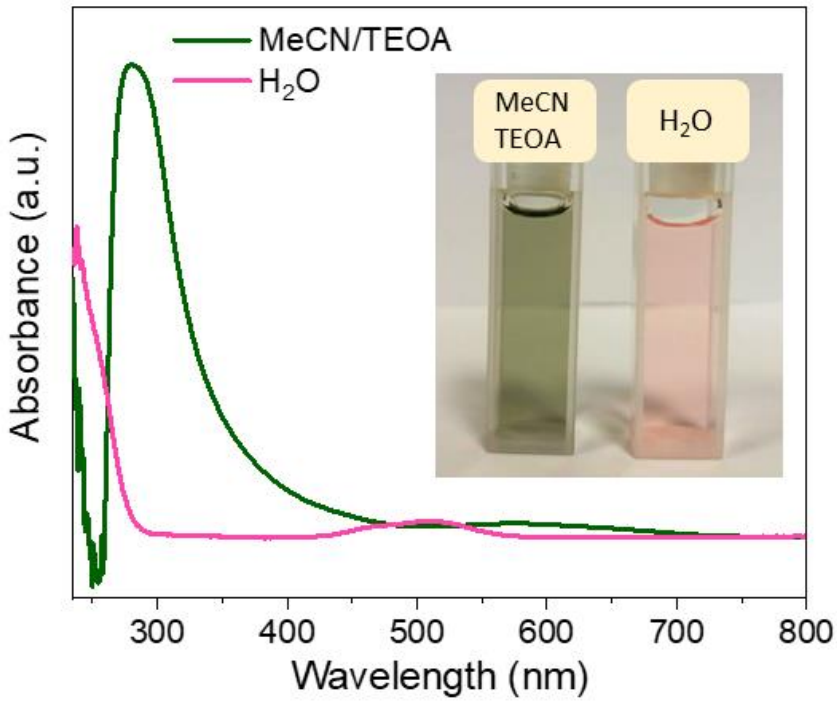

Figure 66. The UV−Vis absorption spectra of Co-dca (10 mg) in MeCN/TEOA and H_2O solutions. Inset: Co-dca powder dissolved in MeCN/TEOA and H_2O solutions.

5.2.4 Post-catalytic Characterizations

The chemical structure of the post-catalytic sample was investigated with FTIR, XPS, UV−Vis absorption, and TEM techniques. The post-catalytic Co-dca sample exhibits CN bands similar to the Co-dca in MeCN/TEOA/CO_2 solution, suggesting that the dca is still retained in the structure after the photocatalytic experiment. The additional bands in the spectrum can be attributed to TEOA (Figure 67a). Moreover, the post-catalytic sample exhibits the C=O stretching vibration at 1656 cm^{-1} (Figure 67b).

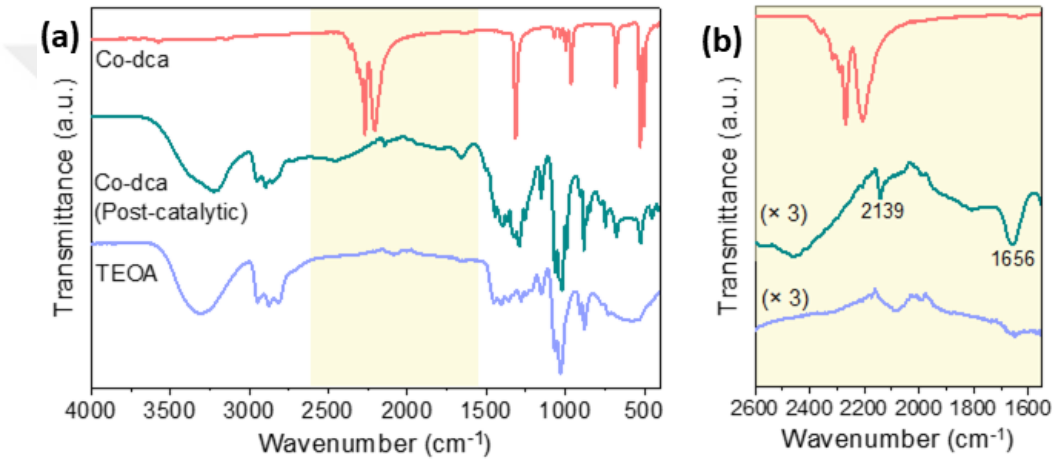

Figure 67. ATR-FTIR spectra of Co-dca, post-catalytic Co-dca, and TEOA between (a) 400−4000 cm^{-1}, and (b) 1550−2600 cm^{-1}.

Co $2p_{3/2}$ and $2p_{1/2}$ peaks get narrower, and the spin−orbit splitting (ΔE = 15.6 eV) is reduced slightly compared to the pristine Co-dca, which indicates that Co^{2+} ions are partially oxidized to Co^{3+} during the photocatalytic process, as proposed for cobalt-based CO_2RR (Figure 68a) [232]. The UV−Vis absorption spectra of Co-dca and $[Ru(bpy)_3]^{2+}$ in MeCN/TEOA (8 mL/2 mL) solution and the supernatant solution of the post-catalytic sample are demonstrated in Figure 68b for comparison. $[Ru(bpy)_3]^{2+}$ displays a characteristic absorption at 453 nm attributed to the MLCT, along with a sharp band at 287 nm [233]. The UV−Vis absorption profile for the post-catalytic supernatant solution is

essentially the same as $[Ru(bpy)_3]^{2+}$, suggesting that Co-dca forms a precipitate during the photocatalytic process.

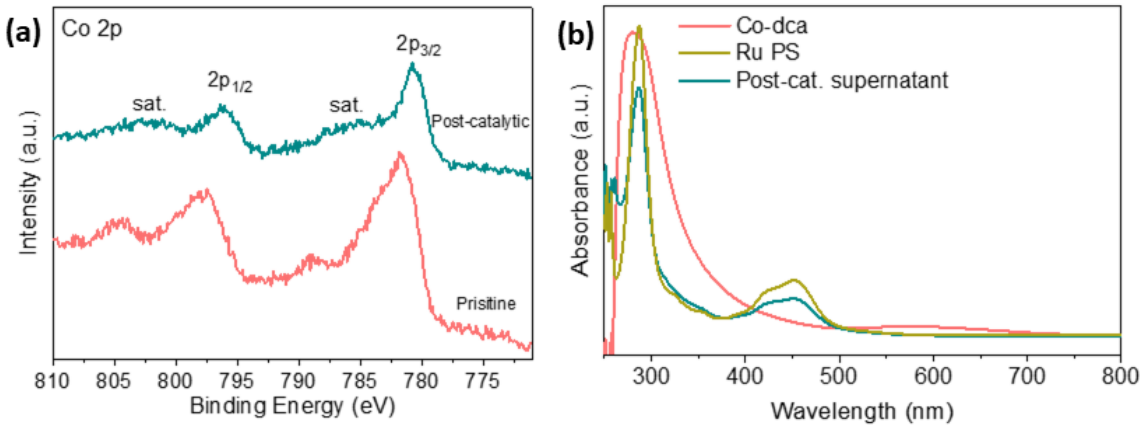

Figure 68. (a) XPS Co 2p spectra of pristine and post-catalytic Co-dca. (b) UV−Vis absorption spectra of Co-dca (10 mg), $[Ru(bpy)_3]Cl_2$ (0.5 mM), and supernatant solution of the post-catalytic sample. (All spectra were recorded in a solution containing 8 mL acetonitrile and 2 mL TEOA).

TEM images and EDS analysis reveal that Co-dca particles have been coated with slightly thick Co-TEOA layers, which could form by leaching of cobalt ions to coordinate to TEOA from multiple sites (Figure 69) [234]–[236]. The decrease in the activity of Co-dca in the 2nd cycle could, thus, be attributed to the transformation of active cobalt sites to inactive Co-TEOA layers.

Furthermore, the TEOA coordinated cobalt cations are significantly active in HER [225], [226], which could be the reason for the higher H_2 production selectivity of the photocatalytic system in the 2nd cycle (Figure 70). Overall, we suggest that TEOA coordinates to cobalt sites, which are active toward the CO_2RR process. TEOA binds further to cobalt sites during the photocatalytic process to produce Co-TEOA particles, which are inactive towards CO_2RR.

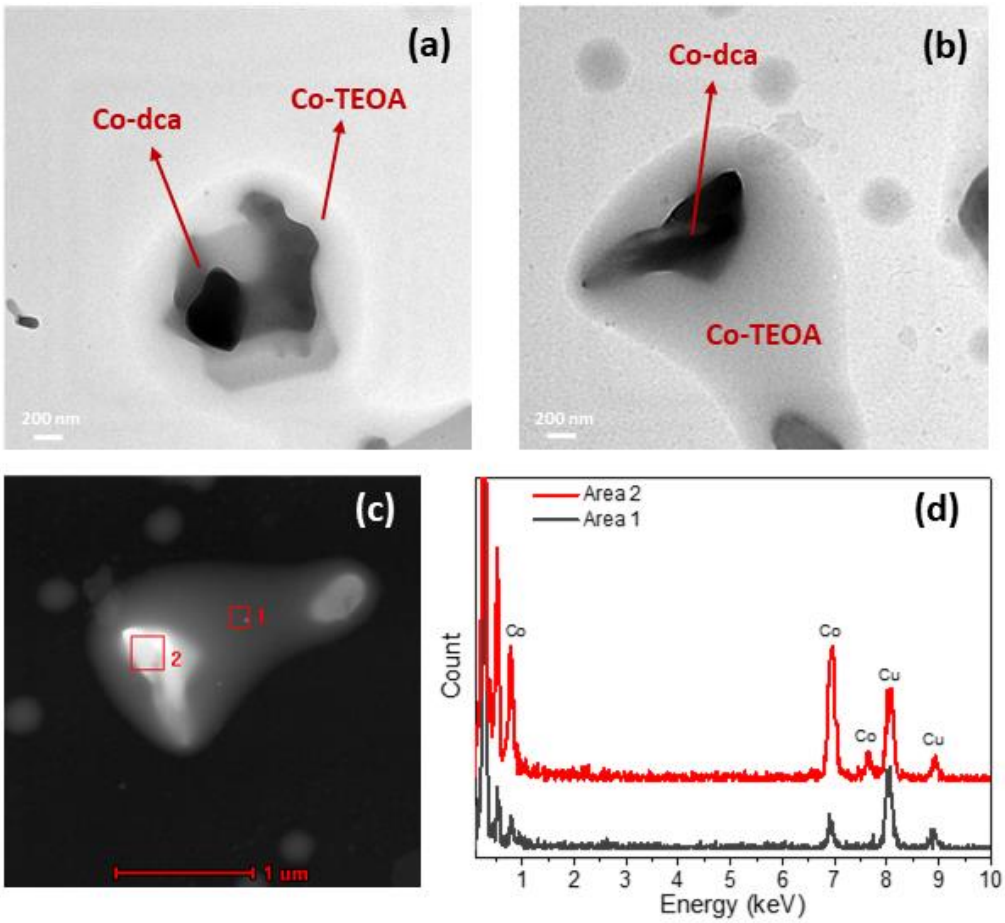

Figure 69. (a-b) TEM images, and (c) HAADF-STEM images of Co-dca for post-catalytic sample. (d) EDS elemental analysis of selected areas. The signal for Cu is from the TEM grid.

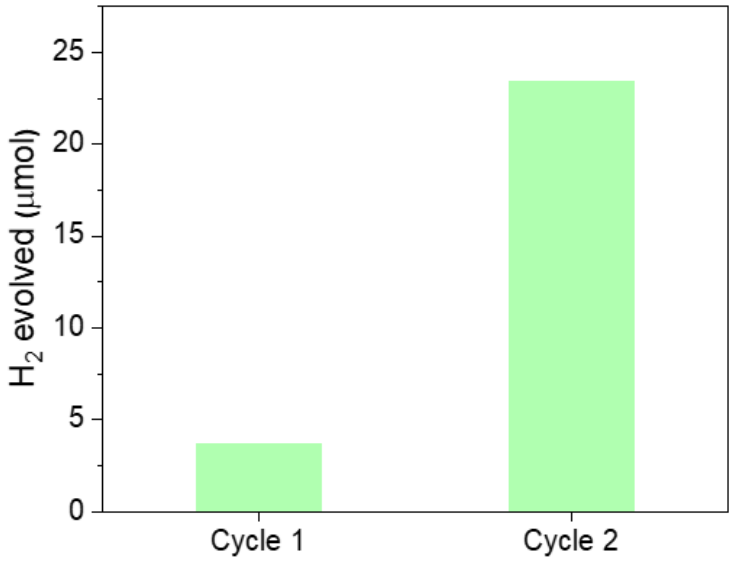

Figure 70. The amount of H_2 evolved during the first and second cycles.

5.3 Summary

In summary, a Co-dca coordination compound was successfully synthesized via a straightforward precipitation method. Characterization studies reveal that the compound exhibits an extended network structure, in which the cobalt sites are surrounded with the nitrogen atoms of the dicyanamide ligands. Photocatalytic studies indicate that Co-dca exhibits a CO_2-to-CO conversion rate of 254 μmol h^{-1} g^{-1} (0.5 mM Ru PS) and selectivity of as high as 93% CO (0.1 mM Ru PS). We also observed that the CO production activity of Co-dca is ca. 3.5 times higher than that of CoFe-PB, which has recently been investigated for photocatalytic CO_2RR. Characterization studies on the post-catalytic sample reveal the formation of the Co-TEOA particles, which are inactive towards CO_2RR.

Chapter 6

Photocatalytic Hydrogen Evolution by Cobalt Dicyanamide

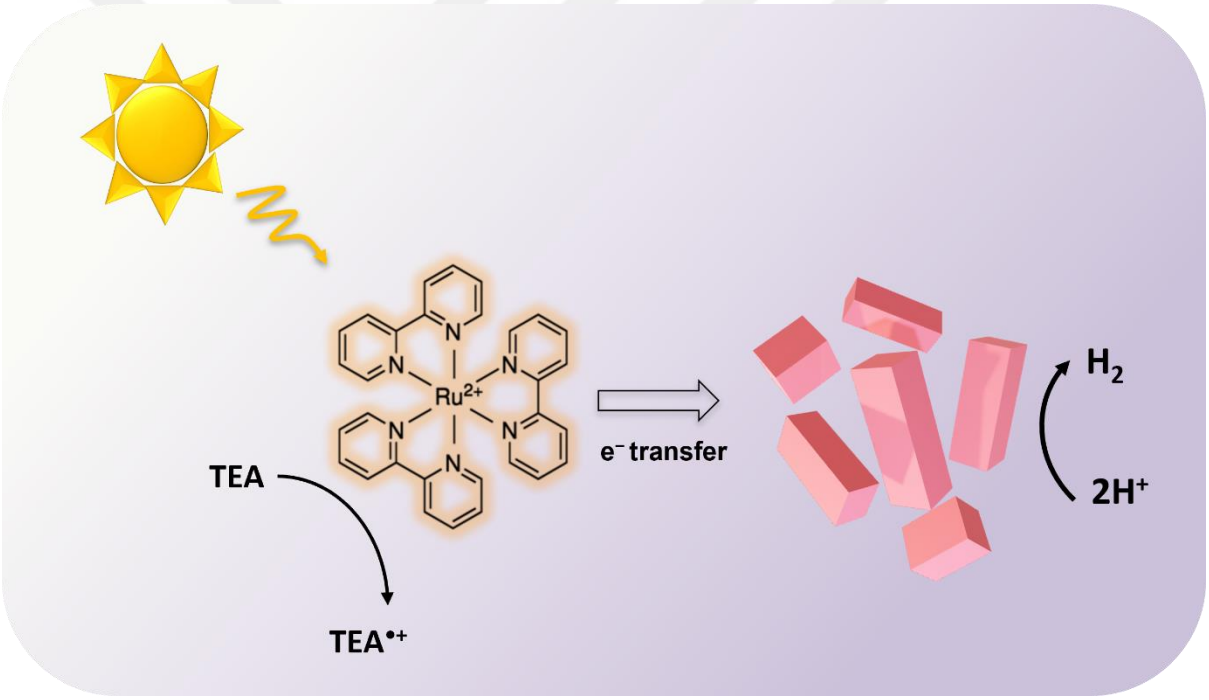

6.1 Experimental Procedure

6.1.1 Materials

Sodium dicyanamide ($NaN(CN)_2$, Acros Organics, 97%), cobalt(II) nitrate hexahydrate ($Co(NO_3)_2 \cdot 6H_2O$, Alfa Aesar, 99.9%), tris(2,2′−bipyridine)ruthenium(II) hexafluorophosphate ($[Ru(bpy)_3](PF_6)_2$, Sigma Aldrich, 98%), acetonitrile (MeCN, Sigma-Aldrich, >99.9%), triethylamine (TEA, Carlo Erba reagents, 99.5%). Deionized water (resistivity: 18 MΩ/cm) is used in all experiments.

6.1.2 Sample Preparation

***Synthesis of Co-dca*:** The synthesis procedure of Co-dca is similar to the 5.1.2 section.

***Preparation of Co-dca/TEA*:** For the preparation of Co-dca/TEA, 60 mg of as-synthesized Co-dca powder, 7.6 mL MeCN, 0.4 mL H_2O, and 2 mL of TEA were mixed and vigorously stirred for 20 h at room temperature. Then, the as-obtained precipitate was centrifuged, washed with distilled water, and dried at 75 °C overnight.

***Synthesis of Co-dca-TEA*:** Typically, 4 mmol of $NaN(CN)_2$ and 2 mmol of $Co(NO_3)_2 \cdot 6H_2O$ were separately dissolved in 3 mL of H_2O/TEA (2/1, v/v) mixed solution. Then, the former solution was added dropwise to the latter one and stirred for 4 h. The final precipitate was collected by centrifugation and washed thoroughly with water. The obtained solid was dried at 75°C.

6.1.3 Photocatalytic H_2 Evolution

The H_2 evolution studies were performed in a 16.5 mL round-bottom flask capped with a septum at room temperature. In a typical experiment, the reactor was filled with a mixed solution of 8 mL MeCN/H_2O (19/1; v/v) and 2 mL TEA containing 8.6 mg

$[Ru(bpy)_3](PF_6)_2$ (1mM), and 1 mg of catalyst. The reaction solution was purged with N_2 gas for 20 min before light illumination. The mixture was continuously stirred and irradiated under a 300 W Xe lamp (300 W; AM 1.5 global filter) with a 420 nm cutoff filter. 100 µL from the headspace of the reactor was injected into a GC to determine the amount of evolved H_2.

6.2 Results and Discussion

6.2.1 Synthesis and Structural Characterization of Materials

Co-dca was synthesized by a facile precipitation method (similar to the 5.1.2 section) [149], and the structure was investigated by Infrared, XRD, SEM, TEM, and XPS analysis. Cobalt ions are coordinated with dicyanamide groups to form a 3D network with a cubic brick morphology (Figure 71). All characteristic peaks of the $Co(dca)_2$ structure were observed in powder XRD analysis (Figure 72a) [237]. Absorption bands in the 2030–2420 cm^{-1} region of the FTIR spectrum of Co-dca correspond to the asymmetric and symmetric stretches of ν(C≡N) (Figure 72b). The details of structural, chemical, and morphological characterization of Co-dca are described in the 5.2.1 section.

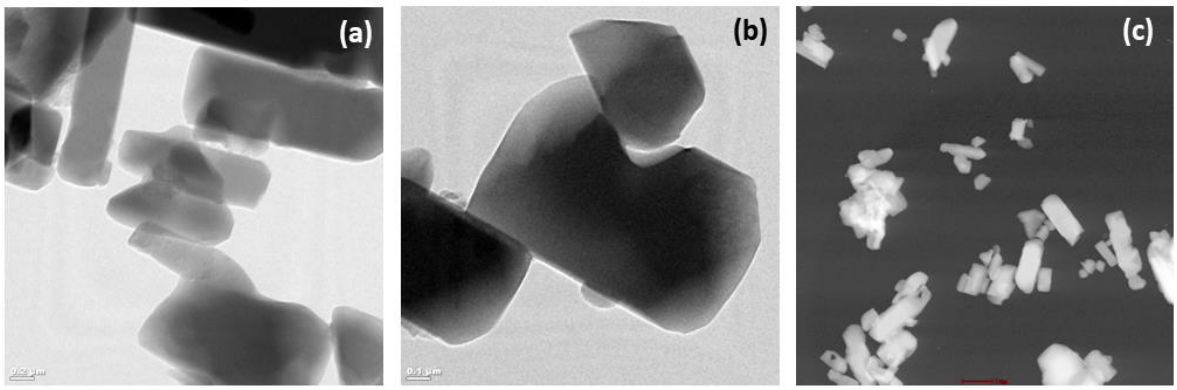

Figure 71. (a-b) TEM, and (c) HAADF-STEM images of Co-dca.

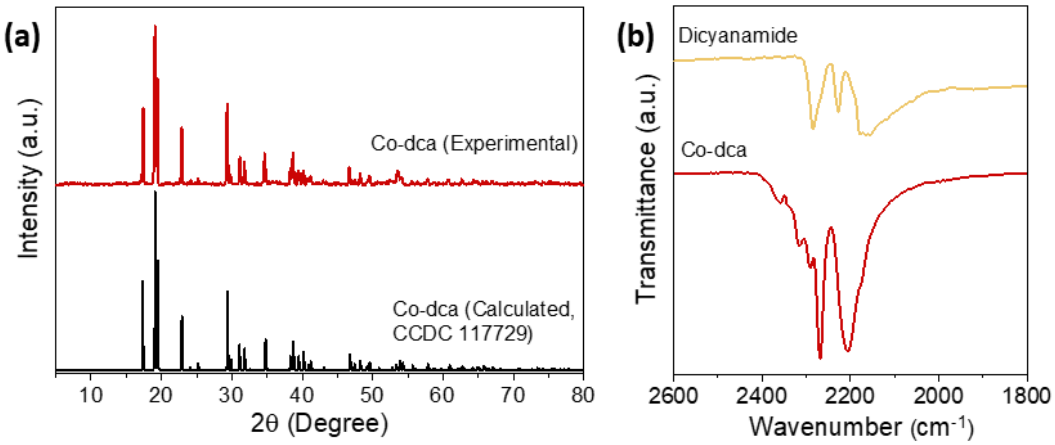

Figure 72. (a) Experimental and calculated (CCDC 117729) XRD patterns of Co-dca. (b) ATR-FTIR spectra of Co-dca and $NaN(CN)_2$ in the 1800–2600 cm^{-1} region.

Co-dca was dispersed in $MeCN/H_2O$/TEA solution (abbreviated as Co-dca/TEA) to study the influence of the TEA on the structure of the catalyst. Figure 73 illustrates the XRD patterns of both as-prepared Co-dca and Co-dca/TEA powders. A considerable decrease in the intensity of the crystalline peaks is clearly observed for the Co-dca/TEA sample. Previous studies reveal that metal dicyanamides form a network with low crystallinity when combined with proper N-containing co-ligands [238], [239].

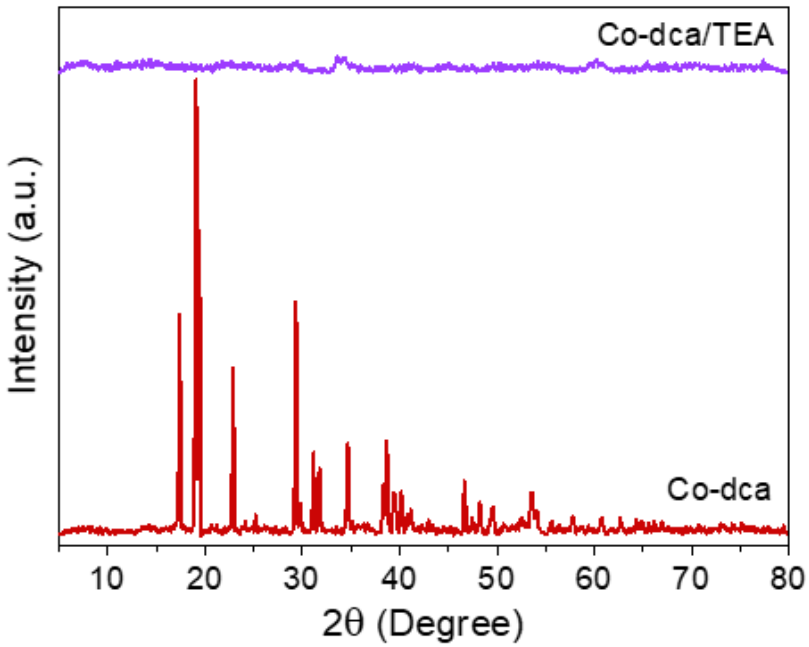

Figure 73. XRD patterns of Co-dca and Co-dca/TEA.

According to the Infrared analysis of Co-dca/TEA, cyanide stretch modes shift to lower wavenumbers in comparison to the pristine Co-dca, which could be attributed to a change in the coordination environment of cobalt sites (Figure 74). The stretching vibration of saturated C−H bonds (2800−3000 cm^{-1}) and the bending vibration of N−H bonds (1060−1385 cm^{-1}) are the characteristic bands of TEA [240], which are not observed in the FTIR spectrum of Co-dca/TEA, suggesting that TEA is not present in the cobalt dicyanamide network. According to the literature, tertiary alkylamines have almost no tendency to coordinate to metal salts unless stabilized by chelation [241].

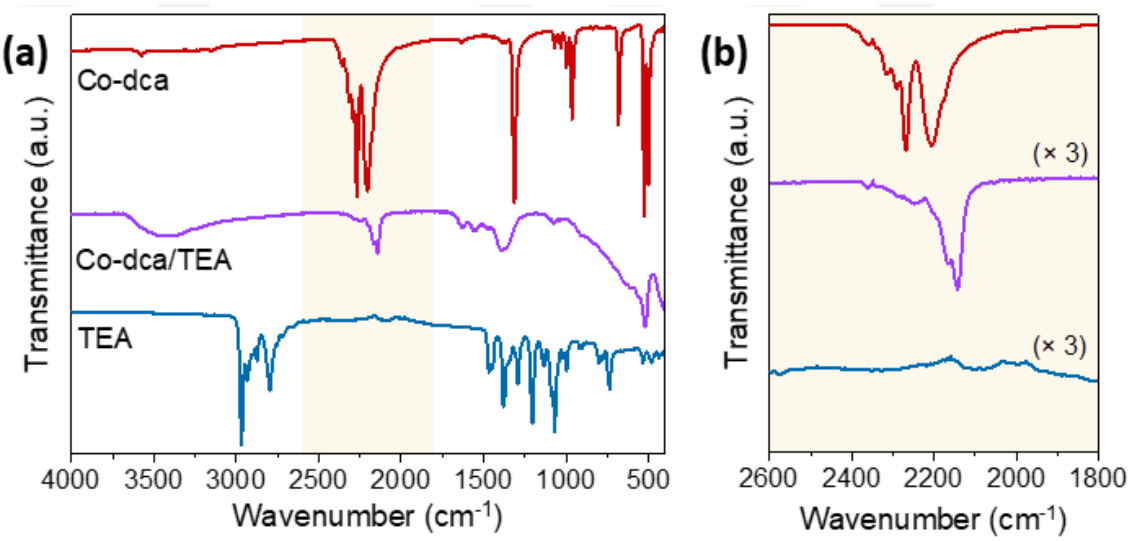

Figure 74. ATR-FTIR spectra of Co-dca, Co-dca/TEA, and TEA between (a) 400−4000 cm^{-1}, and (b) 1800-2600 cm^{-1}.

In the Co 2p spectrum of Co-dca, two prominent peaks at 782.1 and 798.3 eV are assigned to Co $2p_{3/2}$ and Co $2p_{1/2}$, respectively. Another doublet at slightly higher binding energies can be attributed to shake-up satellite peaks. The Co $2p_{3/2}$ and Co $2p_{1/2}$ peaks of the Co-dca/TEA sample are located at 780.9 and 796.6 eV, respectively (Figure 75). While the Co 2p profile of Co-dca reveals that the majority of cobalt ions are in +2 oxidation states, the narrower Co $2p_{3/2}$ and $2p_{1/2}$ peaks and lower spin−orbit splitting energy

difference compared to Co-dca verify that the cobalt cations are partially oxidized to Co^{+3} in Co-dca/TEA [180], [224].

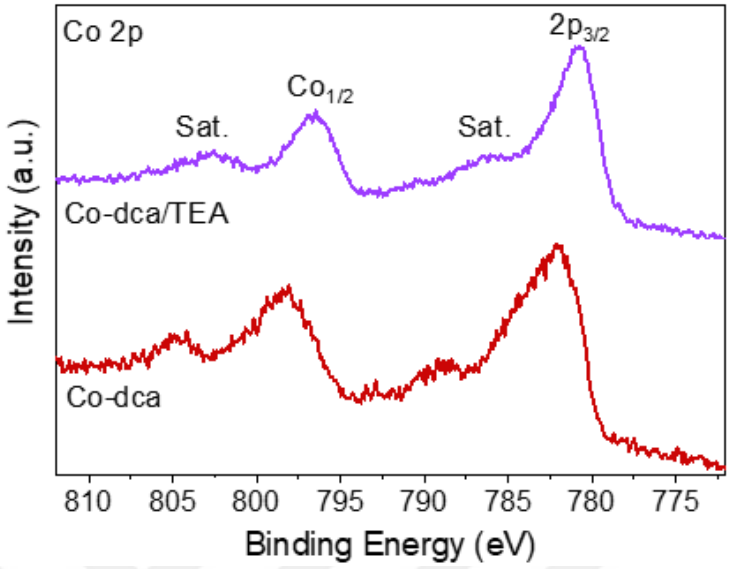

Figure 75. XPS Co 2p spectra of Co-dca and Co-dca/TEA.

TEM studies (Figure 76) depict that Co-dca/TEA is composed of a typical layered-like morphology. Moreover, the average particle sizes of Co-dca/TEA are relatively smaller than as-synthesized Co-dca. Overall, we suggest that the 3D network of Co-dca transforms into a 2D layered structure in the presence of a MeCN/H_2O/TEA mixed solution, which provides more active sites for the HER process. The reduction in crystallinity of Co-dca/TEA indicates that the TEA treatment decreases the dimensionality of the Co-dca structure. Furthermore, the coordination environment of cobalt cations is slightly altered in this condition.

For further investigation, Co-dca was synthesized in the mixed solution of H_2O/TEA instead of an aqueous solution (symbolized as Co-dca-TEA). Figure 77 shows the XRD patterns of Co-dca, Co-dca-TEA, and various $Co(OH)_2$ structures using the International Centre for Diffraction Data (ICDD) database. Co-dca-TEA XRD lines are matched to those

of $Co(OH)_2$, although the lines at 11.1º and 29.5º are not present in the cobalt hydroxide structure.

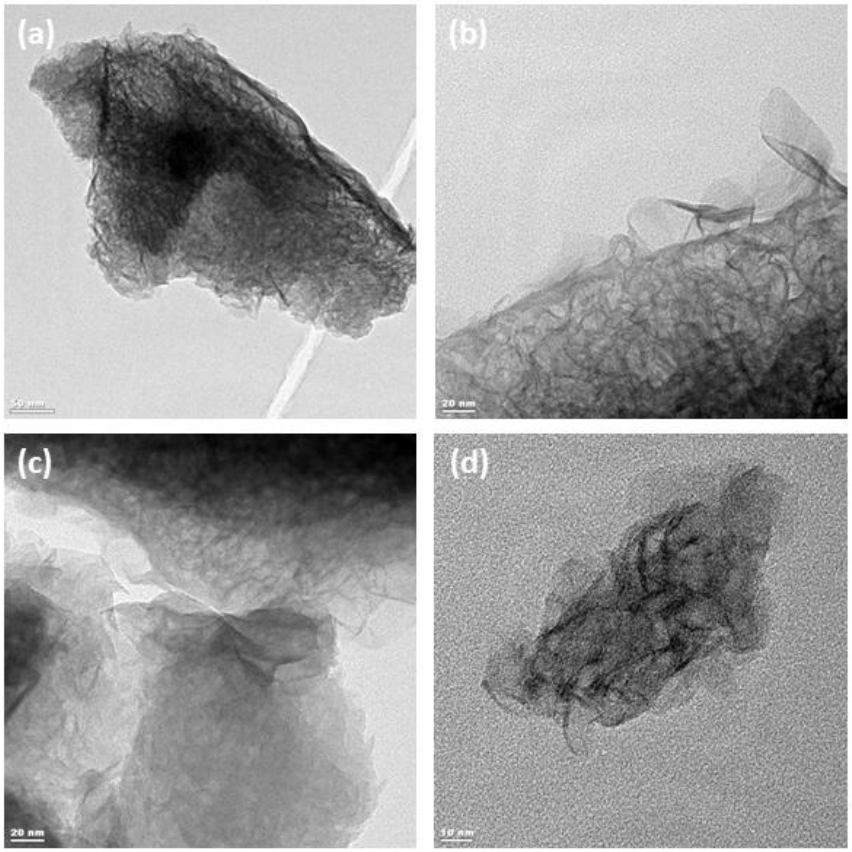

Figure 76. (a-d) TEM images of Co-dca/TEA.

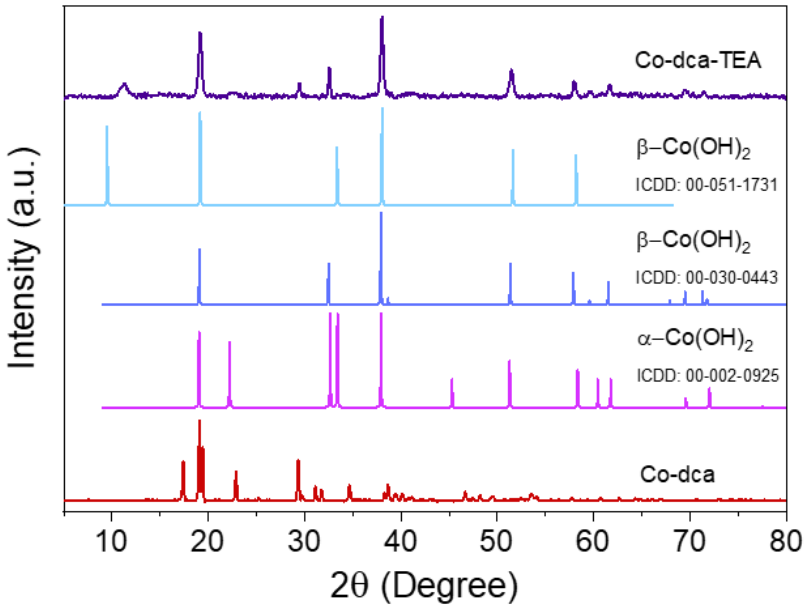

Figure 77. XRD patterns of Co-dca, Co-dca-TEA, and $Co(OH)_2$ structures.

The cyanide stretching mode of Co-dca-TEA is located in a slightly lower wavenumber than that of Co-dca (Figure 78). Similar to Co-dca/TEA, the characteristic bands of TEA are not found in the Co-dca-TEA spectrum, confirming that TEA is not present in the structure. A sharp band at 3630 cm^{-1} can be assigned to the stretching mode of O−H groups, probably due to the formation of $Co(OH)_2$. The XRD and FTIR results suggest the copresence of $Co(OH)_2$ and Co-dca in the Co-dca-TEA structure.

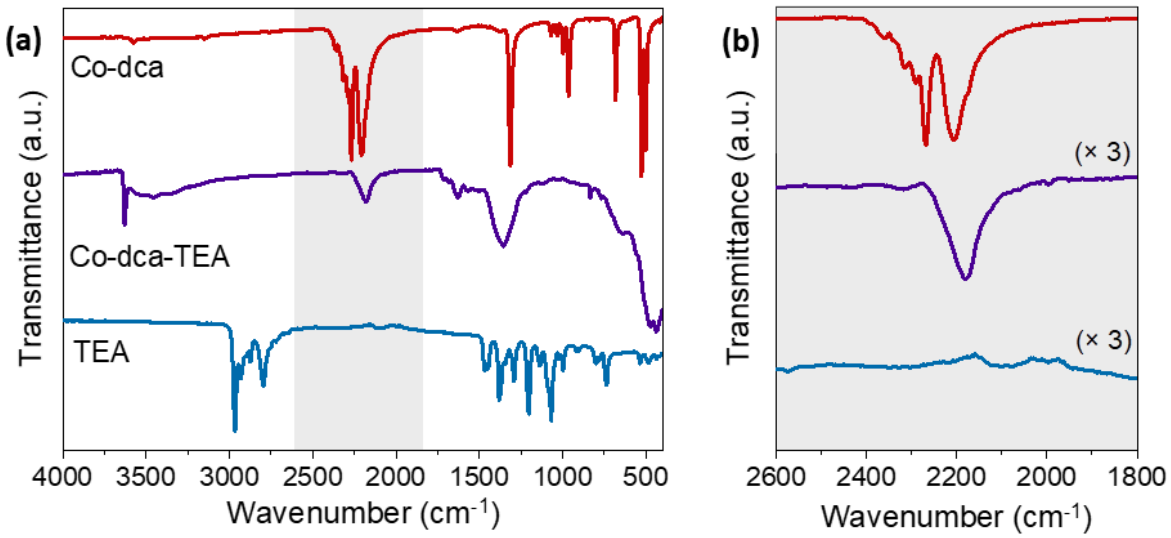

Figure 78. ATR-FTIR spectra of Co-dca, Co-dca-TEA, and TEA between (a) 400−4000 cm^{-1}, and (b) 1800-2600 cm^{-1}.

The surface morphology and particle size of Co-dca-TEA were investigated by the TEM technique (Figure 79). The Co-dca-TEA possesses a 2D sheet-like structure with lateral dimensions in the range of 50–500 nm. Moreover, Co-dca-TEA exhibits a thin nanosheet structure, which significantly differs from the mainly dense and stacked cubes of Co-dca. The EDS elemental analysis reveals the existence of Co, C, O, and N elements in the layers (Figure 80).

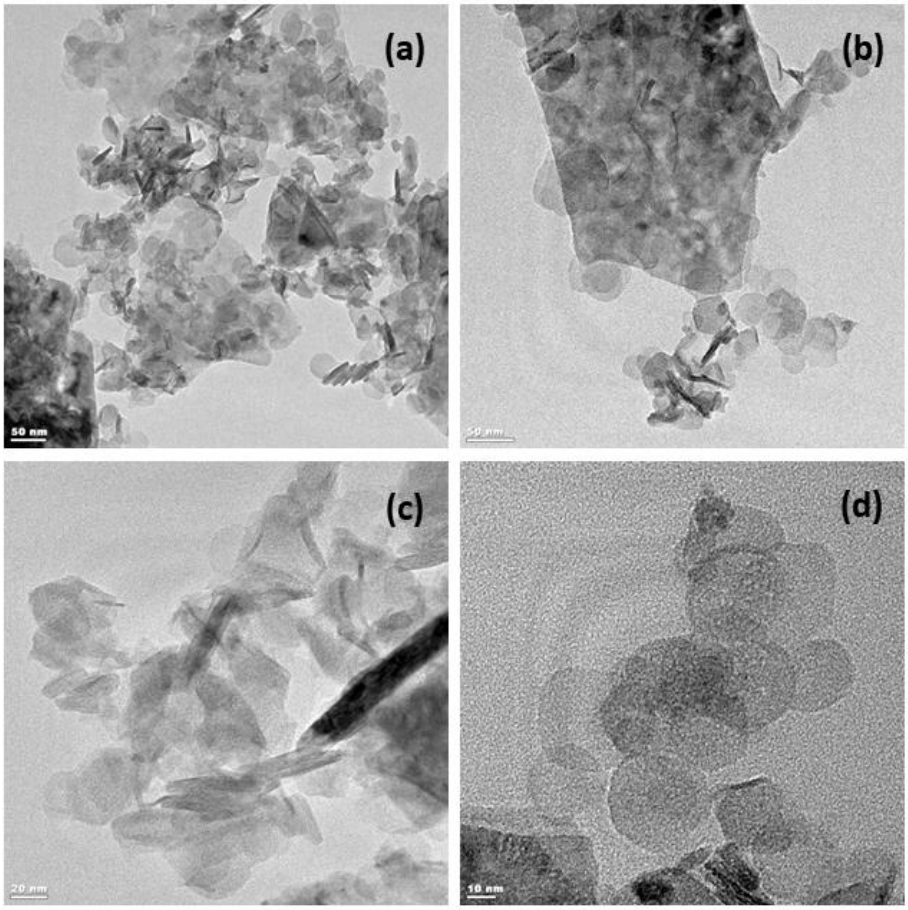

Figure 79. (a-d) TEM images of Co-dca-TEA.

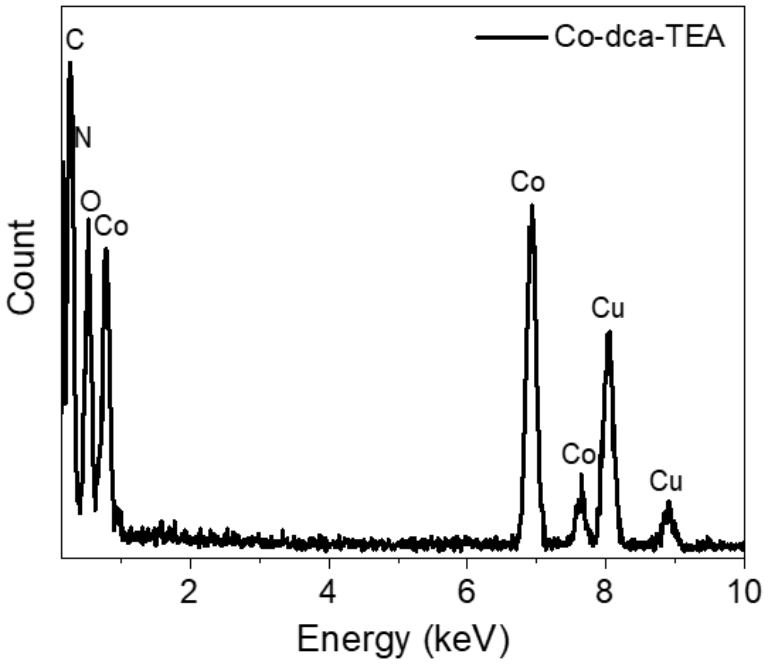

Figure 80. EDS analysis of Co-dca-TEA. The signal for Cu is from the TEM grid.

6.2.2 Photocatalytic HER Performance

The photocatalytic hydrogen-evolving ability of Co-dca was studied in a MeCN/H_2O (19/1 v/v) solution, in the presence of Ru PS, $[Ru(bpy)_3](PF_6)_2$, and a sacrificial electron donor under visible light irradiation. We conducted several control experiments to optimize reaction conditions. First, we investigated the influence of different sacrificial electron donors by evaluating the photocatalytic activity of the catalyst with TEA, TEOA, and ascorbic acid (AA). The highest catalytic activity was obtained when TEA was used, which is around 2 times higher than that obtained for TEOA and 16.8 times higher than that of AA in the MeCN/H_2O mixed solution, which affords the following trend: TEA > TEOA > AA. Furthermore, the rate of H_2 evolution decreases significantly with the increase in the water content (100%, by volume) in all electron donors. Note that Co-dca evolves no hydrogen gas when water is employed as the only solvent in the presence of TEOA (Figure 81a). Replacing MeCN with N,N-Dimethylformamide (DMF) in the reaction solution leads to a remarkable decrease in catalytic activity for both TEA and TEOA, which suggests MeCN plays an important role in the photocatalytic process (Figure 81b). Due to its superior catalytic performance, TEA is selected as the sacrificial electron donor.

We further performed photocatalytic experiments by varying the quantity of the catalyst (Figure 81a). When 1 mg Co-dca is used, the activity reaches a maximum value of 65100 μmol g^{-1} after 3 h of visible light irradiation. The value is the mean of four repeated experiments with a corresponding error bar. In contrast, the catalytic activity is reduced by increasing the amount of catalyst.

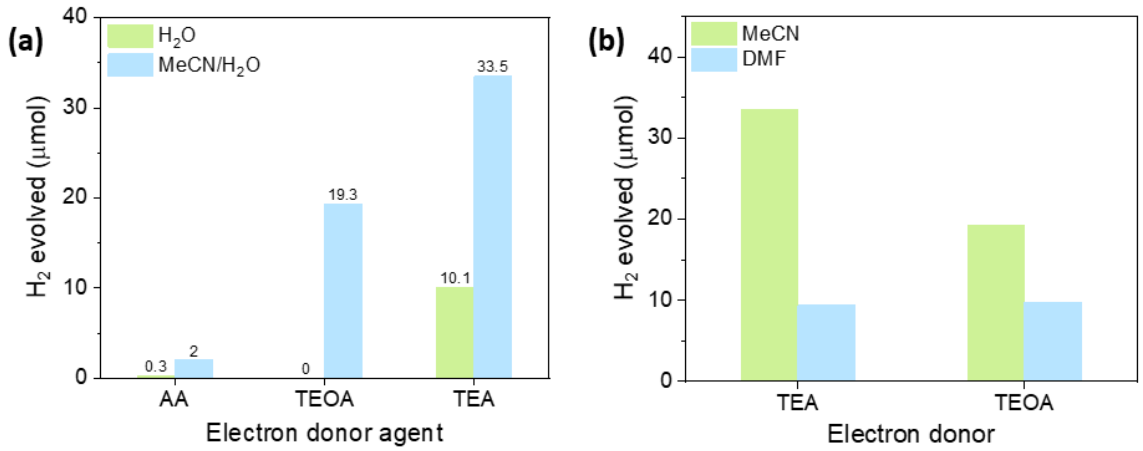

Figure 81. Rates of H_2 evolution (a) in the MeCN/H_2O (19/1 v/v) mixed solution (blue bars) and 100% (volume %) water (green bars) in the presence of TEA, TEOA, and AA as the electron donors, and (b) in the MeCN/H_2O (green bars) and DMF/H_2O (blue bars) mixed solutions in the presence of TEA and TEOA as the electron donor reagents. The reactions are performed using 1 mM $[Ru(bpy)_3](PF_6)_2$ and 10 mg of Co-dca under visible light irradiation for 2 h.

A series of control experiments were also performed to determine the role of each component in the HER process (Figure 82b). When the photocatalytic reaction was operated using the Ru PS, Co-dca, and TEA, the hydrogen generation rate was 65.1 µmol after 3 h irradiation (entry 1). Experiments in entries 2 and 3 indicate that HER could not occur if the Ru PS or light were excluded from the system, which proves that hydrogen evolution is dependent on the excitation of the photosensitizer by light absorption. Without a catalyst, the system yields a much lower H_2 evolution activity (16.2 µmol), confirming the critical role of Co-dca as a catalyst (entry 4). $Co(NO_3)_2$ was replaced with Co-dca to evaluate the role of dca group on the catalytic activity (entry 5). $Co(NO_3)_2$ evolves hydrogen with a significantly lower rate compared to Co-dca (22.7 µmol). The comparison of activities suggests that the activity of the cobalt site is enhanced when it is coordinated to dca ligands. Similar experiments were also conducted with TEOA as the sacrificial electron donor reagent (Figure 82b). While TEOA exhibits an identical profile to that of

TEA, the amount of produced hydrogen is lower in all cases, indicating that TEA is a more suitable sacrificial electron donor for the HER process.

TOF, which is defined as the number of evolved H_2 per active catalytic site per time, is also an essential indicator for comparing the activity of the catalyst. All the cobalt sites are presumed catalytically active for the estimation of the lower bound of TOF values. Co-dca evolves 25 µmol of hydrogen in the 1st h of the photocatalytic experiment, which corresponds to a TOF of 1.33×10^{-3} s^{-1}.

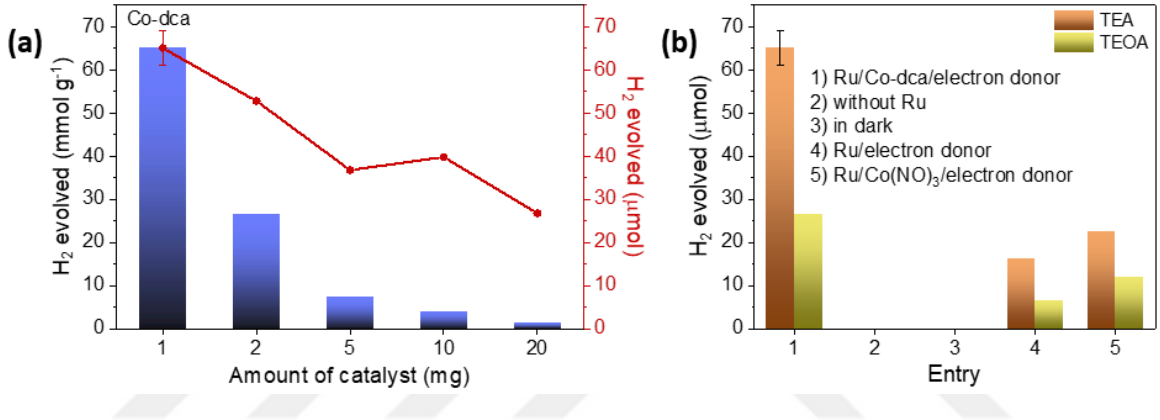

Figure 82. (a) The effect of the quantity of Co-dca on the H_2 evolution. (b) Rate of H_2 evolution with Co-dca, $[Ru(bpy)_3]^{2+}$, and electron donor (entry 1), without $[Ru(bpy)_3]^{2+}$ (entry 2), without light (entry 3), without Co-dca (entry 4), when Co-dca is replaced with $Co(NO_3)_2$ as the catalyst (entry 5). The reactions are performed in the presence of TEA (orange bars) and TEOA (yellow bars) as the electron donor. Reaction conditions: 1 mg of catalyst, 1 mM of $[Ru(bpy)_3](PF_6)_2$, 8 mL MeCN/H_2O (19/1, v/v), and 2 mL of sacrificial electron donor under visible light irradiation ($\lambda > 420$ nm) for 3 h.

Long-term HER measurement for Co-dca is displayed in Figure 83. The catalyst displays an enhanced hydrogen evolution activity in the first 3 h of the photocatalytic experiment. After this period, a decay in the hydrogen evolution was observed, which could be attributed to the decomposition of Ru PS or consumption of the sacrificial electron donor [167], [169], [242]. To elucidate the origin of the decay in the activity, first, an additional portion of Ru PS (1 mM) was added to the reaction solution (point 2). Then, after 1 h

irradiation, 2 mL fresh TEA was added at point 3. While recharging the solution only with Ru PS (8−9 h interval) restores 42% of activity, replenishing it with both Ru PS and TEA (9−10 h interval) regenerates 86% of activity. The similarity of photocatalytic performance after point 1 and point 3 suggests that the catalyst maintains its activity and stability during a 12 h experiment.

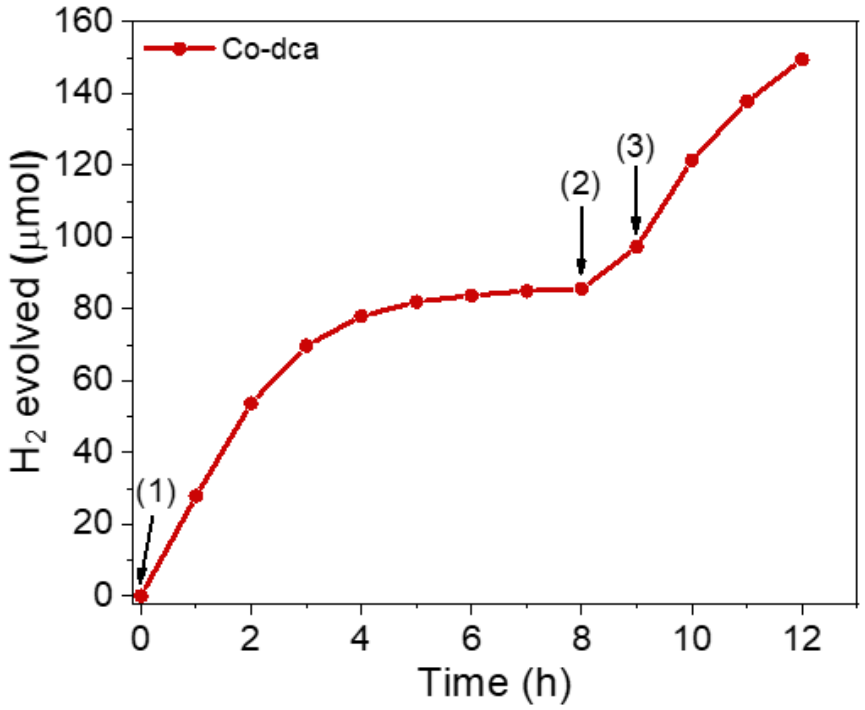

Figure 83. Long-term H_2 evolution rate for Co-dca under visible light under visible (λ > 420 nm) irradiation. (1) Starting conditions: 1 mg of catalyst, 8.6 mg of $[Ru(bpy)_3](PF_6)_2$ (1mM), 8 mL MeCN/H_2O (19/1, v/v), and 2 mL of TEA, (2) 8.6 mg of $[Ru(bpy)_3](PF_6)_2$ (1mM) added; (3) 2 mL of TEA added.

In addition to Co-dca, the catalytic performance of Co-dca/TEA was also studied under the same conditions. The activity of the Co-dca/TEA for photocatalytic H_2 production was similar to that of Co-dca, which maintains its activity at least for 2 consequence cycles (Figure 84a,b). Therefore, the catalytic activity of Co-dca after treatment with a MeCN/H_2O/TEA mixed solution is unaffected. TEM analysis was also used to track the morphological change of the cobalt dicyanamide. While Co-dca initially displays a 3D

coordination network (Figure 84c), it obviously transforms into a 2D layered structure at the end of 3 h of photocatalytic reaction (Figure 84d), which is analogous to Co-dca/TEA morphology (Figure 84e). These observations suggest that the presence of TEA causes a rapid transformation from 3D to 2D structure in Co-dca, which is the catalytically active species.

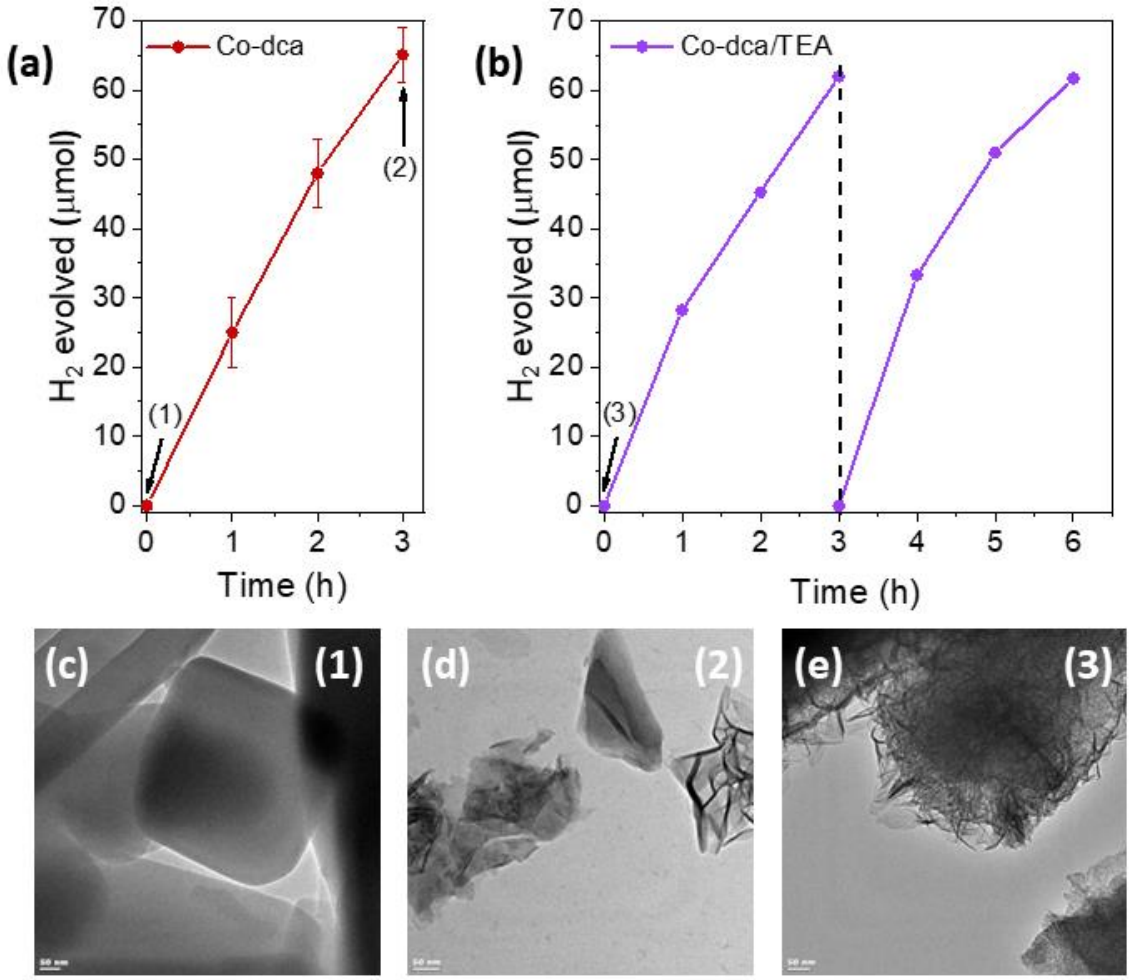

Figure 84. The time courses of hydrogen evolution for (a) Co-dca, and (b) Co-dca/TEA (for the second cycle catalyst was dispersed in a fresh solution containing Ru PS). Reaction conditions: 1 mg of catalyst, 1 mM of $[Ru(bpy)_3](PF_6)_2$, 8 mL MeCN/H_2O (19/1, v/v), and 2 mL of TEA under visible light irradiation ($\lambda > 420$ nm). TEM images of (c) as-synthesized Co-dca (point 1), (d) Co-dca at the end of 3 h photocatalytic experiment (point 2), and (e) Co-dca/TEA (point 3).

Figure 85 shows the H_2 evolution activity of all prepared catalysts, which is 65.1, 62, and 60 µmol after 3 h experiment for Co-dca, Co-dca/TEA, and Co-dca-TEA, respectively. Co-dca structure interacts with TEA in three distinct ways: i) only during the photocatalytic experiment as the electron donor, ii) treatment with TEA-containing solution for 20 h prior to the photocatalytic experiment (Co-dca/TEA), iii) in the synthesis procedure (Co-dca-TEA). These results reveal that the incorporation of TEA is essential for the transformation of C-dca to a more active species and that this transformation is rapid.

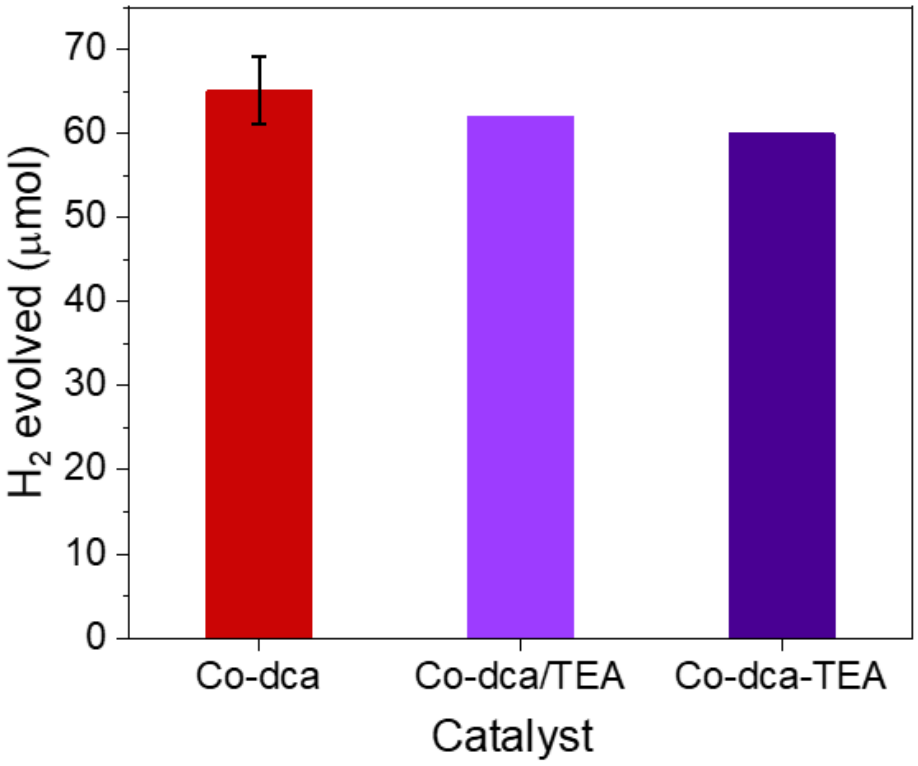

Figure 85. H_2 production data for Co-dca, Co-dca/TEA, and Co-dca-TEA. The reactions are performed using 1 mM $[Ru(bpy)_3](PF_6)_2$ and 1 mg of Co-dca under visible light irradiation for 3 h.

6.2.3 Post-catalytic Characterization of Co-dca

FTIR, XPS, and TEM methods were employed to analyze the chemical and morphological structures of the post-catalytic Co-dca sample. In FTIR spectra, it is shown that cyanide stretching modes shift to a lower wavenumber compared to the pristine sample

(Figure 86a-b). Moreover, XPS spectra display that the Co $2p_{3/2}$ and $2p_{1/2}$ peaks become narrower, and the spin−orbit splitting (ΔE = 15.7 eV) slightly decreases, indicating that Co^{2+} ions are partly oxidized to Co^{3+} during the photocatalytic experiment (Figure 86c). Note that infrared and XPS profiles of the post-catalytic Co-dca sample are similar to those of the Co-dca/TEA.

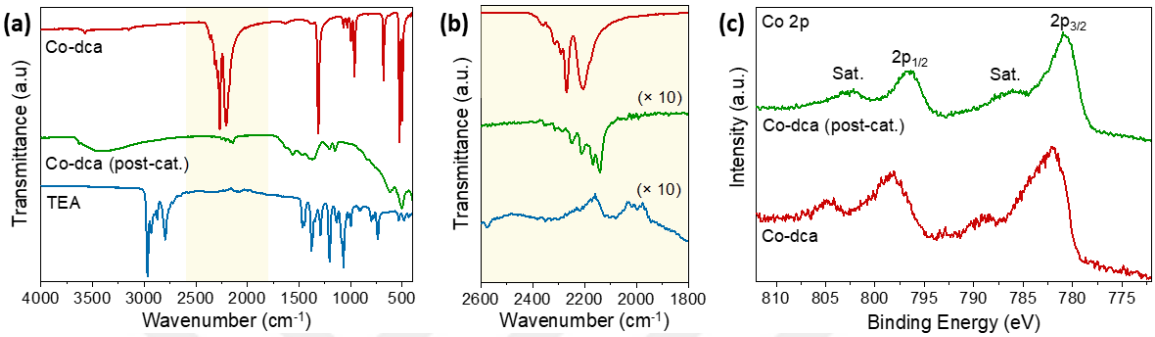

Figure 86. ATR-FTIR spectra of Co-dca, post-catalytic Co-dca, and TEA between (a) 400−4000 cm^{-1}, and (b) 1800-2600 cm^{-1}. (c) XPS Co 2p spectra of pristine and post-catalytic Co-dca.

6.2.4 Effect of Solution on Co-dca Structure

A dispersed solution Co-dca in various solvents was investigated with Infrared spectroscopy to explore the effect of solvent molecules on the transformation process of the catalyst. (Figure 87). The FTIR profile of Co-dca in bare MeCN or TEA is identical to the pristine sample, suggesting no change in the structure of Co-dca, despite the presence of MeCN or TEA. The cyanide stretching modes of the Co-dca spectra shift to lower wavenumbers when the compound is dispersed in MeCN/TEA or MeCN/H_2O/TEA, which suggests that the co-presence of MeCN and TEA is required for the structural transformation of Co-dca.

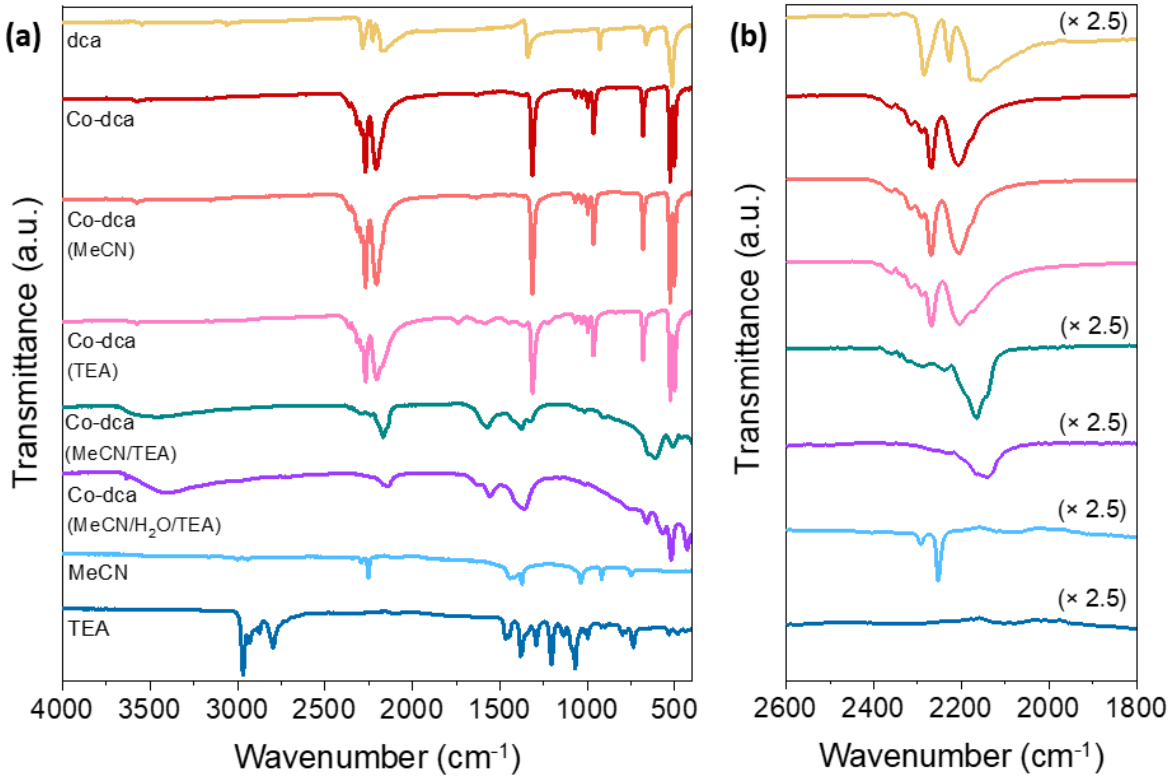

Figure 87. ATR-FTIR spectra of Co-dca dispersed in different solutions (a) 400−4000 cm^{-1}, and (b) 1800−2600 cm^{-1}.

6.3 Summary

The cobalt dicyanamide coordination network was prepared successfully with a precipitation method. Co-dca has significant photocatalytic activity as a hydrogen evolution catalyst, with activity as high as 25000 µmol h^{-1} g^{-1}. A long-term experiment indicates that Co-dca is stable for at least 12 h under photocatalytic conditions. Moreover, we changed the synthesis methodology and photocatalytic experiment conditions to obtain a combination of enhanced activity and durability. Three approaches were used to examine the role of TEA on the structure and photocatalytic activity of Co-dca: i) TEA was employed as the electron donor in the photocatalytic experiment, ii) for treatment of Co-dca before the photocatalytic experiment (Co-dca/TEA), iii) in the synthesis procedure (Co-dca-TEA). These results reveal that the presence of TEA is critical for superior HER

activity of Co-dca. Furthermore, the 3D network of Co-dca was transformed into 2D layered morphology when TEA was used.

Table 7. A comparison study between Co-dca and previously reported photocatalysts for HER.

Catalyst	**Photosensitizer**	**H_2 evolved (μmol h^{-1})**	**TOF (h^{-1})**	**Ref.**
$[Mo_3S_{13}]^{2-}$	$[Ru(bpy)_3]^{2-}$	380	335	[243]
$Co(dmgH)_2pyCl$	$[Ru(bpy)_3]^{2-}$	9.4	54	[166]
FeFe-H_2ase	$[Ru(bpy)_3]^{2-}$		10.8	[244]
CoGGH	$[Ru(bpy)_3]^{2-}$	1.6	62.9	[169]
$[Co_6L_8Cl_6(H_2O)_6]Cl_6$	$[Ru(bpy)_3]^{2-}$		16	[165]
Co-dca	$[Ru(bpy)_3]^{2-}$	25000	4.8	This work

Chapter 7

Conclusions

7.1 Summary and Outlook

Artificial photosynthesis can be realized by a colloidal photocatalytic system since it offers a simple, relatively low-cost, and easily scalable method to harvest solar light. These photocatalytic assemblies generally involve the coupling of a suitable light-harvesting component with a catalyst. However, the design of an efficient, durable, and cost-effective hybrid assembly imposes a challenge and is considered the bottleneck step for the development of a commercially feasible system for water splitting.

In this doctoral thesis, 2D semiconductors, ZnCr-LDH and niobate nanosheets, which are well-known layered materials, were modified with CoFe-PB as the water oxidation catalyst. 2D architecture semiconductors can reduce electron−hole recombination and shorten charge carrier traveling distance. Initially, ZnCr-LDH and CoFe-PB were combined with a facile synthetic method to develop an entirely earth-abundant SC−WOC assembly (LDH-PB) for the visible light-driven water oxidation process. By adjusting the atomic ratio of components, the photocatalytic activity of SC-WOC assembly was enhanced. Optical and electrochemical studies reveal that the HOMO level of PB structure is placed in a position, which can efficiently extract holes from LDH for water oxidation.

This efficient charge separation leads to a three-fold increase in photocatalytic activity compared to the bare LDH. Moreover, the PBA modification as a WOC enhances the stability of LDH under photocatalytic conditions. Furthermore, we observed that the activity and stability of LDH-PB assemblies could be improved by changing their weight ratio.

The exfoliation/restacking route is significantly beneficial for boosting the catalytic activity of layered materials due to the large surface area and high accessibility of reactant molecules, including water, to the reaction sites. Therefore, CoFe-PB was synthesized by exfoliation/restacking route on niobate nanosheet ($Ca_2Nb_3O_{10}^-$) to design another SC−WOC hybrid assembly (Niobate/PB) for the water oxidation process. The assembly creates an efficient p−n junction, resulting in a photocatalytic activity that is about 6.5 times greater than the pristine niobate sample, which maintains its activity for 12 h. The p−n junction feature not only improves the charge transfer between the niobate and PB components but also extends the activity of Niobate/PB in the visible region as well as the UV region. The high photocurrent response of Niobate/PB in the photoelectrochemical experiment compared to $KCa_2Nb_3O_{10}$ confirms a much faster migration and separation rate of photogenerated electrons and holes under UV−vis light illumination. Characterization studies on the post-catalytic sample suggest that the hybrid assembly retains its structural integrity.

Co-dca was used for the first time in this study as a catalyst for both HER and CO_2RR. A 3D Co-dca coordination compound was easily prepared by a precipitation method, in which the cobalt sites are coordinated by the nitrogen atoms of the dicyanamide ligands. The photocatalytic activity of Co-dca for both HER and CO_2RR was evaluated in the presence of a ruthenium-based PS and a sacrificial electron donor under visible light illumination. Several control experiments were performed to optimize the amount of

catalyst, Ru PS, and other photocatalytic conditions. Photocatalytic studies reveal that the CO_2-to-CO conversion rate and CO selectivity of Co-dca are 254 μmol h^{-1} g^{-1} (0.5 mM Ru PS) and 93% (0.1 mM Ru PS), respectively. Additionally, we found that the CO generation activity of Co-dca is about 3.5 times higher than that of CoFe-PB, which has recently been reported for photocatalytic CO_2RR. The formation of Co-TEOA during the photocatalytic experiment is evidenced by post-catalytic characterization, which is inactive toward CO_2 reduction. As a hydrogen evolution catalyst, Co-dca exhibits high photocatalytic activity of 25000 μmol h^{-1} g^{-1}, which is stable for at least 12 h. Moreover, we changed the synthesis methodology and photocatalytic experiment conditions to obtain a combination of enhanced activity and durability. These results reveal that the presence of TEA as the electron donor agent is critical for high activity. Moreover, the 3D network of Co-dca was transformed into 2D layered morphology during the photocatalytic experiment.

7.2 Future Work

ZnCr layered double hydroxide and niobate nanosheets as 2D semiconductors were successfully modified with CoFe-PB to design hybrid assemblies for the water oxidation process. On the other hand, nickel-based PBAs can be suitable candidates for HER. Therefore, the combination of these PBAs with appropriate 2D semiconductors, such as g-C_3N_4 with unique optical and electrical properties, should be investigated to determine whether it operates as an HER hybrid assembly or not. This might create new opportunities for the development of low-cost PBA-based hybrid structures with high activity for overall water splitting.

This study reveals that Co-dca is an active and robust catalyst for hydrogen production. The results are promising; however, the Ru PS needs to be replaced with other organic chromophores due to the high cost and poor long-term stability of ruthenium-based

photosensitizers. Eosin Y, which has been used as an organic dye in several HER studies, can be an ideal candidate to couple with Co-dca for the development of a PS−Cat dyad assembly or dye-sensitized photocatalyst for hydrogen evolution. Thus, the Co-dca-based noble metal-free hybrid systems should be further investigated and optimized.

7.3 List of Publications

Included in this Thesis

(1) **Akbari, S. S.**; Karadas, F. Selective Photocatalytic CO_2 Reduction by Cobalt Dicyanamide. ***Dalt. Trans.*** 2022, 51, 12569-12575.

(2) **Akbari, S. S.**; Unal, U.; Karadas, F. Photocatalytic Water Oxidation with a CoFe Prussian Blue Analogue–Layered Niobate Hybrid Material. ***ACS Appl. Energy Mater*.** 2021, 4, 12383–12390.

(3) **Akbari, S. S.**; Karadas, F. Precious Metal-Free Photocatalytic Water Oxidation by a Layered Double Hydroxide-Prussian Blue Analogue Hybrid Assembly. ***ChemSusChem*** **2021**, 14, 679–685.

Additional Publications

(4) Ülker, E.; **Akbari, S. S.**; Karadas, F. Cobalt Borophosphate on Nickel Foam as an Electrocatalyst for Water Splitting. ***Mater. Chem. Phys.*** **2022**, 288, 126390.

(5) Samuei, S.; **Sadigh Akbari, S**.; Ülker, E.; Karadas, F. Effect of Cobalt Doping on Photocatalytic Water Splitting Activity of NiTi-Layered Double Hydroxide. ***Catal. Sci. Technol.*** **2022**, 3044–3053.

(6) Andonova, S.; **Akbari, S. S.**; Karadas, F.; Spassova, I.; Paneva, D.; Hadjiivanov, K. Structure and Properties of KNi-Hexacyanoferrate Prussian Blue Analogues for

Efficient CO_2 capture: Host-Guest Interaction Chemistry and Dynamics of CO_2 adsorption. ***J. CO_2 Util.*** **2021**, 50, 101593.

(7) Gundogdu, G.; Ulusoy Ghobadi, T. G.; **Sadigh Akbari, S.**; Ozbay, E.; Karadas, F. Photocatalytic Water Oxidation with a Prussian Blue Modified Brown TiO_2. ***Chem. Commun.*** **2021**, 57, 508–511.

(8) Ulusoy Ghobadi, T. G.; Akhuseyin Yildiz, E.; Buyuktemiz, M.; **Sadigh Akbari, S.**; Topkaya, D.; İsci, Ü.; Dede, Y.; Yaglioglu, H. G.; Karadas, F. A Noble-Metal-Free Heterogeneous Photosensitizer-Relay-Catalyst Triad Catalyzes Water Oxidation under Visible Light. ***Angew. Chem. Int. Ed.*** **2018,** 57, 17173–17177.

Bibliography

[1] N. S. Lewis and D. G. Nocera, “Powering the planet: Chemical challenges in solar energy utilization,” *Proc. Natl. Acad. Sci. U. S. A.*, vol. 103, no. 43, pp. 15729–15735, 2006.

[2] L. Hammarström, “Artificial photosynthesis: Closing remarks,” *Faraday Discuss.*, vol. 198, pp. 549–560, 2017.

[3] T. Hisatomi, J. Kubota, and K. Domen, “Recent advances in semiconductors for photocatalytic and photoelectrochemical water splitting,” *Chem. Soc. Rev.*, vol. 43, no. 22, pp. 7520–7535, 2014.

[4] D. Gust, T. A. Moore, and A. L. Moore, “Solar fuels via artificial photosynthesis,” *Acc. Chem. Res.*, vol. 42, no. 12, pp. 1890–1898, 2009.

[5] B. Zhang and L. Sun, “Artificial photosynthesis: Opportunities and challenges of molecular catalysts,” *Chem. Soc. Rev.*, vol. 48, no. 7, pp. 2216–2264, 2019.

[6] T. Takata and K. Domen, “Particulate Photocatalysts for Water Splitting: Recent Advances and Future Prospects,” *ACS Energy Lett.*, vol. 4, no. 2, pp. 542–549, 2019.

[7] D. Luo, K. Nakata, A. Fujishima, and S. Liu, “Photochemistry and photo-electrochemistry on synthetic semiconducting diamond,” *J. Photochem. Photobiol. C Photochem. Rev.*, vol. 31, pp. 139–152, 2017.

[8] F. Li, H. Yang, W. Li, and L. Sun, “Device Fabrication for Water Oxidation, Hydrogen Generation, and CO_2 Reduction via Molecular Engineering,” *Joule*, vol. 2, no. 1, pp. 36–60, 2018.

[9] J. P. McEvoy and G. W. Brudvig, “Water-splitting chemistry of photosystem II,”

Chem. Rev., vol. 106, no. 11, pp. 4455–4483, 2006.

[10] T. Yao, X. An, H. Han, J. Q. Chen, and C. Li, "Photoelectrocatalytic Materials for Solar Water Splitting," *Adv. Energy Mater.*, vol. 8, no. 21, p. 1800210, 2018.

[11] S. Berardi *et al.*, "Molecular artificial photosynthesis," *Chem. Soc. Rev.*, vol. 43, no. 22, pp. 7501–7519, 2014.

[12] X. Liu, S. Inagaki, and J. Gong, "Heterogeneous Molecular Systems for Photocatalytic CO_2 Reduction with Water Oxidation," *Angew. Chem. Int. Ed.*, vol. 55, no. 48, pp. 14924–14950, 2016.

[13] Z. Wang, C. Li, and K. Domen, "Recent developments in heterogeneous photocatalysts for solar-driven overall water splitting," *Chem. Soc. Rev.*, vol. 48, no. 7, pp. 2109–2125, 2019.

[14] S. Chen, T. Takata, and K. Domen, "Particulate photocatalysts for overall water splitting," *Nat. Rev. Mater.*, vol. 2, no. 10, pp. 1–17, 2017.

[15] X. Chen, S. Shen, L. Guo, and S. S. Mao, "Semiconductor-based photocatalytic hydrogen generation," *Chem. Rev.*, vol. 110, no. 11, pp. 6503–6570, 2010.

[16] X. Zhang, T. Peng, and S. Song, "Recent advances in dye-sensitized semiconductor systems for photocatalytic hydrogen production," *J. Mater. Chem. A*, vol. 4, no. 7, pp. 2365–2402, 2016.

[17] P. X. Ding, H. Y. Zeng, S. Xu, C. R. Chen, J. Z. Du, and X. Cao, "Electrochemical behaviors of iron-based layered double hydroxide thin-films," *J. Mater. Sci. Mater. Electron.*, vol. 29, no. 4, pp. 2748–2757, 2018.

[18] T. Edvinsson, "Optical quantum confinement and photocatalytic properties in two-, one- and zero-dimensional nanostructures," *R. Soc. Open Sci.*, vol. 5, no. 9, p.

180387, 2018.

[19] Q. Wang and K. Domen, “Particulate Photocatalysts for Light-Driven Water Splitting: Mechanisms, Challenges, and Design Strategies,” *Chem. Rev.*, vol. 120, no. 2, pp. 919–985, 2019.

[20] K. E. Dalle, J. Warnan, J. J. Leung, B. Reuillard, I. S. Karmel, and E. Reisner, “Electro- and Solar-Driven Fuel Synthesis with First Row Transition Metal Complexes,” *Chem. Rev.*, vol. 119, no. 4, pp. 2752–2875, 2019.

[21] J. Ran, J. Zhang, J. Yu, M. Jaroniec, and S. Z. Qiao, “Earth-abundant cocatalysts for semiconductor-based photocatalytic water splitting,” *Chem. Soc. Rev.*, vol. 43, no. 22, pp. 7787–7812, 2014.

[22] D. M. Fabian *et al.*, “Particle suspension reactors and materials for solar-driven water splitting,” *Energy Environ. Sci.*, vol. 8, no. 10, pp. 2825–2850, 2015.

[23] S. Zhang, X. Yang, Y. Numata, and L. Han, “Highly efficient dye-sensitized solar cells: Progress and future challenges,” *Energy Environ. Sci.*, vol. 6, no. 6, pp. 1443–1464, 2013.

[24] P. Xu, N. S. McCool, and T. E. Mallouk, “Water splitting dye-sensitized solar cells,” *Nano Today*, vol. 14, pp. 42–58, 2017.

[25] J. Willkomm, K. L. Orchard, A. Reynal, E. Pastor, J. R. Durrant, and E. Reisner, “Dye-sensitised semiconductors modified with molecular catalysts for light-driven H_2 production.,” *Chem. Soc. Rev.*, vol. 45, no. 1, pp. 9–23, 2016.

[26] D. L. Ashford *et al.*, “Molecular Chromophore-Catalyst Assemblies for Solar Fuel Applications,” *Chem. Rev.*, vol. 115, no. 23, pp. 13006–13049, 2015.

[27] P. D. Frischmann, K. Mahata, and F. Würthner, “Powering the future of molecular

artificial photosynthesis with light-harvesting metallosupramolecular dye assemblies," *Chem. Soc. Rev.*, vol. 42, no. 4, pp. 1847–1870, 2013.

[28] H. D. Gafney and A. W. Adamson, "Excited state $Ru(bipyr)_3^{2+}$ as an electron-transfer reductant," *J. Am. Chem. Soc.*, vol. 94, no. 23, pp. 8238–8239, 1972.

[29] E. S. Andreiadis, M. Chavarot-Kerlidou, M. Fontecave, and V. Artero, "Artificial photosynthesis: From molecular catalysts for light-driven water splitting to photoelectrochemical cells," *Photochem. Photobiol.*, vol. 87, no. 5, pp. 946–964, 2011.

[30] C. Creutz and N. Sutin, "Reaction of tris(bipyridine)ruthenium(III) with hydroxide and its application in a solar energy storage system," *Proc. Natl. Acad. Sci.*, vol. 72, no. 8, pp. 2858–2862, 1975.

[31] M. Wang, Y. Na, M. Gorlov, and L. Sun, "Light-driven hydrogen production catalysed by transition metal complexes in homogeneous systems," *Dalt. Trans.*, vol. 33, pp. 6458–6467, 2009.

[32] S. J. A. Moniz, S. A. Shevlin, D. J. Martin, Z. X. Guo, and J. Tang, "Visible-light driven heterojunction photocatalysts for water splitting-a critical review," *Energy Environ. Sci.*, vol. 8, no. 3, pp. 731–759, 2015.

[33] S. Bera, D. Il Won, S. B. Rawal, H. J. Kang, and W. I. Lee, "Design of visible-light photocatalysts by coupling of inorganic semiconductors," *Catal. Today*, vol. 335, pp. 3–19, 2018.

[34] Y. K. Jo, J. M. Lee, S. Son, and S. J. Hwang, "2D inorganic nanosheet-based hybrid photocatalysts: Design, applications, and perspectives," *J. Photochem. Photobiol. C Photochem. Rev.*, vol. 40, pp. 150–190, 2018.

[35] T. Su, Q. Shao, Z. Qin, Z. Guo, and Z. Wu, “Role of Interfaces in Two-Dimensional Photocatalyst for Water Splitting,” *ACS Catal.*, vol. 8, no. 3, pp. 2253–2276, 2018.

[36] S. Ida and T. Ishihara, “Recent progress in two-dimensional oxide photocatalysts for water splitting,” *J. Phys. Chem. Lett.*, vol. 5, no. 15, pp. 2533–2542, 2014.

[37] J. Di, C. Yan, A. D. Handoko, Z. W. Seh, H. Li, and Z. Liu, “Ultrathin two-dimensional materials for photo- and electrocatalytic hydrogen evolution,” *Mater. Today*, vol. 21, no. 7, pp. 749–770, 2018.

[38] P. Ganguly *et al.*, “2D Nanomaterials for Photocatalytic Hydrogen Production,” *ACS Energy Lett.*, vol. 4, no. 7, pp. 1687–1709, 2019.

[39] J. Di, J. Xiong, H. Li, and Z. Liu, “Ultrathin 2D Photocatalysts: Electronic-Structure Tailoring, Hybridization, and Applications,” *Advanced Materials*, vol. 30, no. 1. p. 1704548, 2018.

[40] K. Maeda and T. E. Mallouk, “Two-dimensional metal oxide nanosheets as building blocks for artificial photosynthetic assemblies,” *Bull. Chem. Soc. Jpn.*, vol. 92, no. 1, pp. 38–54, 2019.

[41] E. M. Sproviero, J. A. Gascón, J. P. McEvoy, G. W. Brudvig, and V. S. Batista, “Quantum mechanics/molecular mechanics study of the catalytic cycle of water splitting in photosystem II,” *J. Am. Chem. Soc.*, vol. 130, no. 11, pp. 3428–3442, 2008.

[42] M. D. Kärkäs, O. Verho, E. V. Johnston, and B. Åkermark, “Artificial photosynthesis: Molecular systems for catalytic water oxidation,” *Chem. Rev.*, vol. 114, no. 24, pp. 11863–12001, 2014.

[43] S. J. A. Moniz, S. A. Shevlin, D. J. Martin, Z. X. Guo, and J. Tang, “Visible-light

driven heterojunction photocatalysts for water splitting – a critical review," *Energy Environ. Sci.*, vol. 8, pp. 731–739, 2015.

[44] J. L. Inglis, B. J. MacLean, M. T. Pryce, and J. G. Vos, "Electrocatalytic pathways towards sustainable fuel production from water and CO_2," *Coord. Chem. Rev.*, vol. 256, no. 21–22, pp. 2571–2600, 2012.

[45] T. Zheng, K. Jiang, and H. Wang, "Recent Advances in Electrochemical CO_2-to-CO Conversion on Heterogeneous Catalysts," *Adv. Mater.*, vol. 30, no. 48, pp. 1–15, 2018.

[46] R. Kortlever, J. Shen, K. J. P. Schouten, F. Calle-Vallejo, and M. T. M. Koper, "Catalysts and Reaction Pathways for the Electrochemical Reduction of Carbon Dioxide," *J. Phys. Chem. Lett.*, vol. 6, no. 20, pp. 4073–4082, 2015.

[47] J. Wu, Y. Huang, W. Ye, and Y. Li, "CO_2 Reduction: From the Electrochemical to Photochemical Approach," *Adv. Sci.*, vol. 4, no. 11, p. 1700194, 2017.

[48] E. Fujita, "Photochemical carbon dioxide reduction with metal complexes," *Coord. Chem. Rev.*, vol. 185–186, pp. 373–384, 1999.

[49] Y. Yamazaki, H. Takeda, and O. Ishitani, "Photocatalytic reduction of CO_2 using metal complexes," *J. Photochem. Photobiol. C*, vol. 25, no. 4, pp. 106–137, 2015.

[50] H. Takeda and O. Ishitani, "Development of efficient photocatalytic systems for CO_2 reduction using mononuclear and multinuclear metal complexes based on mechanistic studies," *Coord. Chem. Rev.*, vol. 254, no. 3–4, pp. 346–354, 2010.

[51] Y. Kuramochi, O. Ishitani, and H. Ishida, "Reaction mechanisms of catalytic photochemical CO_2 reduction using Re(I) and Ru(II) complexes," *Coord. Chem. Rev.*, vol. 373, pp. 333–356, 2018.

[52] Y. Tamaki and O. Ishitani, "Supramolecular Photocatalysts for the Reduction of CO_2," *ACS Catal.*, vol. 7, no. 5, pp. 3394–3409, 2017.

[53] J. Grodkowski *et al.*, "Reduction of cobalt and iron phthalocyanines and the role of the reduced species in catalyzed photoreduction of CO_2," *J. Phys. Chem. A*, vol. 104, no. 48, pp. 11332–11339, 2000.

[54] S. Roy and E. Reisner, "Visible-Light-Driven CO_2 Reduction by Mesoporous Carbon Nitride Modified with Polymeric Cobalt Phthalocyanine," *Angew. Chem. Int. Ed.*, vol. 58, pp. 12180–12184, 2019.

[55] S. Wang, W. Yao, J. Lin, Z. Ding, and X. Wang, "Cobalt Imidazolate Metal-Organic Frameworks Photosplit CO_2 under Mild Reaction Conditions," *Angew. Chem. Int. Ed.*, vol. 53, pp. 1034–1038, 2014.

[56] Z. Y. Du *et al.*, "Polyoxometalate-induced 'cage-within-cage' metal-organic frameworks with high efficiency towards CO_2 photoreduction," *Sustain. Energy Fuels*, vol. 5, no. 15, pp. 3876–3883, 2021.

[57] X. Deng, Y. Qin, M. Hao, and Z. Li, "MOF-253-Supported Ru Complex for Photocatalytic CO_2 Reduction by Coupling with Semidehydrogenation of 1,2,3,4-Tetrahydroisoquinoline (THIQ)," *Inorg. Chem.*, vol. 58, no. 24, pp. 16574–16580, 2019.

[58] X. K. Wang *et al.*, "Monometallic Catalytic Models Hosted in Stable Metal-Organic Frameworks for Tunable CO_2 Photoreduction," *ACS Catal.*, vol. 9, no. 3, pp. 1726–1732, 2019.

[59] S. Wang, Y. Hou, and X. Wang, "Development of a stable $MnCo_2O_4$ cocatalyst for photocatalytic CO_2 reduction with visible light," *ACS Appl. Mater. Interfaces*, vol.

7, no. 7, pp. 4327–4335, 2015.

[60] C. Gao *et al.*, "Co_3O_4 Hexagonal Platelets with Controllable Facets Enabling Highly Efficient Visible-Light Photocatalytic Reduction of CO_2," *Adv. Mater.*, vol. 28, no. 30, pp. 6485–6490, 2016.

[61] S. Bai, Z. Wang, L. Tan, G. I. N. Waterhouse, Y. Zhao, and Y. F. Song, "600 nm Irradiation-Induced Efficient Photocatalytic CO_2 Reduction by Ultrathin Layered Double Hydroxide Nanosheets," *Ind. Eng. Chem. Res.*, vol. 59, no. 13, pp. 5848–5857, 2020.

[62] L. Tan *et al.*, "Highly Selective Photoreduction of CO_2 with Suppressing H_2 Evolution over Monolayer Layered Double Hydroxide under Irradiation above 600 nm," *Angew. Chem. Int. Ed.*, vol. 58, pp. 11860–11867, 2019.

[63] X. Meng *et al.*, "Light-Driven CO_2 Reduction over Prussian Blue Analogues as Heterogeneous Catalysts," *ACS Catal.*, vol. 12, pp. 89–100, 2022.

[64] Y. Liu and C. C. L. McCrory, "Modulating the mechanism of electrocatalytic CO_2 reduction by cobalt phthalocyanine through polymer coordination and encapsulation," *Nat. Commun.*, vol. 10, no. 1, pp. 1–10, 2019.

[65] T. Abe *et al.*, "Electrochemical CO_2 Reduction Catalysed by Cobalt Octacyanophthalocyanine and its Mechanism," *J. Porphyr. Phthalocyanines*, vol. 1, no. 4, pp. 315–321, 1997.

[66] S. Dutta, "Review on Solar Hydrogen: Its Prospects and Limitations," *Energy and Fuels*, vol. 35, no. 15, pp. 11613–11639, 2021.

[67] T. Hisatomi and K. Domen, "Reaction systems for solar hydrogen production via water splitting with particulate semiconductor photocatalysts," *Nat. Catal.*, vol. 2,

no. 5, pp. 387–399, 2019.

[68] Y. J. Yuan, Z. T. Yu, D. Q. Chen, and Z. G. Zou, "Metal-complex chromophores for solar hydrogen generation," *Chem. Soc. Rev.*, vol. 46, no. 3, pp. 603–631, 2017.

[69] Z. Hu, Z. Shen, and J. C. Yu, "Phosphorus containing materials for photocatalytic hydrogen evolution," *Green Chem.*, vol. 19, no. 3, pp. 588–613, 2017.

[70] L. Z. Wu, B. Chen, Z. J. Li, and C. H. Tung, "Enhancement of the efficiency of photocatalytic reduction of protons to hydrogen via molecular assembly," *Acc. Chem. Res.*, vol. 47, no. 7, pp. 2177–2185, 2014.

[71] M. Bowker, "Sustainable hydrogen production by the application of ambient temperature photocatalysis," *Green Chem.*, vol. 13, no. 9, pp. 2235–2246, 2011.

[72] A. Fujishima and K. Honda, "Electrochemical photolysis of water at a semiconductor electrode," *Nature*, vol. 238, no. 5358, pp. 37–38, 1972.

[73] W. Zhang, J. Hong, J. Zheng, Z. Huang, and R. Xu, "Nickel−Thiolate Complex Catalyst Assembled in One Step in Water for Solar H_2 Production," *J. Am. Chem. Soc.*, vol. 133, pp. 20680–20683, 2011.

[74] T. Lazarides, T. McCormick, P. Du, G. Luo, B. Lindley, and R. Eisenberg, "Making hydrogen from water using a homogeneous system without noble metals," *J. Am. Chem. Soc.*, vol. 131, no. 26, pp. 9192–9194, 2009.

[75] Y. Li, T. Yu, Y. Zeng, J. Chen, Y. Y. Li, and G. Yang, "Exceptional dendrimer-based mimics of diiron hydrogenase for the photochemical production of hydrogen," *Angew. Chem. Int. Ed.*, vol. 52, no. 21, pp. 5631–5635, 2013.

[76] R. Gueret *et al.*, "Cobalt(II) Pentaaza-Macrocyclic Schiff Base Complex as Catalyst for Light-Driven Hydrogen Evolution in Water: Electrochemical Generation and

Theoretical Investigation of the One-Electron Reduced Species," *Inorg. Chem.*, vol. 58, no. 14, pp. 9043–9056, 2019.

[77] M. Rupp *et al.*, "Photocatalytic Hydrogen Evolution Driven by a Heteroleptic Ruthenium(II) Bis(terpyridine) Complex," *Inorg. Chem.*, vol. 58, no. 14, pp. 9127–9134, 2019.

[78] K. Sakai and H. Ozawa, "Homogeneous catalysis of platinum(II) complexes in photochemical hydrogen production from water," *Coord. Chem. Rev.*, vol. 251, no. 21–24, pp. 2753–2766, 2007.

[79] E. Bae and W. Choi, "Effect of the anchoring group (carboxylate vs phosphonate) in Ru-complex-sensitized TiO_2 on hydrogen production under visible light," *J. Phys. Chem. B*, vol. 110, no. 30, pp. 14792–14799, 2006.

[80] A. Fihri, V. Artero, M. Razavet, C. Baffert, W. Leibl, and M. Fontecave, "Cobaloxime-based photocatalytic devices for hydrogen production," *Angew. Chem. Int. Ed.*, vol. 47, no. 3, pp. 564–567, 2008.

[81] J. Wang, H. Zhang, and X. Wang, "Recent Methods for the Synthesis of Noble-Metal-Free Hydrogen-Evolution Electrocatalysts: From Nanoscale to Sub-nanoscale," *Small Methods*, vol. 1, no. 6, p. 1700118, 2017.

[82] D. Aguilà, Y. Prado, E. S. Koumousi, C. Mathonière, and R. Clérac, "Switchable Fe/Co Prussian blue networks and molecular analogues," *Chem. Soc. Rev.*, vol. 45, no. 1, pp. 203–224, 2016.

[83] J. M. Herrera *et al.*, "Mixed valency and magnetism in cyanometallates and Prussian blue analogues," *Philos. Trans. R. Soc. A Math. Phys. Eng. Sci.*, vol. 366, no. 1862, pp. 127–138, 2008.

[84] T. G. Ulusoy Ghobadi, E. Ozbay, and F. Karadas, “How to Build Prussian Blue Based Water Oxidation Catalytic Assemblies: Common Trends and Strategies,” *Chem. Eur. J.*, vol. 27, no. 11, pp. 3638–3649, 2021.

[85] S. Goberna-Ferron, W. Y. Hernandez, B. Rodriguez-Garcia, and J. R. Galan-Mascaros, “Light-driven water oxidation with metal hexacyanometallate heterogeneous catalysts,” *ACS Catal.*, vol. 4, no. 6, pp. 1637–1641, 2014.

[86] L. Han *et al.*, “Enhanced Activity and Acid pH Stability of Prussian Blue-type Oxygen Evolution Electrocatalysts Processed by Chemical Etching,” *J. Am. Chem. Soc.*, vol. 138, no. 49, pp. 16037–16045, 2016.

[87] Z. Kap and F. Karadas, “Visible light-driven water oxidation with a ruthenium sensitizer and a cobalt-based catalyst connected with a polymeric platform,” *Faraday Discuss.*, vol. 215, pp. 111–122, 2019.

[88] T. G. Ulusoy Ghobadi *et al.*, “A Noble-Metal-Free Heterogeneous Photosensitizer-Relay-Catalyst Triad Catalyzes Water Oxidation under Visible Light,” *Angew. Chem. Int. Ed.*, vol. 57, pp. 17173–17177, 2018.

[89] F. S. Hegner, I. Herraiz-Cardona, D. Cardenas-Morcoso, N. López, J. R. Galán-Mascarós, and S. Gimenez, “Cobalt Hexacyanoferrate on $BiVO_4$ Photoanodes for Robust Water Splitting,” *ACS Appl. Mater. Interfaces*, vol. 9, no. 43, pp. 37671–37681, 2017.

[90] F. S. Hegner, D. Cardenas-Morcoso, S. Giménez, N. López, and J. R. Galan-Mascaros, “Level Alignment as Descriptor for Semiconductor/Catalyst Systems in Water Splitting: The Case of Hematite/Cobalt Hexacyanoferrate Photoanodes,” *ChemSusChem*, vol. 10, no. 22, pp. 4552–4560, 2017.

[91] J. Yu, Q. Wang, and D. O'Hare, "Preparation of two dimensional layered double hydroxide nanosheets and their applications," *Chem. Soc. Rev.*, vol. 46, pp. 5950–5974, 2017.

[92] G. Fan, F. Li, D. G. Evans, and X. Duan, "Catalytic applications of layered double hydroxides: recent advances and perspectives," *Chem. Soc. Rev.*, vol. 43, no. 20, pp. 7040–7066, 2014.

[93] S. He, Z. An, M. Wei, D. G. Evans, and X. Duan, "Layered double hydroxide-based catalysts: nanostructure design and catalytic performance," *Chem. Commun.*, vol. 49, no. 53, p. 5912, 2013.

[94] M. Xu and M. Wei, "Layered Double Hydroxide-Based Catalysts: Recent Advances in Preparation, Structure, and Applications," *Adv. Funct. Mater.*, vol. 28, no. 47, p. 1802943, 2018.

[95] Q. Wang and D. O'Hare, "Recent advances in the synthesis and application of layered double hydroxide (LDH) nanosheets," *Chem. Rev.*, vol. 112, no. 7, pp. 4124–4155, 2012.

[96] Y. Wang, D. Yan, S. El Hankari, Y. Zou, and S. Wang, "Recent Progress on Layered Double Hydroxides and Their Derivatives for Electrocatalytic Water Splitting," *Adv. Sci.*, vol. 5, no. 8, 2018.

[97] J. W. L. and J. K. K. Yeob Lee, Jung Hoon Choi, Hyung Joon Jeon, Kyung Min Choi, "Titanium-embedded layered double hydroxides as highly efficient water oxidation photocatalysts under visible light," *Energy Environ. Sci.*, vol. 4, pp. 914–920, 2011.

[98] D. S. Su *et al.*, "Highly Dispersed TiO_6 Units in a Layered Double Hydroxide for

Water Splitting," *Chem. - A Eur. J.*, vol. 18, no. 38, pp. 11949–11958, 2012.

[99] Y. Zhao *et al.*, "NiTi-Layered double hydroxides nanosheets as efficient photocatalysts for oxygen evolution from water using visible light," *Chem. Sci.*, vol. 5, no. 3, pp. 951–958, 2014.

[100] H. Zhou, Y. Song, Y. Liu, H. Li, W. Li, and Z. Chang, "Fabrication of CdS/Ni–Fe LDH heterostructure for improved photocatalytic hydrogen evolution from aqueous methanol solution," *Int. J. Hydrogen Energy*, vol. 43, no. 31, pp. 14328–14336, 2018.

[101] S. Nayak and K. M. Parida, "Nanostructured CeO_2/MgAl-LDH composite for visible light induced water reduction reaction," *Int. J. Hydrogen Energy*, vol. 41, no. 46, pp. 21166–21180, 2016.

[102] A. R. Amani-Ghadim, F. Khodam, and M. S. Seyed Dorraji, "ZnS quantum dot intercalated layered double hydroxide semiconductors for solar water splitting and organic pollutant degradation," *J. Mater. Chem. A*, vol. 7, no. 18, pp. 11408–11422, 2019.

[103] Y. Dou *et al.*, "TiO_2@layered double hydroxide core-shell nanospheres with largely enhanced photocatalytic activity toward O_2 generation," *Adv. Funct. Mater.*, vol. 25, no. 15, pp. 2243–2249, 2015.

[104] S. M. Xu, H. Yan, and M. Wei, "Band Structure Engineering of Transition-Metal-Based Layered Double Hydroxides toward Photocatalytic Oxygen Evolution from Water: A Theoretical-Experimental Combination Study," *J. Phys. Chem. C*, vol. 121, no. 5, pp. 2683–2695, 2017.

[105] J. Zou, Z. Wang, W. Guo, B. Guo, Y. Yu, and L. Wu, "Photocatalytic selective

oxidation of benzyl alcohol over ZnTi-LDH: The effect of surface OH groups," *Appl. Catal. B Environ.*, vol. 260, p. 118185, 2020.

[106] B. Ou, J. Wang, Y. Wu, S. Zhao, and Z. Wang, "Efficient removal of Cr(VI) by magnetic and recyclable calcined CoFe-LDH/g-C_3N_4 via the synergy of adsorption and photocatalysis under visible light," *Chem. Eng. J.*, vol. 380, p. 122600, 2020.

[107] Y. Zhao *et al.*, "Layered Double Hydroxide Nanostructured Photocatalysts for Renewable Energy Production," *Adv. Energy Mater.*, vol. 6, no. 6, p. 1501974, 2016.

[108] L. Lv, Z. Yang, K. Chen, C. Wang, and Y. Xiong, "2D Layered Double Hydroxides for Oxygen Evolution Reaction: From Fundamental Design to Application," *Adv. Energy Mater.*, vol. 9, no. 17, p. 1803358, 2019.

[109] J. L. Gunjakar, T. W. Kim, H. N. Kim, I. Y. Kim, and S. J. Hwang, "Mesoporous layer-by-layer ordered nanohybrids of layered double hydroxide and layered metal oxide: Highly active visible light photocatalysts with improved chemical stability," *J. Am. Chem. Soc.*, vol. 133, no. 38, pp. 14998–15007, 2011.

[110] C. G. Silva, Y. Bouizi, V. Fornés, and H. García, "Layered double hydroxides as highly efficient photocatalysts for visible light oxygen generation from water," *J. Am. Chem. Soc.*, vol. 131, no. 38, pp. 13833–13839, 2009.

[111] K. Parida and L. Mohapatra, "Recent progress in the development of carbonate-intercalated Zn/Cr LDH as a novel photocatalyst for hydrogen evolution aimed at the utilization of solar light," *Dalt. Trans.*, vol. 41, no. 4, pp. 1173–1178, 2012.

[112] Y. Fu, F. Ning, S. Xu, H. An, M. Shao, and M. Wei, "Terbium doped ZnCr-layered double hydroxides with largely enhanced visible light photocatalytic performance," *J. Mater. Chem. A*, vol. 4, no. 10, pp. 3907–3913, 2016.

[113] D. P. Sahoo, S. Nayak, K. H. Reddy, S. Martha, and K. Parida, "Fabrication of a $Co(OH)_2$/ZnCr LDH 'p-n' heterojunction photocatalyst with enhanced separation of charge carriers for efficient visible-light-driven H_2 and O_2 evolution," *Inorg. Chem.*, vol. 57, no. 7, pp. 3840–3854, 2018.

[114] C. Wang *et al.*, "Visible-light-driven overall water splitting with a largely-enhanced efficiency over a Cu_2O@ZnCr-layered double hydroxide photocatalyst," *Nano Energy*, vol. 32, pp. 463–469, 2017.

[115] D. P. Sahoo, S. Patnaik, and K. Parida, "Construction of a Z-Scheme Dictated WO_{3-x}/Ag/ZnCr LDH Synergistically Visible Light-Induced Photocatalyst towards Tetracycline Degradation and H_2 Evolution," *ACS Omega*, vol. 4, no. 12, pp. 14721–14741, 2019.

[116] J. L. Gunjakar, I. Y. Kim, J. M. Lee, N. S. Lee, and S. J. Hwang, "Self-assembly of layered double hydroxide 2D nanoplates with graphene nanosheets: An effective way to improve the photocatalytic activity of 2D nanostructured materials for visible light-induced O_2 generation," *Energy Environ. Sci.*, vol. 6, no. 3, pp. 1008–1017, 2013.

[117] J. L. Gunjakar, T. W. Kim, I. Y. Kim, J. M. Lee, and S. J. Hwang, "Highly efficient visible light-induced O_2 generation by self-Assembled nanohybrids of inorganic nanosheets and polyoxometalate nanoclusters," *Sci. Rep.*, vol. 3, pp. 1–8, 2013.

[118] G. Zhang, B. Lin, Y. Qiu, L. He, Y. Chen, and B. Gao, "Highly efficient visible-light-driven photocatalytic hydrogen generation by immobilizing CdSe nanocrystals on ZnCr-layered double hydroxide nanosheets," *Int. J. Hydrogen Energy*, vol. 40, no. 14, pp. 4758–4765, 2015.

[119] M. Sohail, H. Kim, and T. W. Kim, "Enhanced photocatalytic performance of a Ti-

based metal-organic framework for hydrogen production: Hybridization with ZnCr-LDH nanosheets," *Sci. Rep.*, vol. 9, no. 1, pp. 1–11, 2019.

[120] T. G. Ulusoy Ghobadi *et al.*, "A Robust, Precious-Metal-Free Dye-Sensitized Photoanode for Water Oxidation: A Nanosecond-Long Excited-State Lifetime through a Prussian Blue Analogue," *Angew. Chem. Int. Ed.*, vol. 59, no. 10, pp. 4082–4090, 2020.

[121] M. Aksoy, S. V. K. Nune, and F. Karadas, "A Novel Synthetic Route for the Preparation of an Amorphous Co/Fe Prussian Blue Coordination Compound with High Electrocatalytic Water Oxidation Activity," *Inorg. Chem.*, vol. 55, no. 9, pp. 4301–4307, 2016.

[122] T. G. Ulusoy Ghobadi *et al.*, "Strong Light-matter Interaction in Au Plasmonic Nanoantennas Coupled with Prussian Blue Catalyst on $BiVO_4$ for Photoelectrochemical Water Splitting," *ChemSusChem*, vol. 13, pp. 2577–2588, 2020.

[123] M. A. Bizeto, A. L. Shiguihara, and V. R. L. Constantino, "Layered niobate nanosheets: building blocks for advanced materials assembly," *J. Mater. Chem.*, vol. 19, no. 17, pp. 2512–2525, 2009.

[124] A. Kumar, A. Kumar, and V. Krishnan, "Perovskite Oxide Based Materials for Energy and Environment-Oriented Photocatalysis," *ACS Catal.*, vol. 10, no. 17, pp. 10253–10315, 2020.

[125] Y. Okamoto, S. Ida, J. Hyodo, H. Hagiwara, and T. Ishihara, "Synthesis and photocatalytic activity of rhodium-doped calcium niobate nanosheets for hydrogen production from a water/methanol system without cocatalyst loading," *J. Am. Chem. Soc.*, vol. 133, no. 45, pp. 18034–18037, 2011.

[126] M. R. Karim *et al.*, "Electrical conductivity and ferromagnetism in a reduced graphene-metal oxide hybrid," *Adv. Funct. Mater.*, vol. 23, no. 3, pp. 323–332, 2013.

[127] N. N. Rabin *et al.*, "Super Dielectric Materials of Two-Dimensional TiO_2 or $Ca_2Nb_3O_{10}$ Nanosheet Hybrids with Reduced Graphene Oxide," *ACS Omega*, vol. 3, no. 2, pp. 2074–2083, 2018.

[128] F. E. Sarac, C. Yilmaz, F. Y. Acar, and U. Unal, "CdTe quantum dot sensitized hexaniobate nanoscrolls and their photoelectrochemical properties," *RSC Adv.*, vol. 2, no. 27, pp. 10182–10184, 2012.

[129] N. D. Morris and T. E. Mallouk, "A high-throughput optical screening method for the optimization of colloidal water oxidation catalysts.," *J. Am. Chem. Soc.*, vol. 124, no. 37, pp. 11114–11121, 2002.

[130] M. Hara, C. C. Waraksa, J. T. Lean, B. A. Lewis, and T. E. Mallouk, "Photocatalytic Water Oxidation in a Buffered Tris(2,2'-bipyridyl)ruthenium Complex-Colloidal IrO_2 System," *J. Phys. Chem. A*, vol. 104, no. 22, pp. 5275–5280, 2000.

[131] Y. Ebina, N. Sakai, and T. Sasaki, "Photocatalyst of lamellar aggregates of RuOx-loaded perovskite nanosheets for overall water splitting.," *J. Phys. Chem. B*, vol. 109, no. 36, pp. 17212–17216, 2005.

[132] W. J. Youngblood, S.-H. A. Lee, K. Maeda, and T. E. Mallouk, "Visible light water splitting using dye-sensitized oxide semiconductors.," *Acc. Chem. Res.*, vol. 42, no. 12, pp. 1966–1973, 2009.

[133] T. Oshima, O. Ishitani, and K. Maeda, "Non-Sacrificial Water Photo-Oxidation Activity of Lamellar Calcium Niobate Induced by Exfoliation," *Adv. Mater. Interfaces*, vol. 1, no. 7, p. 1400131, 2014.

[134] T. Oshima, D. Lu, O. Ishitani, and K. Maeda, “Intercalation of highly dispersed metal nanoclusters into a layered metal oxide for photocatalytic overall water splitting,” *Angew. Chem. Int. Ed.*, vol. 54, no. 9, pp. 2698–2702, 2015.

[135] T. Oshima, Y. Wang, D. Lu, T. Yokoi, and K. Maeda, “Photocatalytic overall water splitting on Pt nanocluster-intercalated, restacked $KCa_2Nb_3O_{10}$ nanosheets: The promotional effect of co-existing ions,” *Nanoscale Adv.*, vol. 1, no. 1, pp. 189–194, 2019.

[136] K. Maeda, M. Eguchi, S. H. A. Lee, W. J. Youngblood, H. Hata, and T. E. Mallouk, “Photocatalytic hydrogen evolution from Hexaniobate nanoscrolls and calcium niobate nanosheets sensitized by ruthenium(II) bipyridyl complexes,” *J. Phys. Chem. C*, vol. 113, no. 18, pp. 7962–7969, 2009.

[137] K. Maeda, M. Eguchi, and T. Oshima, “Perovskite Oxide Nanosheets with Tunable Band-Edge Potentials and High Photocatalytic Hydrogen-Evolution Activity,” *Angew. Chem. Int. Ed.*, vol. 53, no. 48, pp. 13164–13168, 2014.

[138] T. Oshima, M. Eguchi, and K. Maeda, “Photocatalytic Water Oxidation over Metal Oxide Nanosheets Having a Three-Layer Perovskite Structure,” *ChemSusChem*, vol. 9, no. 4, pp. 396–402, 2016.

[139] T. Oshima, O. Ishitani, and K. Maeda, “Non-sacrificial water photo-oxidation activity of lamellar calcium niobate induced by exfoliation,” *Adv. Mater. Interfaces*, vol. 1, no. 7, pp. 2–5, 2014.

[140] K. Maeda, M. Eguchi, J. W. Youngblood, and T. E. Mallouk, “Calcium niobate nanosheets prepared by the polymerized complex method as catalytic materials for photochemical hydrogen evolution,” *Chem. Mater.*, vol. 21, no. 15, pp. 3611–3617, 2009.

[141] Z. Kap, E. Ülker, S. V. K. Nune, and F. Karadas, “Electrocatalytic hydrogen evolution with cobalt–poly(4-vinylpyridine) metallopolymers,” *J. Appl. Electrochem.*, vol. 48, no. 2, pp. 201–209, 2018.

[142] S. S. Akbari and F. Karadas, “Precious Metal-Free Photocatalytic Water Oxidation by a Layered Double Hydroxide-Prussian Blue Analogue Hybrid Assembly,” *ChemSusChem*, vol. 14, no. 2, pp. 679–685, 2021.

[143] G. Gundogdu, T. G. Ulusoy Ghobadi, S. Sadigh Akbari, E. Ozbay, and F. Karadas, “Photocatalytic water oxidation with a Prussian blue modified brown TiO_2,” *Chem. Commun.*, vol. 57, no. 4, pp. 508–511, 2021.

[144] A. Juris, V. Balzani, F. Barigelletti, S. Campagna, P. Belser, and A. Von Zelewsky, “Ru(II) polypyridine complexes: photophysics, photochemistry, eletrochemistry, and chemiluminescence,” *Coord. Chem. Rev.*, vol. 84, pp. 85–277, 1998.

[145] N. Sutin and C. Creutz, “Electron-transfer reactions of excited states,” *J. Chem. Educ.*, vol. 60, no. 10, pp. 809–814, 1983.

[146] V. Balzani, G. Bergamini, and P. Ceroni, “Light: A Very Peculiar Reactant and Product,” *Angew. Chem. Int. Ed.*, vol. 54, no. 39, pp. 11320–11337, 2015.

[147] D. R. Turner, A. S. R. Chesman, K. S. Murray, G. B. Deacon, and S. R. Batten, “The chemistry and complexes of small cyano anions,” *Chem. Commun.*, vol. 47, no. 37, pp. 10189–10210, 2011.

[148] S. R. Batten *et al.*, “Syntheses, structures and magnetism of α-$Mn(dca)_2$, $[Mn(dca)_2(H_2O)_2].H_2O$, $[Mn(dca)_2(C_2H_5OH)_2].(CH_3)_2CO$, $[Fe(dca)_2(CH_3OH)_2]$ and $[Mn(dca)_2(L)_2]$, where L = pyridine, CH_3OH or DMF and dca = dicyanamide, $N(CN)_2^-$,” *Dalt. Trans.*, no. 17, pp. 2987–2997, 1999.

[149] J. L. Manson *et al.*, "Structure and Magnetic Ordering of $M^{II}[N(CN)_2]_2$ (M = Co, Ni)," *Chem. Mater.*, vol. 10, no. 9, pp. 2552–2560, 1998.

[150] S. R. Batten and K. S. Murray, "Structure and magnetism of coordination polymers containing dicyanamide and tricyanomethanide," *Coord. Chem. Rev.*, vol. 246, no. 1–2, pp. 103–130, 2003.

[151] S. R. Batten, P. Jensen, B. Moubaraki, K. S. Murray, and R. Robson, "Structure and molecular magnetism of the rutile-related compounds $M(dca)_2$, where M = CoII, NiII, CuII, dca = dicyanamide, $N(CN)_2^-$," *Chem. Commun.*, vol. 3, pp. 439–440, 1998.

[152] M. Kurmoo and C. J. Kepert, "Hard magnets based on transition metal complexes with the dicyanamide anion, $\{N(CN)_2\}^-$," *New J. Chem.*, vol. 22, no. 12, pp. 1515–1524, 1998.

[153] T. Peng, D. Ke, P. Cai, K. Dai, L. Ma, and L. Zan, "Influence of different ruthenium(II) bipyridyl complex on the photocatalytic H_2 evolution over TiO_2 nanoparticles with mesostructures," *J. Power Sources*, vol. 180, no. 1, pp. 498–505, 2008.

[154] H. Lv *et al.*, "Visible-light-driven hydrogen evolution from water using a noble-metal-free polyoxometalate catalyst," *J. Catal.*, vol. 307, pp. 48–54, 2013.

[155] B. D. Yuhas, A. L. Smeigh, A. P. Douvalis, M. R. Wasielewski, and M. G. Kanatzidis, "Photocatalytic hydrogen evolution from FeMoS-based biomimetic chalcogels," *J. Am. Chem. Soc.*, vol. 134, no. 25, pp. 10353–10356, 2012.

[156] H. Lin *et al.*, "Towards a comprehensive insight into efficient hydrogen production by self-assembled $Ru(bpy)_3^{2+}$-polymer-Pt artificial photosystems," *Phys. Chem.*

Chem. Phys., vol. 17, no. 16, pp. 10726–10736, 2015.

[157] Y. Tsuji, K. Yamamoto, K. Yamauchi, and K. Sakai, "Near-Infrared Light-Driven Hydrogen Evolution from Water Using a Polypyridyl Triruthenium Photosensitizer," *Angew. Chem. Int. Ed.*, vol. 57, no. 1, pp. 208–212, 2018.

[158] F. Kishimoto, D. Mochizuki, M. M. Maitani, E. Suzuki, and Y. Wada, "Construction of Highly Hierarchical Layered Structure Consisting of Titanate Nanosheets, Tungstate Nanosheets, $Ru(bpy)_3^{2+}$, and Pt(terpy) for Vectorial Photoinduced Z-Scheme Electron Transfer," *ACS Appl. Mater. Interfaces*, vol. 10, no. 43, pp. 37150–37162, 2018.

[159] K. Nakanishi, G. J. T. Cooper, L. J. Points, L. G. Bloor, M. Ohba, and L. Cronin, "Development of a Minimal Photosystem for Hydrogen Production in Inorganic Chemical Cells," *Angew. Chem. Int. Ed.*, vol. 57, no. 40, pp. 13066–13070, 2018.

[160] S. C. Marguet, M. J. Stevenson, and H. S. Shafaat, "Intramolecular Electron Transfer Governs Photoinduced Hydrogen Evolution by Nickel-Substituted Rubredoxin: Resolving Elementary Steps in Solar Fuel Generation," *J. Phys. Chem. B*, vol. 123, no. 46, pp. 9792–9800, 2019.

[161] P. Wang *et al.*, "Enhanced Hydrogen Evolution in Neutral Water Catalyzed by a Cobalt Complex with a Softer Polypyridyl Ligand," *Angew. Chem. Int. Ed.*, vol. 59, no. 31, pp. 12694–12697, 2020.

[162] K. Kawano, K. Yamauchi, and K. Sakai, "A cobalt–NHC complex as an improved catalyst for photochemical hydrogen evolution from water," *Chem. Commun.*, vol. 50, no. 69, pp. 9872–9875, 2014.

[163] S. Aoi, K. Mase, K. Ohkubo, and S. Fukuzumi, "Mechanism of a one-photon two-

electron process in photocatalytic hydrogen evolution from ascorbic acid with a cobalt chlorin complex," *Chem. Commun.*, vol. 51, no. 82, pp. 15145–15148, 2015.

[164] M. Natali, "Elucidating the Key Role of pH on Light-Driven Hydrogen Evolution by a Molecular Cobalt Catalyst," *ACS Catal.*, vol. 7, no. 2, pp. 1330–1339, 2017.

[165] M. S. Deshmukh, V. S. Mane, A. S. Kumbhar, and R. Boomishankar, "Light-driven Hydrogen Evolution from Water by a Tripodal Silane Based $Co^{II}_6L_{18}$ Octahedral Cage," *Inorg. Chem.*, vol. 56, no. 21, pp. 13286–13292, 2017.

[166] S. Guo, K. K. Chen, R. Dong, Z. M. Zhang, J. Zhao, and T. B. Lu, "Robust and Long-Lived Excited State Ru(II) Polyimine Photosensitizers Boost Hydrogen Production," *ACS Catal.*, vol. 8, no. 9, pp. 8659–8670, 2018.

[167] E. Joliat-Wick *et al.*, "Light-Induced H_2 Evolution with a Macrocyclic Cobalt Diketo-Pyrphyrin as a Proton-Reducing Catalyst," *Inorg. Chem.*, vol. 57, no. 3, pp. 1651–1655, 2018.

[168] W. M. Liao *et al.*, "Semiconductive Amine-Functionalized Co(II)-MOF for Visible-Light-Driven Hydrogen Evolution and CO_2 Reduction," *Inorg. Chem.*, vol. 57, no. 18, pp. 11436–11442, 2018.

[169] S. Chakraborty, E. H. Edwards, B. Kandemir, and K. L. Bren, "Photochemical Hydrogen Evolution from Neutral Water with a Cobalt Metallopeptide Catalyst," *Inorg. Chem.*, vol. 58, no. 24, pp. 16402–16410, 2019.

[170] H. G. Hecht, "Interpretation of Diffuse Reflectance Spectra.," *J. Res. the National Bur. Standards-A. Phys. Chem.*, vol. 80, no. 4, pp. 567–583, 1976.

[171] P. Makuła, M. Pacia, and W. Macyk, "How To Correctly Determine the Band Gap Energy of Modified Semiconductor Photocatalysts Based on UV-Vis Spectra," *J.*

Phys. Chem. Lett., vol. 9, no. 23, pp. 6814–6817, 2018.

[172] A. A. Kokhanovsky, "Physical interpretation and accuracy of the Kubelka-Munk theory," *J. Phys. D. Appl. Phys.*, vol. 40, no. 7, pp. 2210–2216, 2007.

[173] P. Xu, T. J. Milstein, and T. E. Mallouk, "Flat-Band Potentials of Molecularly Thin Metal Oxide Nanosheets," *ACS Appl. Mater. Interfaces*, vol. 8, no. 18, pp. 11539–11547, 2016.

[174] E. A. Turhan, S. V. K. Nune, E. Ülker, U. Şahin, Y. Dede, and F. Karadas, "Water Oxidation Electrocatalysis with a Cobalt-Borate-Based Hybrid System under Neutral Conditions," *Chem. Eur. J.*, vol. 24, no. 41, pp. 10372–10382, 2018.

[175] M. Pramanik, C. Li, M. Imura, V. Malgras, Y. M. Kang, and Y. Yamauchi, "Ordered Mesoporous Cobalt Phosphate with Crystallized Walls toward Highly Active Water Oxidation Electrocatalysts," *Small*, vol. 12, no. 13, pp. 1709–1715, 2016.

[176] O. Sato, T. Iyoda, A. Fujishima, and K. Hashimoto, "Photoinduced magnetization of a cobalt-iron cyanide," *Science*, vol. 272, no. 5262, pp. 704–705, 1996.

[177] S. J. Gerber and E. Erasmus, "Electronic effects of metal hexacyanoferrates: An XPS and FTIR study," *Mater. Chem. Phys.*, vol. 203, pp. 73–81, 2018.

[178] Y. Wang, J. Ma, J. Wang, S. Chen, H. Wang, and J. Zhang, "Interfacial Scaffolding Preparation of Hierarchical PBA-Based Derivative Electrocatalysts for Efficient Water Splitting," *Adv. Energy Mater.*, vol. 9, no. 5, p. 1802939, 2019.

[179] X. Cui, L. Hong, and X. Lin, "Electrochemical preparation, characterization and application of electrodes modified with hybrid hexacyanoferrates of copper and cobalt," *J. Electroanal. Chem.*, vol. 526, no. 1–2, pp. 115–124, 2002.

[180] H. Haraguchi, K. Fujiwara, and F. Keiichiro, "A Study of Cobalt Complexes by X-

ray Photoelectron Spectroscopy," *Chem. Lett.*, vol. 4, no. 5, pp. 409–414, 1975.

[181] D. Atzei, D. De Filippo, A. Rossi, and R. Caminiti, "X-ray photoelectron spectra of dinitrogen chelating ligands with some transition metals," *Spectrochim. Acta Part A Mol. Spectrosc.*, vol. 49, no. 12, pp. 1779–1785, 1993.

[182] K. Lu, B. Song, X. Gao, H. Dai, J. Zhang, and H. Ma, "High-energy cobalt hexacyanoferrate and carbon micro-spheres aqueous sodium-ion capacitors," *J. Power Sources*, vol. 303, pp. 347–353, 2016.

[183] D. Briggs and V. A. Gibson, "Direct observation of multiplet splitting in 2P photoelectron peaks of cobalt complexes," *Chem. Phys. Lett.*, vol. 25, no. 4, pp. 493–496, 1974.

[184] D. Atzei, A. Rossi, and C. Sadun, "Synthesis and characterization of a cobalt(III) complex with 1-(D-3-mercapto-methylpropionyl)-L-proline," *Spectrochim. Acta Part A*, vol. 56, pp. 1875–1886, 2000.

[185] T. Ivanova, A. Naumkin, A. Sidorov, I. Eremenko, and M. Kiskin, "X-ray photoelectron spectra and electron structure of polynuclear cobalt complexes," *J. Electron Spectros. Relat. Phenomena*, vol. 156–158, pp. 200–203, 2007.

[186] M. Berrettoni, M. Ciabocco, M. Fantauzzi, M. Giorgetti, A. Rossi, and E. Caponetti, "Physicochemical characterization of metal hexacyanometallate-TiO_2 composite materials," *RSC Adv.*, vol. 5, no. 45, pp. 35435–35447, 2015.

[187] A. J. Naylor *et al.*, "Depth-dependent oxygen redox activity in lithium-rich layered oxide cathodes," *J. Mater. Chem. A*, vol. 7, no. 44, pp. 25355–25368, 2019.

[188] F. A. Frame *et al.*, "Photocatalytic water oxidation with nonsensitized IrO_2 nanocrystals under visible and UV light," *J. Am. Chem. Soc.*, vol. 133, no. 19, pp.

7264–7267, 2011.

[189] U. S. Akhtar, E. L. Tae, Y. S. Chun, I. C. Hwang, and K. B. Yoon, “Insights into decomposition pathways and fate of $Ru(bpy)_3^{2+}$ during photocatalytic water oxidation with $S_2O_8^{2-}$ as sacrificial electron acceptor,” *ACS Catal.*, vol. 6, no. 12, pp. 8361–8369, 2016.

[190] J. W. Boclair, P. S. Braterman, J. Jiang, S. Lou, and F. Yarberry, “Layered double hydroxide stability. 2. Formation of Cr(III)-containing layered double hydroxides directly from solution,” *Chem. Mater.*, vol. 11, no. 2, pp. 303–307, 1999.

[191] A. J. Bard and M. A. Fox, “Artificial Photosynthesis: Solar Splitting of Water to Hydrogen and Oxygen,” *Acc. Chem. Res.*, vol. 28, no. 3, pp. 141–145, 1995.

[192] J. W. Boclair and P. S. Braterman, “One-Step Formation and Characterization of Zn(II)-Cr(III) Layered Double Hydroxides, $Zn_2Cr(OH)_6X$ (X = Cl, $1/2SO_4$),” *Chem. Mater.*, vol. 10, no. 8, pp. 2050–2052, 1998.

[193] H. Jiang *et al.*, “Photocatalytic reduction of CO_2 on Cu_2O-loaded Zn-Cr layered double hydroxides,” *Appl. Catal. B Environ.*, vol. 224, pp. 783–790, 2018.

[194] O. Sato, V. Einaga, T. Iyoda, A. Fujishima, and K. Hashimoto, “Reversible Photoinduced Magnetization,” *J. Electrochem. Soc.*, vol. 144, no. 1, p. L11, 1997.

[195] Z. Y. Yu *et al.*, “Unconventional CN vacancies suppress iron-leaching in Prussian blue analogue pre-catalyst for boosted oxygen evolution catalysis,” *Nat. Commun.*, vol. 10, no. 1, pp. 1–9, 2019.

[196] M. Lan, G. Fan, L. Yang, and F. Li, “Significantly enhanced visible-light-induced photocatalytic performance of hybrid Zn-Cr layered double hydroxide/graphene nanocomposite and the mechanism study,” *Ind. Eng. Chem. Res.*, vol. 53, no. 33, pp.

12943–12952, 2014.

[197] B. Luo, R. Song, and D. Jing, “ZnCr LDH nanosheets modified graphitic carbon nitride for enhanced photocatalytic hydrogen production,” *Int. J. Hydrogen Energy*, vol. 42, no. 37, pp. 23427–23436, 2017.

[198] Y. Xu, L. Tan, Y. Zhao, and Y. Song, “Visible-Light-Induced Hydrogenation of C=C Bonds by Hydrazine over Ultrathin Layered Double Hydroxide Nanosheets,” *Ind. Eng. Chem. Res.*, vol. 59, no. 32, pp. 14315–14322, 2020.

[199] C. G. Silva, Y. Bouizi, V. Fornés, and H. García, “Layered double hydroxides as highly efficient photocatalysts for visible light oxygen generation from water,” *J. Am. Chem. Soc.*, vol. 131, no. 38, pp. 13833–13839, 2009.

[200] S. S. Akbari, U. Unal, and F. Karadas, “Photocatalytic Water Oxidation with a CoFe Prussian Blue Analogue–Layered Niobate Hybrid Material,” *ACS Appl. Energy Mater.*, vol. 4, no. 11, pp. 12383–12390, 2021.

[201] H. Hata, Y. Kobayashi, V. Bojan, W. J. Youngblood, and T. E. Mallouk, “Direct deposition of trivalent rhodium hydroxide nanoparticles onto a semiconducting layered calcium niobate for photocatalytic hydrogen evolution,” *Nano Lett.*, vol. 8, no. 3, pp. 794–799, Mar. 2008.

[202] Q.Q. Wang, B.Z. Lin, B.-H. Xu, X.L. Li, Z.J. Chen, and X.-T. Pian, “Preparation and photocatalytic properties of mesoporous SnO_2–hexaniobate layered nanocomposite,” *Microporous Mesoporous Mater.*, vol. 130, no. 1–3, pp. 344–351, 2010.

[203] X. Kong *et al.*, “Ti-O-O coordination bond caused visible light photocatalytic property of layered titanium oxide,” *Sci. Rep.*, vol. 6, no. 1, p. 29049, 2016.

[204] Y. Matsumoto, “Energy positions of oxide semiconductors and photocatalysis with iron complex oxides,” *J. Solid State Chem.*, vol. 126, no. 2, pp. 227–234, 1996.

[205] K. Akatsuka, G. Takanashi, Y. Ebina, M. A. Haga, and T. Sasaki, “Electronic band structure of exfoliated titanium-and/or niobium-based oxide nanosheets probed by electrochemical and photoelectrochemical measurements,” *J. Phys. Chem. C*, vol. 116, no. 23, pp. 12426–12433, 2012.

[206] J. C. Wojdeł, I. de P. R. Moreira, S. T. Bromley, and F. Illas, “Prediction of half-metallic conductivity in Prussian Blue derivatives,” *J. Mater. Chem.*, vol. 19, no. 14, pp. 2032–2036, 2009.

[207] Y. C. Wang, C. Y. Chang, T. F. Yeh, Y. L. Lee, and H. Teng, “Formation of internal p−n junctions in Ta_3N_5 photoanodes for water splitting,” *J. Mater. Chem. A*, vol. 2, no. 48, pp. 20570–20577, 2014.

[208] S. Wang *et al.*, “Controllable fabrication of homogeneous ZnO p−n junction with enhanced charge separation for efficient photocatalysis,” *Catal. Today*, vol. 335, pp. 151–159, 2019.

[209] H. Lim *et al.*, “Activation of a Nickel-Based Oxygen Evolution Reaction Catalyst on a Hematite Photoanode via Incorporation of Cerium for Photoelectrochemical Water Oxidation,” *ACS Appl. Mater. Interfaces*, vol. 9, no. 36, pp. 30654–30661, 2017.

[210] S. Ida and T. Ishihara, “Recent progress in two-dimensional oxide photocatalysts for water splitting,” *J. Phys. Chem. Lett.*, vol. 5, no. 15, pp. 2533–2542, 2014.

[211] Y. Hu *et al.*, “Layered perovskite oxides and their derivative nanosheets adopting different modification strategies towards better photocatalytic performance of water

splitting," *Renew. Sustain. Energy Rev.*, vol. 119, p. 109527, 2020.

[212] O. C. Compton, E. C. Carroll, J. Y. Kim, D. S. Larsen, and F. E. Osterloh, "Calcium niobate semiconductor nanosheets as catalysts for photochemical hydrogen evolution from water," *J. Phys. Chem. C*, vol. 111, no. 40, pp. 14589–14592, 2007.

[213] F. E. Sarac and U. Unal, "Electrochemical-Hydrothermal Synthesis of Manganese Oxide Films As Electrodes for Electrochemical Capacitors," *Electrochim. Acta*, vol. 178, pp. 199–208, 2015.

[214] M. Hekmatfar, A. Kazzazi, G. G. Eshetu, I. Hasa, and S. Passerini, "Understanding the Electrode/Electrolyte Interface Layer on the Li-Rich Nickel Manganese Cobalt Layered Oxide Cathode by XPS," *ACS Appl. Mater. Interfaces*, vol. 11, no. 46, pp. 43166–43179, 2019.

[215] K. Domen *et al.*, "A novel series of photocatalysts with an ion-exchangeable layered structure of niobate," *Stud. Surf. Sci. Catal.*, vol. 75, pp. 2159–2162, 1993.

[216] Y. Ebina, N. Sakai, and T. Sasaki, "Photocatalyst of lamellar aggregates of RuOx-loaded perovskite nanosheets for overall water splitting," *J. Phys. Chem. B*, vol. 109, no. 36, pp. 17212–17216, 2005.

[217] S. S. Akbari and F. Karadas, "Selective photocatalytic CO_2 reduction by cobalt dicyanamide," *Dalt. Trans.*, vol. 51, no. 33, pp. 12569–12575, 2022.

[218] J. Palion-Gazda *et al.*, "Influence of the pyrazine substituent on the structure and magnetic properties of dicyanamide-bridged cobalt(II) complexes," *Dalt. Trans.*, vol. 48, no. 46, pp. 17266–17280, 2019.

[219] M. Mann, O. Reckeweg, N. Nöthling, R. Goddard, and R. Dronskowski, "Syntheses and characterization of two dicyanamide compounds containing monovalent cations:

$Hg_2[N(CN)_2]_2$ and $Tl[N(CN)_2]$," *Inorganics*, vol. 6, no. 4, p. 135, 2018.

[220] A. Sivanantham, P. Ganesan, L. Estevez, B. P. McGrail, R. K. Motkuri, and S. Shanmugam, "A Stable Graphitic, Nanocarbon-Encapsulated, Cobalt-Rich Core–Shell Electrocatalyst as an Oxygen Electrode in a Water Electrolyzer," *Adv. Energy Mater.*, vol. 8, no. 14, p. 1702838, 2018.

[221] N. Hellgren, R. T. Haasch, S. Schmidt, L. Hultman, and I. Petrov, "Interpretation of X-ray photoelectron spectra of carbon-nitride thin films: New insights from in situ XPS," *Carbon N. Y.*, vol. 108, pp. 242–252, 2016.

[222] J. K. Chang, M. T. Lee, W. T. Tsai, M. J. Deng, and I. W. Sun, "X-ray photoelectron spectroscopy and in situ X-ray absorption spectroscopy studies on reversible insertion/desertion of dicyanamide anions into/from manganese oxide in ionic liquid," *Chem. Mater.*, vol. 21, no. 13, pp. 2688–2695, 2009.

[223] H. Hashimoto, A. Ohno, K. Nakajima, M. Suzuki, H. Tsuji, and K. Kimura, "Surface characterization of imidazolium ionic liquids by high-resolution Rutherford backscattering spectroscopy and X-ray photoelectron spectroscopy," *Surf. Sci.*, vol. 604, no. 3–4, pp. 464–469, 2010.

[224] G. S. Stucky, T. A. Carlson, and G. A. Vernon, "Comprehensive Study of Satellite Structure in the Photoelectron Spectra of Transition Metal Compounds," *Inorg. Chem.*, vol. 15, no. 2, pp. 278–284, 1976.

[225] J. Dong, M. Wang, X. Li, L. Chen, Y. He, and L. Sun, "Simple nickel-based catalyst systems combined with graphitic carbon nitride for stable photocatalytic hydrogen production in water," *ChemSusChem*, vol. 5, no. 11, pp. 2133–2138, 2012.

[226] J. Wang *et al.*, "Polymer-modified hydrophilic graphene: A promotor to

photocatalytic hydrogen evolution for in situ formation of core@shell cobalt nanocomposites," *J. Photochem. Photobiol. A Chem.*, vol. 331, pp. 247–254, 2016.

[227] G. H. Allen, R. P. White, D. P. Rillema, and T. J. Meyer, "Synthetic Control of Excited-State Properties. Tris-Chelate Complexes Containing the Ligands 2,2'-Bipyrazine, 2,2'-Bipyridine, and 2,2'-Bipyrimidine," *J. Am. Chem. Soc.*, vol. 106, pp. 2613–2620, 1984.

[228] B. Durham, J. V Caspar, J. K. Nagle, and T. J. Meyer, "Photochemistry of $Ru(bpy)_3^{2+}$," *J. Am. Chem. Soc.*, vol. 104, pp. 4803–4810, 1982.

[229] T. Morimoto, T. Nakajima, S. Sawa, R. Nakanishi, D. Imori, and O. Ishitani, "CO_2 capture by a rhenium(I) complex with the aid of triethanolamine," *J. Am. Chem. Soc.*, vol. 135, no. 45, pp. 16825–16828, 2013.

[230] H. Koizumi, H. Chiba, A. Sugihara, M. Iwamura, K. Nozaki, and O. Ishitani, "CO_2 capture by Mn(I) and Re(I) complexes with a deprotonated triethanolamine ligand," *Chem. Sci.*, vol. 10, no. 10, pp. 3080–3088, 2019.

[231] R. N. Sampaio, D. C. Grills, D. E. Polyansky, D. J. Szalda, and E. Fujita, "Unexpected Roles of Triethanolamine in the Photochemical Reduction of CO_2 to Formate by Ruthenium Complexes," *J. Am. Chem. Soc.*, vol. 142, no. 5, pp. 2413–2428, 2020.

[232] E. Boutin *et al.*, "Molecular catalysis of CO_2 reduction: recent advances and perspectives in electrochemical and light-driven processes with selected Fe, Ni and Co aza macrocyclic and polypyridine complexes," *Chem. Soc. Rev.*, vol. 49, no. 16, pp. 5772–5809, 2020.

[233] N. H. Damrauer, G. Cerullo, A. Yeh, T. R. Boussie, C. V. Shank, and J. K.

McCusker, “Femtosecond dynamics of excited-state evolution in $[Ru(bpy)_3]^{2+}$,” *Science*, vol. 275, no. 5296, pp. 54–57, 1997.

[234] K. J. Rutt and M. N. Hughes, “Complexes of Triethanolamine with Cobalt(II), Nickel(II) and Copper(II) Salts,” *J. Chem. Soc. A Inorganic, Phys. Theor.*, pp. 2788–2790, 1968.

[235] Y. Kuge and S. Yamada, “The Syntheses and the Structure of Triethanolamine Complexes with Cobalt (II) and Nickel (II),” *Bull. Chem. Soc. Jpn.*, vol. 42, pp. 2552–2555, 1969.

[236] S. R. Hosseinian, V. Tangoulis, M. Menelaou, C. P. Raptopoulou, V. Psycharis, and C. Dendrinou-Samara, “Defective dicubanes of CoII/CoIII complexes with triethanolamine and N-donors,” *Dalt. Trans.*, vol. 42, no. 15, pp. 5355–5366, 2013.

[237] S. R. Batten, R. Robson, S. R. Batten, P. Jensen, B. Moubaraki, and K. S. Murray, “Structure and molecular magnetism of the rutile-related compounds $M(dca)_2$, M = CoII, NiII, CuII, dca = dicyanamide, $N(CN)_2^-$,” *Chem. Commun.*, no. 3, pp. 439–440, 1998.

[238] H. S. Jena, S. Goswami, S. Sanda, S. Parshamoni, S. Biswas, and S. Konar, “A perception of ferro- and antiferromagnetic interactions in a two dimensional Ni(II) heterochiral coordination polymer showing unusual CO_2 uptake behavior,” *Dalt. Trans.*, vol. 43, no. 45, pp. 16996–16999, 2014.

[239] Q. Shi, M. L. Hu, H. P. Xiao, and X. H. Li, “Synthesis and magnetic property of a dual μ-$[N(CN)_2]$ bridged copper(II) supramolecule with dinuclear unit,” *Inorg. Chem. Commun.*, vol. 8, no. 12, pp. 1169–1172, 2005.

[240] X. Li, J. Hou, H. Sui, L. Sun, and L. Xu, “Switchable-hydrophilicity triethylamine:

Formation and synergistic effects of asphaltenes in stabilizing emulsions droplets," *Materials*, vol. 11, no. 12, p. 2431, 2018.

[241] W. E. Hatfield and J. T. Yoke, "Complexes of the Ethylamines with the Halides of Calcium, Cobalt(II), and Zinc," *Inorg. Chem.*, vol. 1, no. 3, pp. 463–470, 1962.

[242] B. B. Beyene and C. H. Hung, "Photocatalytic hydrogen evolution from neutral aqueous solution by a water-soluble cobalt(II) porphyrin," *Sustain. Energy Fuels*, vol. 2, no. 9, pp. 2036–2043, 2018.

[243] Y. Lei *et al.*, "Thiomolybdate $[Mo_3S_{13}]^{2-}$ nanocluster: A molecular mimic of MoS_2 active sites for highly efficient photocatalytic hydrogen evolution," *Chem. Commun.*, vol. 54, no. 6, pp. 603–606, 2018.

[244] S. Li, W. Chen, X. Hu, and F. Feng, "Self-Assembly of Albumin and [FeFe]-Hydrogenase Mimics for Photocatalytic Hydrogen Evolution," *ACS Appl. Bio Mater.*, vol. 3, no. 4, pp. 2482–2488, 2020.